A Shock Tube Study of the Pyrolysis of Real Jet Fuels Jet A and JP10

BY

XU HAN

B.Eng., Southeast University, 2008
M.S., University of Illinois at Chicago, 2012

THESIS

Submitted as partial fulfillment of the requirements
for the degree of Doctor of Philosophy in Mechanical Engineering
in the Graduate College of the
University of Illinois at Chicago, 2018
Chicago, Illinois

Defense Committee:

Kenneth Brezinsky, Chair and Advisor, Mechanical and Industrial Engineering
Farzad Mashayek, Mechanical and Industrial Engineering
Patrick Lynch, Mechanical and Industrial Engineering
W.J. Minkowycz, Mechanical and Industrial Engineering
Robert S. Tranter, Argonne National Laboratory

ACKNOWLEDGEMENTS

First, I would like to thank my academic advisor, Prof. Kenneth Brezinsky, for his support for the three year I worked under him. His offering of help when I needed it most enabled me to continue my pursuit of this degree.

I also would like to thank Prof. Farzad Mashayek, Prof. Patrick Lynch, Prof. W.J. Minkowycz, and Dr. Robert S. Tranter from Argonne National Laboratory to be the committees of my final defense. I would also like to thank Dr. Robert S. Tranter for the helpful suggestions on shock tube experiments. I would also like to thank Prof. Hai Wang from Stanford University and other participants involved in the HyChem project for the discussions. Special thanks to Dr Chiping Li for the financial support, AFOSR Award # FA9550-16-1-0079. I also thank the laboratory members Miroslaw Liszka and Juan Pablo Guzman for the 3 years of happily working together. I appreciate all other current or previous members in the High Pressure Shock Tube Laboratory that helped me with the work.

Finally, I would like to give my special thanks to my parents who supported me in many aspects of life during my time as graduate student.

CONTRIBUTION OF AUTHORS

A significant portion of Section 4.1 is reproduced from an accepted manuscript (Xu Han, Miroslaw Liszka, Rui Xu, Kenneth Brezinsky, Hai Wang, A high pressure shock tube study of pyrolysis of real jet fuels Jet A, *Proc. Combust. Inst.*, 37 (2018)) on which I was the first author and the main investigator. My adviser, Professor Kenneth Brezinsky, provided guidance to the experiments and modelling and contributed to the discussions and writing the article. Miroslaw Liszka, my colleague, contributed to performing the experiments. Professor Hai Wang from Stanford University contributed to the discussions and writing the article. Rui Xu and Professor Hai Wang provided the model.

TABLE OF CONTENTS

LIST OF TABLES

LIST OF FIGURES

FIGURE NUMBER PAGE

SUMMARY

The design of jet engines requires an efficient and accurate way of simulating the combustion chemistry in a CFD framework. There are many obstacles in constructing a practical chemical kinetic model for real jet fuel combustion. Detailed mechanisms for multicomponent fuels like Jet A or even single component fuels like JP10 contain too much detail for CFD calculations. Previous approaches such as using surrogate fuel models have not shown satisfying performances. Recently, a new type of model called the HyChem model is proposed as a greatly simplified approach that arose from previous observations of the decoupling of the oxidation and pyrolysis in real combustion processes. The HyChem model is a hybrid chemical kinetic model in which description of the fuel oxidization follows two stages: the fuel pyrolyzes into a limited number of small intermediates through a few lumped reactions and then oxidation of these intermediates occurs through well-known foundation chemistry. The multicomponent fuel is taken as a single species in the model. The present work to experimentally verify the underlying pyrolysis chemistry assumptions is part of the large collaborative work with five other research groups to construct and further validate the HyChem model of real jet fuels. The HyChem models of Jet A (POSF #10325) and JP10 are compared in this thesis against the experimental results of the present work.

In the present work, shock tube experiments on Jet A and JP10 pyrolysis were conducted over a wide range of temperature, pressure, and fuel mole fractions, and in two different shock tubes. The speciation analysis is primarily done through gas chromatography. For both fuels, the experimental results supported the important assumption that the majority of the products of the fuel pyrolysis is represented by a limited number of small species. The simulations results by the HyChem models are compared with the experimental results and show satisfying level of agreement for Jet

A, and excellent agreement for JP10. Techniques such as Monte Carlo simulation are applied to the analysis of the model. Explanations for certain discrepancies are presented in this work.

A concern about the characterization of temperature in a shock tube arose from the comparisons and discussions of the model and the experiments. A critical issue is the changing pressure and temperature profile after the arrival of the reflected shock wave in a shock tube. To address this issue, an investigation of the chemical kinetic simulations when using changing pressure profiles and using a constant pressure approximation was conducted. JP10 pyrolysis experiments from the high pressure shock tube and the lower pressure shock tube with different pressure profiles were also compared. Overall, the results from both simulation and experiments showed that a constant pressure can be used to approximate the changing pressure profile after the reflected shock wave in a single pulse shock tube. Furthermore, the chemical thermometer approach was justified. In addition to sources of temperature uncertainty, real shock wave effects have been examined.

Overall, the present work presents an investigation and critical discussion of the pyrolysis characteristics of Jet A and JP10, the HyChem model, and the temperature characterization of shock tubes. It was done in a collaborative mode, and directly benefitted from the perspectives of many experts in the combustion community.

A description of future work related to jet fuel combustion chemistry and improvements for temperature characterization of shock tubes are suggested.

1 INTRODUCTION

1.1 BACKGROUND

While the combustion of fossil fuels for transportation has been controversial regarding its renewability and its effect to the environment, it will still be the main energy source for transportation vehicles in the foreseeable future. For high speed aircraft and rockets, there is basically no alternative to combustion energy as a propulsion power source. The combustion dynamics in these engines has attracted even more attention nowadays due to the demands in developing hypersonic jets and a new generation of rockets. A basic understanding of the combustion chemistry of real fuels that are used in real engines is critical to a better design of them. A fundamental challenge in building reliable chemical reaction models for jet fuels is the large number of reactions and species involved in the fuel reaction process because of the complexity of the fuel [1]. For example, Jet A fuel is composed of thousands of hydrocarbon species that cannot be tracked at the level of each of these species. The approach of building a surrogate fuel mechanism [1–10] has been commonly used in the past in order to overcome this difficulty. However, even if there are only a few species in a fuel, the number of reactions associated with the decomposition and oxidation of these species can easily reach a few thousand. Therefore, surrogate fuel models are still not compact enough to enable CFD simulations of real combustor processes even after mechanism reduction. This reason prevents even fuels with small number of components, such as JP10 [11–17] and Gevo-ATJ [18], to be modelled efficiently by traditional detailed and reduced models in CFD simulations.

Fortunately, a common pattern of the oxidation process of hydrocarbon fuels recently found has given light to a potential new approach for the simplification of chemical kinetic models for use

in real CFD applications. Previous studies [2,19–26] showed that during the oxidation of large hydrocarbons fuels, fuel pyrolysis is separated from the oxidation of the resulting pyrolysis products in high-temperature combustion. The decoupling of pyrolysis and oxidation opens up an opportunity for building a simpler hybrid chemistry model for multicomponent real fuels in which the fuel decomposition is described by a small set of reactions, leading to the production of a handful of intermediates, followed by the use of a detailed chemistry model to describe the oxidation of these intermediates [25]. The products of large hydrocarbon pyrolysis are mostly small stable species including CH_4, H_2, C_2H_4, C_3H_6, 1-butene, benzene, and toluene. These species typically have reasonably accurate kinetic models for their further decomposition and oxidation. Based on these observations, a new chemical kinetics model for Jet A combustion, called the HyChem model, has been proposed recently [25,27]. This approach makes the assumption that the major pyrolysis processes of a multicomponent fuel are dominated by H-abstraction followed by C-C β-scission. Since the H-abstraction reactions are rate limiting, the reaction processes can be described by a small number of lumped reactions [28–30] that directly form small intermediate products. For example, a long-chain alkane such as *n*-dodecane produces mainly CH_4, H_2, C_2H_4, C_3H_6, and 1-C_4H_8 through H-abstraction and a series of β-scission reactions, which proceed rapidly once initiated, without being significantly interfered by other reactions [21]. The resulting species undergo further reactions to form C_2H_2, allene, propyne, etc., or are oxidized in the presence of oxygen, all of which can be modeled by a foundational chemistry model rather reliably. Fuels with aromatic rings will also quickly form a significant amount of benzene and toluene [23].

These assumptions of the HyChem model need to be further supported and validated by experiments. An accurate determination of the model's parameters and reaction structures requires data from a variety of experimental sources that test the chemical reactions at different conditions

with a range of measurement techniques, each of which has certain advantages. This necessitates collaboration among a number of research groups with different expertise. The development of the HyChem model was conducted in such a collaboration, with 5 research groups in the nation with expertise in shock tubes, flow reactors, flame reactors, and chemical kinetic modelling. The present work is a part of this collaboration, which is a shock tube speciation study conducted at the High Pressure Shock Tube Laboratory at the University of Illinois at Chicago (UIC) [31–33]. It is primarily aimed at examining the underlying assumptions about pyrolysis the chemistry of jet fuels and providing the potential validation of the HyChem model initially constructed by other research groups in this collaboration. Specifically, our main task is to study the pyrolysis products of two important jet fuels, Jet A and JP10, over a wide range of temperature, pressure and fuel mole fractions in the shock tubes, using product sampling with gas chromatography (GC) analysis. The theory and model construction part was handled by Prof. Hai Wang's group [34] from Stanford University. The model was fitted against the speciation data collected from the shock tube laser diagnostic speciation study done by Prof. Ronald Hanson's group from Stanford University and the flow reactor speciation study done by Prof. Tom Bowman's group [35] from Stanford University. The ignition delay study was also done by Prof. Hanson's group from Stanford University for validation. The flame study was done by Prof. Fokion Egolfopoulos' group [36] from University of South California. More complex CFD studies [37] may be done after this project by other research groups. Experiments on other jet fuels in our UIC laboratory are likely to be conducted in the future. A significant portion of work from all the research groups involved resulted from the discussion of and comparison between the model and experimental data.

1.2 SCOPE OF WORK

As the first part of this study, our experimental work on fuel pyrolysis covers the measurement of all the major hydrocarbon products at temperatures from 800 K to 2200 K and pressures from 1 atm to 90 atm. The fuel mole fractions of the test gases range from below 100 ppm to thousands of ppm. Our experimental work takes advantage of the GC species measurement technique and the ability to reach high pressure/highly dilute reaction conditions in our laboratory [31]. These are a good complement to the experiments from the Stanford groups. While the GC technique, as described later, cannot measure time resolved speciation profiles, it has more sensitivity for speciation than laser diagnostics as applied by Dr. Hanson's shock tube group. Laser diagnostics will have trouble reaching good accuracy at high temperature, and it is hard to detect many species at a time. Our speciation data can measure all the stable hydrocarbon products from a single shock and can thus examine the HyChem assumption that the fuel pyrolysis forms a limited number of species in shock tube conditions. Furthermore, both the Stanford flow reactor and the Stanford shock tube experiments in this study were done at high concentration (> 1000 ppm fuel) and low pressure (1 - 15 atm). The shock tube studies in this work not only included similar conditions to the above, but also added results in the dilute range (< 100 ppm fuel) and up to 90 atm pressure. The collaborative nature of this work brought great value to the combustion chemistry community.

The Jet A fuel of interest to the current study is an average Jet A (POSF#10325) [38,39]. This fuel is designated as A2 fuel in the recent National Jet Fuel Combustion Program [38] and has an average molecular formula of $C_{11.37}H_{21.87}$. The main components are, by mass, 20.0% n-paraffins, 29.5% iso-paraffins, 24.9% cyclo-paraffins, 6.8% dicyclo-paraffins, and 18.7% aromatics. It will be called Jet A in the later part of the text. However, note that it is called A2 in the HyChem main

papers and its official website [40], since they have the models of a few different Jet A fuels.

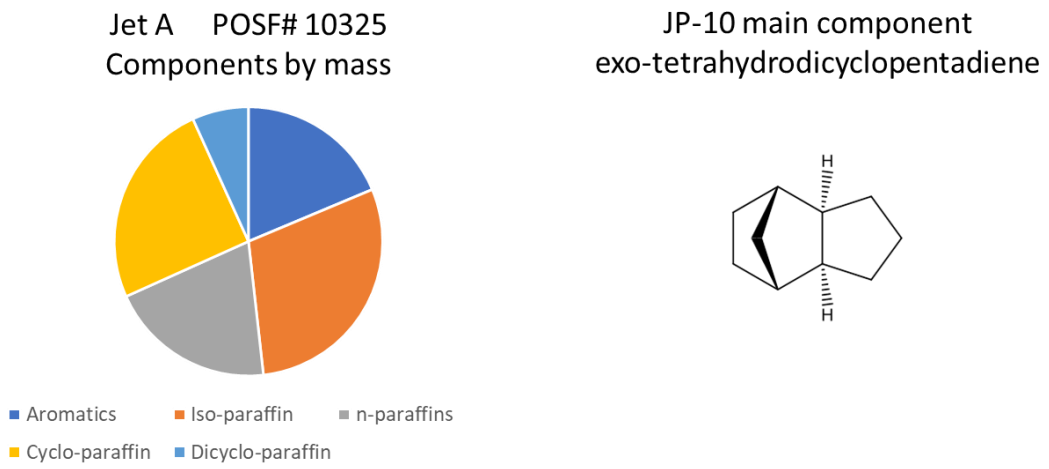

Figure 1: Illustration of the components of the Jet A and JP10 fuel investigated in this study.

The major species of the other jet fuel in this study, JP10 (POSF#7478), is exo-tetrahydrodicyclopentadiene ($C_{10}H_{16}$) which makes up about 96% of the total fuel by mass, while the minor species include endo-tetrahydrodicyclopentadiene ($C_{10}H_{16}$), adamantane ($C_{10}H_{16}$), and decahydronaphthalene ($C_{10}H_{18}$), all of which have ring structures constructed of C-C single bonds.

Two shock tubes with different configurations and pressure ranges were applied in the UIC study. In the UIC shock tube study, all of the major pyrolysis product species were measured and compared to the results predicted by the HyChem model. Overall, the HyChem model can satisfactorily predict well the shock tube reactions. The JP10 model shows an overall excellent match with our experiments, while the Jet A model shows satisfactory predictions of our experimental data, with some evident discrepancies between model and our experiments. The experimental results generally supported the assumption made by the model that the pyrolysis products are limited to a number of small intermediates. Further analyses of the models were

conducted using Monte Carlo simulations with predefined uncertainties in the rate parameters of the fuel pyrolysis chemistry and foundational chemistry. It mainly serves as a sensitivity study. The dominant reactions are identified for different temperature regions. This study showed that different temperature regions have different dominant chemistry. The discrepancies between model and experimental results are discussed with the knowledge of how the model is derived and how the experimental data from all contributing research groups are obtained. There are already some detailed analyses on the uncertainties and discrepancies done by the modelling group of HyChem [25,27]. We seek to add our further insights here in this thesis, using our better knowledge of the data we generated. Besides the HyChem model, another chemical kinetic model – the 2nd Generation Surrogate model for Jet A fuel developed by Malewicki et al. [2] based on previous studies [2,3,21] was used to simulate the reactions in the shock tubes. The predictions from the surrogate model were compared with those from the HyChem model. The comparison showed that there are many differences between the two types of models in predicting the multicomponent Jet A fuel.

An important and fruitful part of the discussions in this collaborative project is on the temperature measurements in experiments. The concern arises from some discrepancies between the UIC shock tube data and Stanford shock tube data. The discrepancies could be considered small in a sense that they don't significantly affect the ignition delay predictions. However, for more precise kinetic modelling in the future, resolving these discrepancies will become increasingly important.

Currently a variety of experimental data sets, along with a set of models built upon them, e.g. [41–44], are available in the chemical kinetic community. There is considerable difference among them regarding their description of combustion chemistry. For example, even for C_2H_4, a simple and

critical species in most combustion reactions of interest, different kinetic models predict a different pyrolysis profile, with the largest discrepancy in the C_2H_4 mole fraction to be about 30% of its initial mole fraction at 1600 K [45]. Anyway, the point here is that, the uncertainties of measurements, especially those for temperature, require a thorough understanding within the whole community of combustion. Although it may not be fully addressed in the short term, some improvements can be made for an accurate knowledge of the physical process in real shock tubes, and the understanding of the uncertainty of temperatures of not just one's own research group will give direction to future improvement and unification of kinetic models.

A significant section of this thesis is devoted to the temperature characterization of the shock tubes and their replications in numerical models of homogeneous reactors. A main focus is to revisit whether or not the constant pressure model can be used to describe our shock tube. This is important, because for shock tubes with the gas chromatography (GC) speciation method, the species measurement can only be done after the reaction is completed. The actual shock pressure history profile is not perfectly flat with time. Even if the shock is made close to perfectly flat, the finite decrease rate of the pressure after the rarefaction wave arrives is unavoidable. Researchers attempted to use chemical thermometers to cover the overall effect of the whole process [46,47]. However, the nonlinear nature of chemical kinetic networks still raises concern for that. There are previous studies on the non-constant pressure issue of shocks. In this work, we seek to provide more understanding of it, based on the speciation data and the pressure profiles in our two different shock tubes, and with some support from the theoretical aspect. The reaction process that is imposed with a changing pressure profile with rising post-shock pressure and finite dwelling rate (dropping rate) is compared to the standard constant pressure model in simulation and also compared to the case with a flat pressure profile with finite dwelling rate in experiments. Chemical

thermometers will be used for this study in experiments and discussed in the temperature characterization section. Concerns about the chemical thermometer approach are addressed. The validity of their use is further examined by the analysis of the changing pressure simulation and constant pressure approximation.

The temperature uncertainty of our shock tube experiments is also revisited, bringing about a newly discovered calculation method. Some other details of shock wave experiments have been looked into in our latest research. In this thesis, we will present a preliminary analysis of the behavior of the reflected shock waves in our lower pressure shock tube, which will show directions in future investigations to reduce temperature uncertainty.

Although the HyChem models for the Jet A and JP10 are already constructed and compared to the data from both shock tube groups, it will be revisited in the future. Consequently, we expect that the discussion we provide here will give one a better understanding of the model and other sources of problems that produce discrepancies among experiments or between a model and an experiment.

At the end of this thesis, some past efforts in studying heterogeneous combustion is briefly described. Some future work related to the jet fuel combustion study and temperature characterization is proposed.

2 EXPERIMENTAL SETUP

2.1 INTRODUCTION TO SHOCK TUBES

A shock tube is a mechanical tube in which a shock wave can be formed and propagate along the tube, often in a one-dimensional form. It has been widely applied to study gas phase chemical kinetics. The shock tubes we use in this work can be described as single-pulse shock tubes with diaphragms. Typically, a shock tube of this type is separated by a diaphragm or a short diaphragm section into a driver section and a driven section. The driver section will be filled with a higher pressure gas than the driven section, and eventually burst the diaphragm and create a shock wave. This shock wave will pressurize and heat the gas it passes through instantaneously. Thus, the gas phase chemistry can be studied at a constant high temperature starting from the onset of the reaction process, without the effect of a smoothly-rising temperature. Shock tubes can also be used to study surface reactions or gas/condensed state interactions of aerosols [48–51]. They can be also used to study surface reactions with a stationary surface installed in the driven section [52] Some shock tubes are focused on aerodynamics research [53–56] and the fracture of solid materials [57,58] The detailed shock wave theory relevant to our shock tube configuration will be given in Section 2.2. The setup and functionality of the two shock tubes, UIC high pressure shock tube and UIC lower pressure shock tube will be given in Section 2.3.

2.2 BASIC SHOCK THEORY IN SHOCK TUBES

The shock wave, rarefaction wave, and contact surface formed in a shock tube can be illustrated as in the following $x - t$ diagram.

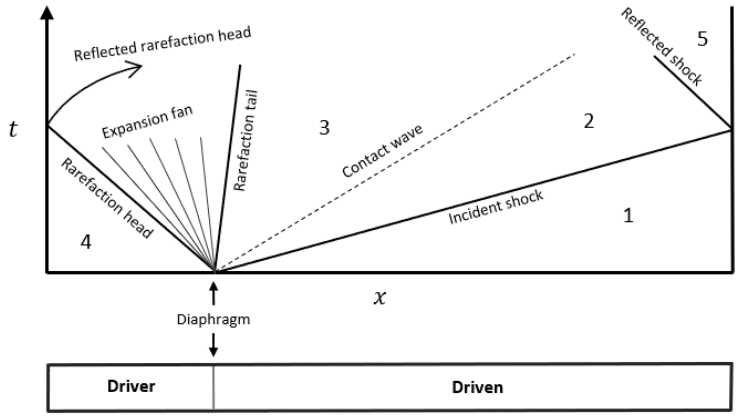

Figure 2: *x* - *t* diagram showing wave propagation in a shock tube, reproduced from [59]**.**

A shock wave is a wave travelling faster than the speed of sound of the local fluid. A simple situation where shock waves are formed is when high pressure gas is suddenly in contact with the low pressure gas. Compression waves will be formed and move towards the low pressure gas. The later compression waves will catch up with the earlier ones because fluid behind the earlier waves is moving in the same direction of the wave, which makes the later ones move faster than the earlier waves, regarding their relative velocities to the stationary gas (or the laboratory). In addition, the temperature of the gas behind the earlier compression waves will rise, leading to increased speed of sound, further increasing the total velocity with the laboratory as the reference. These compression waves will merge and form the shock wave. This process can be initiated by the rupture of a diaphragm separating the high pressure and low pressure gas, as happens in a shock

tube. Although the complete rupture of the diaphragm is a gradual process (not “instantaneous”) and can be disordered in the beginning of the burst and varies every time, a well-developed shock wave can still be formed if the rupture is abrupt enough.

In the direction opposite to one where shock waves are formed, rarefaction waves will be formed at the rupture location and propagate towards the driver gas direction,and will lower the temperature and pressure isentropically. A contact surface, as shown in Figure 2, will also propagate towards the driven section, but more slowly than the shock wave. Both the rarefaction wave and shock wave will reflect once they hit the end walls.

When the incident shock wave reflects after hitting the end wall of the driven section, the reflected shock wave will further heat and pressurize the gas that has been previously compressed by the incident shock wave. On the other hand, rarefaction waves can reflect from the end wall of the driver section, and then meet the reflected shock wave and pass through it, thus rapidly reducing the pressure and temperature in the region that previously experienced the reflected shock wave. A faster cooling by the rarefaction wave is preferred in chemical kinetic experiments because this will create a reaction history that more resembles one with a constant pressure and temperature (if the reactions have negligible pressure and temperature effects), as well as a clear reaction time.

The reflection of the shock wave and rarefaction waves from the two end walls can continue for a few round trips. The installation of a dump tank near the diaphragm in the driven section can reduce the strength of the reflected shock wave significantly each time it passes. Thus, the test gas will not react again after it experiences the first cooling process.

The Mach number M_1 of an incident shock wave in a shock tube can be estimated by the following equation [59,60]:

$$\frac{P_4}{P_1} = \frac{2\gamma_1 M_1^2 - \gamma_1 + 1}{\gamma_1 + 1}\left[1 - \frac{\gamma_4 - 1}{\gamma_1 + 1}\cdot\frac{a_1}{a_4}\left(M_1^2 - \frac{1}{M_1^2}\right)\right]^{-\frac{2\gamma_4}{\gamma_4 - 1}} \qquad (2.1)$$

where P_1, γ_1, a_1 are the initial pressure, temperature, specific heat ratio, and speed of sound of the lower pressure gas in the driven section, respectively, while P_4, γ_1, a_1 are those for the higher pressure gas in the driver section. $M_1 = \frac{W_s}{a_1}$ is the Mach number of the incident shock wave. The speed of sound, a, of any gas can be calculated by

$$a = \sqrt{\frac{\gamma RT}{M_g}} \qquad (2.2)$$

where R is the universal gas constant, T is the gas temperature and M_g is the molar mass of the gas. Typically, Eq (2.1) is not used in experiments. Rather, W_s is measured. However, the equation is still used sometimes to evaluate the performance of shock tubes or to design shock tubes.

With the incident shock wave velocity W_s known, a calorically perfect gas with a constant specific heat ratio γ behind an ideal shock wave satisfies the following equations [59,60],

$$\frac{P_2}{P_1} = \frac{2\gamma M_1^2 - \gamma + 1}{\gamma + 1} \qquad (2.3)$$

$$\frac{T_2}{T_1} = \frac{\left(\gamma M_1^2 - \frac{\gamma-1}{2}\right)\left(\frac{\gamma-1}{2}M_1^2 + 1\right)}{\left(\frac{\gamma+1}{2}\right)^2 M_1^2} \qquad (2.4)$$

where. P_2, T_2 are the pressure and temperature before the shock wave, respectively.

When the normal shock wave hits the end wall, the reflected shock will satisfy [59,60]

$$\frac{P_5}{P_1} = \frac{2\gamma M_1^2 - \gamma + 1}{\gamma + 1}\left[\frac{(3\gamma-1)M_1^2 - 2(\gamma-1)}{(\gamma-1)M_1^2 + 2}\right] \qquad (2.5)$$

$$\frac{T_5}{T_1} = \frac{[2(\gamma-1)M_1^2 + 3 - \gamma][(3\gamma-1)M_1^2 - 2(\gamma-1)]}{(\gamma+1)^2 M_1^2} \qquad (2.6)$$

$$\frac{M_R}{M_R^2 - 1} = \frac{M_1}{M_1^2 - 1}\sqrt{1 + \frac{2(\gamma-1)}{(\gamma+1)^2}(M_1^2 - 1)\left[(\gamma+1)\frac{1}{M_1^2}\right]} \qquad (2.7)$$

where P_5, T_5 are the pressure and temperature behind the reflected shock wave, respectively. M_R is the Mach number of the reflected shock wave. Note that M_R stands for the Mach number that corresponds to the velocity relative to the moving gas in Region 2 that has been heated by the incident shock wave. The velocity of the reflected shock wave W_R stands for the one that is relative to the stationary objects in the laboratory, and can be directly measured through experiments. It can be predicted by [59,60]:

$$\frac{W_R}{W_S} = \frac{2 + \frac{2}{\gamma - 1}\frac{p_1}{p_2}}{\frac{\gamma + 1}{\gamma - 1} - \frac{p_2}{p_1}} \qquad (2.8)$$

Note that all the above equations are derived in the case when γ does not change with temperature and there is no effect from chemical reactions. When the gas experiencing the shock is of polyatomic nature, the rise of c_p and c_v (thus a reduced γ) induced by the rise of temperature due to the shock wave will render a lower estimate of temperature than expected in the case of constant c_p, c_v, γ. This effect becomes significant when the mole fraction of a jet fuel reaches the level of 1000 ppm at above 1000 K. In this case, the post-shock temperature is dependent on a gas property that is also dependent on that temperature itself. A Newton-Raphson iteration method is needed to numerically calculate the post-shock temperature. A MATLAB program named FROSH developed by Campell [61] is applied to solve this problem.

It should also be pointed that the turbulent boundary layer and a strong contact surface behind the shock wave will attenuate the strength of the shock wave. This phenomenon has been examined in many previous studies [62–67]. Typically, the incident shock wave generates a boundary layer first in Region 2 depicted in the $x - t$ diagram in Figure 2. Then the reflected shock enters Region 2 and interacts with the nonuniform flow, causing the pressure of the post-reflected-shock region (Region 5) to gradually increase. The pressure in this region can further increase, if the shock wave meets the contact surface too early and generates a reflected shock to interact with this region before the rarefaction wave arrives.

To make it clear, we call a shock an ideal one when the shock wave can be described by Equations 2.5-2.6, and there is no pressure change at a certain location after experiencing the reflected shock before the rarefaction wave or other waves reach this location when chemical reactions have a negligible on the aerodynamic processes of the gas.

2.3 SHOCK TUBES IN THE UIC HIGH PRESSURE SHOCK TUBE LABORATORY

Two shock tubes are used in this experimental study of JP10 and Jet A. They are the high pressure single pulse shock tube (HPST) and the lower pressure single pulse shock tube (LPST) at UIC. The HPST can stand up to 1000 atm of shock pressure, while the LPST can stand up to 14 atm of shock pressure as tested. Details about these reactors are described previously by Tranter et al. [31,33] for the HPST, and Fridlyand et al. [68] and Keifer et al [69] for the LPST.

Briefly, for the HPST, the driver section is 60 inches long with a 2-inch bore, and the driven section is 118 inches long with 1-inch bore. The HPST has a double diaphragm section. In this study, it is only used with a single diaphragm. A dump tank is located close to the diaphragm on the driven side of the shock tube. The shock pressures of the experiments in the HPST for this study are typically around 25 atm and 90 atm. The HPST is heated to 100 °C to prevent fuel condensation.

For the LPST, the driver section is 48 inches with a 4-inch bore, and the driven section is 174 inches with 2.5-inch bore. Different from configuration in the HPST, the diaphragm section in the LPST consists of two diaphragms that form a 1” long intermediate section. This arrangement enables better control of the burst pressure of the diaphragms and thus the temperature of reaction obtained. The shock pressures in LPST for this study are typically around 1 atm, 4 atm, and 12 atm. The diaphragms are polyester films of which different thickness are chosen for each pressure range. For shocks around 1 atm, two 0.0005” thick diaphragms are used. In the future, the combination of a 0.0005” diaphragm and a 0.001” one is suggested for better performance. For shocks around 4 atm, a 0.002” diaphragm and a 0.003” one are used. For shocks around 12 atm, a 0.005” and a 0.007” diaphragm, or two 0.005” diaphragms are used.

A schematic of the sizes of the two shock tubes is given in Figure 3 for comparison. Note that the bore size and length are in different scales in the figure. In the actual shock tubes, the bore of the driven section is small compared to the length of the tube. Therefore, in the figure, the bores are sketched to look much larger than they are in reality in comparison with the length of the shock tube, in order to have a schematic idea of how the two shock tubes compare with each other in both bore size and length.

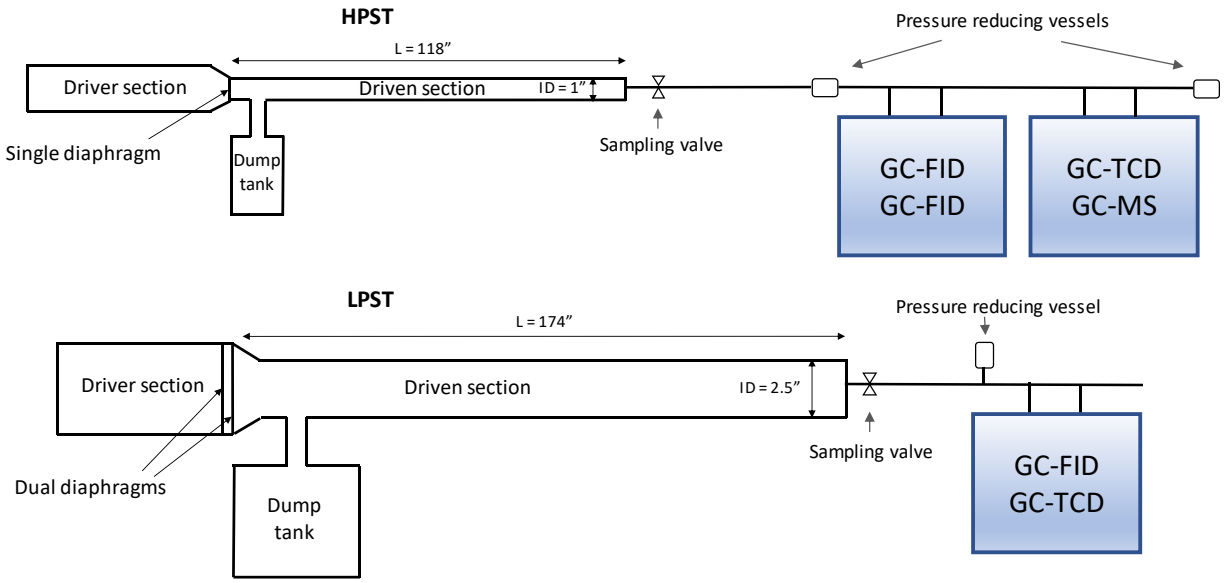

Figure 3: Comparison between the HPST (in single diaphragm configuration) and LPST in size, sampling lines, and connected analytical equipment. The vertical lines of the shock tubes representing the bores are rescaled to look larger for easier visualization.

In a difference from setups in previous studies by Aleksandr Fridlyand et al. [68,70], the LPST is now heated to 100 °C. This caused an effect on the velocity of the incident shock wave making it drop along the axis of the shock tube. Therefore, the end wall velocity needs to be obtained through extrapolation of the side wall measurements of velocity or time instead of averaging.

For the HPST, 6 PCB 113A22 (5,000 psi) or 113A23 (10,000 psi) pressure transducers are embedded in the side wall of the shock tube, close to the end wall, with a known distance between each pair along the axial direction of the shock tube. Another PCB 113B24 (1,000 psi) pressure transducer is attached to the end wall. The velocity at the end wall in this study is determined by the extrapolation of the side wall velocities or an arrival-time-extrapolation method we will later

discuss in the thesis. For the LPST, the side wall and end wall pressure transducers are all PCB 113A21 ones.

The pressure signals from the pressure transducers are connected to two PCI-DAS4020/12 high-speed data acquisition cards. A LabVIEW program written by Dr. Robert Tranter was used to control the data acquisition, the pneumatic valves' opening, and part of the signal processing for the operation of the HPST. Another LabVIEW program written by Aleksandr Fridlyand with minor modifications is used for a similar purpose on the LPST.

2.4 ANALYTICAL INSTRUMENTS

In shock tube experiments for chemical kinetic studies, chemical species formed through the reactions need to be quantified. Typical methods for species diagnostics include gas chromatography (GC), mass spectroscopy (MS), and laser diagnostics. There are also some advanced forms of measurements based on the above three. They include GCxGC and Time-Of-Flight Mass Spectroscopy, etc. In this work, we only use ordinary GC for species quantification and in some cases GC-MS for species identification.

Using the GC method for speciation, a small volume of post-shock gas is sampled from the shock tube and transferred to the GC(s). The UIC high pressure shock is connected to two GCs. The GC closest to the shock tube has the GC columns connected to two flame ionization detectors (FID).

The two GC columns are an Agilent GS-GASPRO (60 m × 0.32 mm) and an Agilent HP-5 (30 m × 0.32 mm × 0.25 μm). GS-GASPRO is used to separate small species starting from CH_4 up to toluene. HP-5 is mainly used to separate larger species such as the four components of JP10. In the second GC, another Agilent GS-GASPRO (60 m × 0.32 mm) is installed and connected to a mass spectrometer in order to identify the species separated by the GASPRO column in the previous GC. Another column in the second GC is connected to a thermal conductivity detector (TCD). However the species measurement$_S$ from TCD are not included in this work, because all speciation data needed in this work can be acquired from FID detectors which are typically more sensitive, reliable and accurate than TCDs. For the lower pressure shock tube, only one GC was connected at the time of experiment. Only one column that is connected to an FID detector is applied in the experiments of this work. The column is Agilent GS-GASPRO (60 m × 0.32 mm), which is the same as the major column used in the GC used in the HPST.

Instead of the typical split or splitless injection method that is commonly applied in many chemistry research labs, in the GCs in this laboratory, gas samples are first collected in a sample column (or sample loop) with a measured pressure, and directly injected onto the chromatography column by a rotor valve. The sample columns and the rotor values in all GCs are heated to 150 °C.

All stainless steel tubing and connections involved in contacting the sample gas before detection by the FIDs are treated with Silconert. This also includes the FID jet, though it is shown later that the coating of this compartment does not have an observable effect on the results.

The first GC connected to the HPST and the GC connected to the LPST are each equipped with a nickel catalyst methanizer to measure CO and CO_2 when needed. In this case, the methanizer was

connected between a GC column and an FID. It was heated up to 380 °C with hydrogen gas flowing through it. The CO and CO_2 were converted to CH_4 with other species intact, before entering the FID. Tubings attached to the methanizers are not treated with Silconert.

2.5 SAMPLING LINE

The HPST sampling line setup is designed to transport the sampled gas from a shock tube to the GC sample columns and obtain a controllable stable pressure within the pressure limit of the GC sample ports and the high precision pressure gauge. The pressure of the sampled gas in the GC columns should be below 20 psi. The schematic for the connections between sampling line and the shock tubes, as well as the GCs is depicted in Figure 3. At the end wall of the HPST, there is a port connected to a pneumatic value which opens after the shock is detected. The duration of opening (sampling) of this valve is controlled to 0.2 seconds. The rest of the sampling line is connected to this valve. Due to the high pressure of the gas sampled from the HPST experiments, the tubing in the main line is set to be very narrow (1/16" ID), in order to restrict the flow to reduce the pressure to a safe and measurable range for the GC and the manometer (0-20 psi) connected to the line. In the middle of the sampling line, a large volume vessel is attached to relieve the high pressure and to reduce the transient flow rate of gas entering the sample columns. When the pressure reading of the sample columns is around 15 psi, the vessel and the section of the sampling line before the vessel will be disconnected by closing a value in the sampling line. Thus, the pressure reading will

be stabilized quickly, and the gas samples in the sampling columns are then injected onto the chromatography columns. For high pressure shocks at 90 atm, an additional pressure-reducing vessel attached at the end of the sampling line is used to control the pressure. The whole sampling line, including vessels and valves, is coated with Silconert and heated to 150 °C, in order to reduce the loss of heavy species on the walls.

The LPST has a similar setup except that there is only one pressure reducing vessel in the sampling line and that for 1 bar shocks, the pressure-reducing vessel is not used because the pressure in the sampling line is already very low without it.

2.6 TYPICAL EXPERIMENTAL PROCEDURES

2.6.1 FIRING OF SHOCKS

While the test gas fuel concentration, fuel composition, pressure, and other details of an experiment have an influence on how the experiments are done, the general procedures of shock tube experiments are similar.

In a typical set of shock tube experiments, a reactant/diluent mixture is prepared in a high pressure cylinder tank (typically heated at 150 °C) connected to a heated mixing rig. If the reactant is readily available as a vapor at room temperature, then the vapor reactant is injected into the high pressure cylinder under vacuum, with the pressure of the vapor in the mixture cylinder measured by two

high precision pressure manometers (both MKS 631B02TAFH). For single component fuels that are in their liquid phase at standard atmospheric conditions, the fuel will be injected into the cylinder under vacuum by the freeze thaw method (repeated cycles of freezing with liquid nitrogen and thawing with heat plate to degas the liquid fuel followed by the injection of the fuel vapor), also with the pressure of the vapor controlled by the pressure manometers. For multicomponent fuels (including JP10 and Jet A), the fuel is injected by a syringe into a vessel shown in Figure 4 through an injection port with a septum as the sealing body. This vessel is connected to the high pressure mixture cylinder, and is under vacuum and at 150 °C. Once the liquid fuel is injected into the vessel, it is immediately vaporized. Low pressure argon gas is used to flush the vaporized fuel from the vessel into the mixture cylinder. After about 30 seconds of flushing, all the reactants are considered to be flushed into the cylinder, the cylinder will be further filled with high pressure argon gas to reach the designated pressure. After overnight mixing, the mixture is ready to be directly injected into the shock tube with consistent reactant mole fractions.

Figure 4: Picture of the vessel used in the mixture preparation for vaporizing and flushing liquid fuel into the high pressure gas cylinder tank. The vessel is the same with that in [71]**.**

In the HPST, the prepared gas mixture will be injected into the driven section. A certain amount of argon will be filled into the driver section. Then the driver section will be further filled with helium until the diaphragm bursts and generate a shock wave. The pneumatic sampling valve connected to the end wall will be open for 200 ms at about 0.4 s of delay after the shock wave is detected by the first transducer experiencing the incident shock wave. A small volume of sample gas thus enters the sampling line. The driver section gas typically has a small fraction of argon mixed in with the helium. The argon content in the driver gas tailors the strength of the shock wave, generating an incident shock with lower velocity than without argon in driver section at the same pressure conditions (P_4 and P_1), as can be derived from Eq (2.1). At the same time, the argon content can increase the reaction time of the shock wave [72] by reducing the speed of the rarefaction wave because of the change in the speed of sound, a_4. A further increase in argon content can also reduce the contact surface strength and reduce its interference with the reaction region. Typically, the argon content in the driver gas is between 10-20 % of the P_4 in this study.

In the LPST, a shock is fired following a similar procedure except that the diaphragms are burst in a different procedure. First, the intermediate section between the two diaphragm is filled with helium and argon. The driver section is later filled with helium and argon to a desired pressure. The bursting of the diaphragms can be controlled by pumping down the gas in the intermediate section until the diaphragm on the driver section side first bursts followed with the bursting of the other one. Thus, the pressure of both the driver and the driven section before bursting can be well controlled in the LPST. The pneumatic sampling valve connected to the end wall will open for 300 ms without observable delay after the first pressure transducer detects the shock wave

The species will be injected into the GCs after the pressure in the sampling line is stabilized and recorded. The GCs will immediately start the separation process and generate the chromatograph. The sampling line will be flushed for a few times to remove the residuals from the sample.

In both shock tubes, after each experiment with a reactive mixture in the driven section, at least one cleaning shock will be fired to remove any residuals from that experiment. The cleaning shock is typically a high temperature shock (>2000 K) done with argon or oxygen as driven gas and pure helium as driver gas. In this work, we observed that shock experiments of any of JP10, Jet A, and cyclopropylcyanide (CPCN) in the HPST will require more than one cleaning shock to prevent clogging in the sampling line, even though the mixtures were dilute. In the LPST, clogging is never observed (probably due to the low pressure, low sooting, and low volume of flow into the sampling line), but when a high mole fraction of fuel is in the reactant mixture, then a cleaning shock with oxygen instead of argon in the driven section will help reduce the effect from the current experiment's residuals on the next experiment's accuracy.

The actual mole fraction of fuel in the shock tube driven section in each pyrolysis experiment may be different from the value calculated based on the amount of fuel injected into the tank and the final pressure of the tank in the mixture preparation process. The reasons for this may include: inaccuracy of the tank volume, temperature uncertainties of the tank, loss of fuel from the mixture injection line to the driven section. To have better knowledge of the mole fraction of the fuel in the mixture that is actually in the shock tube driven section in the pyrolysis experiments, CO_2 conversion experiments are also conducted. To run such experiments, when the fuel mole fraction is very small (<500 ppm), the mixture will be prepared with fuel, argon, and oxygen, with the same amount of fuel injected into the mixture tank and same final pressure in the tank as in the case for

normal pyrolysis experiments, so that the new oxygen-containing mixture will have the same fuel mole fraction as that in the previous oxygen-free mixture used in pyrolysis experiments. An extremely high temperature shock, with T_5 above 2000 K, is fired with this mixture. The product is sampled and analyzed in the GC with the methanizer connected. If CO_2 and a small amount of CO are the only products observed, then the mole fraction of fuel in the mixture before the shock can be inferred from the mole fractions of CO_2 and CO. These shock experiments are done a few times with different injection pressure in the driven section, in order to check repeatability. Our experience shows that for dilute mixtures of JP10 and Jet A, CO_2 conversion experiments give very repeatable values of the initial fuel mole fraction, independent of the injection pressure.

For CO_2 conversion experiments with a high mole fraction of fuel, the oxygen will not be mixed with the fuel in the mixture tank, in case any oxidation or even explosion of the mixture happens in the tank. In this type of experiment, as was done in the LPST with Jet A, the fuel/Ar mixture is mixed with oxygen in the driven section of the shock tube. The fuel/Ar mixture is injected first into the driven section, and the pressure is recorded. Then a certain amount of oxygen is injected to obtain an equivalence ratio below 0.5. Then a shock is fired after more than 2 hours of mixing. The volumetric fraction of oxygen after being fully mixed is generally controlled below 1/6 of the total volume of the driven gas. This is to ensure a high level of mixing between oxygen and the fuel. The less oxygen added, the less uncertainty of the level of mixing between fuel and oxygen. For example, if we let 4% CH_4 in Ar at 10 psi mix with an additional 1 psi of O_2 and let them fully mix, then in order for the fuel in the newly formed mixture of 3.64% CH_4/ 9.1% O_2 in Ar to be fully consumed into CO_2, then 7.28 % O_2 (0.8 psi of O_2) out of the 9.1% O_2 is needed, with only the 1.82% O_2 remaining (0.2 psi of O_2). If we observed from the GC that the products only contain CO_2, then we know that, at most the 1.82% O_2 is not fully mixed into the fuel/Ar mixture at the

end wall. When we back out the CH_4 mole fraction in the original fuel/Ar mixture (the one without O_2) from the CO_2 fraction, we need to know the change of the mole fraction of CH_4 after mixing. In this example, even without a perfect mixing, we know the reduction of mole fraction of CH_4 after mixing will be between 1 psi/(10 psi+1 psi) to 1 psi/(10 psi+0.8 psi) of the original fraction, which is a very narrow range.

Note that for high fuel mole fractions, in converting the CO_2 mole fraction to the initial fuel mole fraction in the fuel/argon/O_2 mixture, it is not strictly accurate to directly divide the CO_2 mole fraction by the number of carbon atoms of the fuel molecule (11.37 for Jet A). This is due to the fact that for a given mass of such reactant mixtures, the total moles of the mixture will change after the reaction. Although the effect from this change is small in this study, we still applied the rigorous calculation method, which has a more complex expression, as given in Appendix H.

2.6.2 AERODYNAMIC AND TEMPERATURE MEASUREMENT

The detection and measurement of the shock wave generated in each experiment is described in detail in the theses of previous researchers[31,68]. The end wall pressure trace of the shock that is regarded as the one experienced by the reactant sampled into the GC. The time of shock arrival at each side wall pressure transducer is measured. Typically, time intervals between each two neighboring pressure transducers are used to get 5 velocities along the side wall since the distances between transducers are known. The incident velocity at the end wall is extrapolated from these 5 velocities. However, there is an alternative method which uses the extrapolation of 6 arrival times.

There are also other details about the shock wave that are investigated in order to precisely characterize the shock wave, as well as to determine the actual temperature history experienced by the test gas, which will be discussed in Chapter 6.

When the velocity is determined, given the compositions and the temperature of the test gas, the temperature of the gas behind the reflected shock before any reaction taking place ("shock temperature") can be derived from either the ideal shock relations or through the chemical thermometer method (to be discussed later). For dilute mixtures (<500 ppm of fuel), we take the whole test gas as pure argon and do the ideal shock calculation using the molar density and specific heat capacity of pure argon. Since the thermodynamic properties of argon do not change with the increase of temperature before a significant fraction of argon is ionized (which will not occur in our temperatures < 2500 K), we will use Equation (2.6). For concentrated mixtures (>500 ppm of fuel), the fuel content has a non-negligible contribution to the specific heat capacity of the test mixture. Since the post-shock specific heat capacity and the shock temperature are functions of each other, the shock temperature is calculated by iteration methods. As mention earlier, for concentrated mixtures, we use a MATLAB code FROSH [61], to determine this temperature. The required inputs are the species composition, their fractions, their thermodynamic data in NASA polynomial coefficients form, the shock velocity, the initial temperature, and the initial pressure. The initial pressure does not have any effect on temperature prediction, however the code requires it, in order to predict the post-shock pressure.

The pressure trace of each transducer is collected for each shock. The pressure and the reaction time of the shock is determined by the 80% rule [73]. Under this rule, the reaction time of a shock is determined by the time between the arrival of shock wave at the end wall and when the post-

shock pressure is decreased to 80% of its peak. The 80% rule is adopted in the shock tube community as an empirical resolution to the changing post-shock pressure and its finite dwelling rate when the test gas experiences a rarefaction wave. It will be further illustrated how valid the 80% rule is. The nominal pressure is decided by the peak pressure the post-shock gas experienced (see Figure 5). The shock is reported as one with the measured reaction time with a constant pressure of the measured value mentioned above. A typical shock pressure trace with the nominal reaction time of 2.1 msec and nominal pressure of 18.5 psi is shown below in Figure 5.

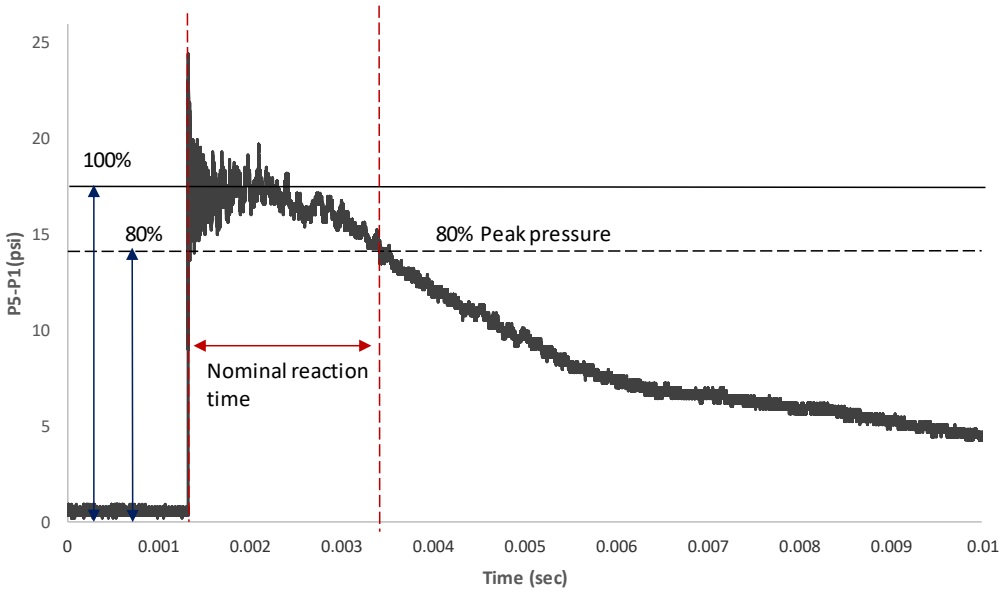

Figure 5: Illustration of the 80% rule on how it determines the nominal reaction time. The pressure trace is obtained from the end wall transducer in the LPST. The pre-shock pressure of this shock is 0.98 psi. The nominal reaction time is 2.1 msec. The nominal pressure is 18.5 psi.

The expression for calibrated temperature T_5 using the 80% rule when using the unimolecular decomposition reaction of a chemical thermometer [73] is,

$$T_{5,cal} = \frac{-\left(\frac{E}{R}\right)}{\ln\left[-\frac{\ln(1-x)}{A\tau}\right]} \qquad (2.9)$$

where E and A are the activation energy and A factor, respectively, for the Arrhenius equation (when the n factor is 0) of that reaction. R is the universal gas constant; x is the extent of reaction, meaning the fraction of the chemical thermometer reacted in the shock; τ is the nominal reaction time measured by the 80% rule as what the red arrows illustrated in Figure 5. If the modified Arrhenius equation is used, i.e. n is not zero in equation, $T_{5,cal}$ is calculated numerically, using Equation (2.10) as following.

$$T_{5,cal} = \frac{-\left(\frac{E}{R}\right)}{\ln\left[-\frac{\ln(1-x)}{AT_{5,cal}^{n}\tau}\right]} \qquad (2.10)$$

The chemical thermometers we used are 1,1,1-trifluoroethane (TFE) with Matsugi's rate parameters[74,75], and cyclopropylcyanide (CPCN) with Lifshitz's rate parameter's[76,77].

Although there has been much debate on whether the 80% rule as well as the chemical thermometer method are good enough to characterize the "averaged" reaction time of a single-shock experiment, at this point in this field they are widely accepted for shock tube studies that rely on GC measurements, because this method works well for the modelling of chemical kinetics. For the experiment data reported in Chapter 4 and Chapter 5, in order to overcome the relatively high rise in pressure, we chose the chemical thermometer method to determine T_5 in HPST; while in LPST, which has very low rise in pressure, we chose the ideal shock relation Eq (2.6) to obtain T_5, in

order to address the cases with high fuel contentin the test gas, since the temperature calibration can only be done for dilute cases and it requires the velocity to get the $T_5(0)$ using the FROSH code for the high-fuel-content case. In Chapter 6, there will be a detailed discussion about the characterization of the reaction temperature and reaction time.

2.6.3 SPECIES MEASUREMENT

The species are identified through the use of both calibration gases and mass spectroscopy. A calibration gas mixture in argon with most of the important C1-C4 product species, with the addition of cyclopentene, benzene, and toluene, was purchased from Air Liquide (later it became part of Airgas). The ppm level in the gas ranges from 50 ppm to 300 ppm. The uncertainty level of species mole fraction is ±5%. Species that were previously known to show up in close retention times are set to have very different ppm values, that makes it easy to distinguish based on the contrast of FID peak areas. Note that here, we took advantage of the fact that the FID response to each ppm of carbon does not vary much among hydrocarbons. The GC method (temperature program, flow rate settings, etc.) of the main GC (for HPST, it's the one closest to the shock tube) is adjusted so that the GasPro column can separate well the major product species up to toluene, especially the C4 ones, and that the HP-5 column can separate the 4 components of JP10. This has also been tested by samples for shock experiments of Jet A and JP10, so that other minor species will not effectively coelute with the major products. Once the temperature program is set, we use the same temperature program in the GC-MS with the same column and same GC method to identify the species again, in order to ensure the previous identification is right. Once the species

are completely identified, we use the GC response obtained from the multiple times of running the GC with the calibration gas mixture injected from the sampling line to generate a response factor for each species. Different mixtures of calibrations gases from other sources (SCOTTY, DCG Partnership I) that has species mole fractions of 10, 15, or 100 ppm are also tested for calibration of the gaseous hydrocarbon species. The CO/CO_2 calibration gas used is from SCOTTY with 0.5% mole fraction. In the HPST, the mixture filled the sampling line with the same pressure (called the injection pressure), typically obtained from the shock tube experiments (~ 16 psi). In the LPST, the injection pressure is not as well controlled in shock experiments because the filling of the sampling line by sampled gas happens very fast and it's hard to adjust the pressure precisely by a valve. Therefore, the calibration is done under a set of injection pressures covering a wide range.

For non-gaseous species, we typically inject the sample in the liquid phase into the 300 ml silconert-treated stainless steel vessel connected to the sampling line under vacuum. The vessel is heated to 150 °C. A syringe containing the liquid is inserted into the silicone septum on the vessel. The 10-μl-range syringe used in the injection has a dead volume even after the needle was shortened. Therefore, the dead volume response was also tested with the 0 μl reading on the syringe by inserting the needle into the steel vessel and observing any GC response. Then, the vessel is pressurized to a given pressure with helium. The mixture mole fraction can be calculated from this pressure. After the liquid is fully mixed in the vessel, with the sampling line under vacuum, we inject the mixture into the sampling line, and then inject into the GC. The GC response per ppm of this species can then be obtained. JP10 is a liquid and can easily be done in this way. The 3 minor species which take only ~ 4% of mass fraction were summed together with the main species, exo-tetrahydrodicyclopentadiene, in measuring the peak area, since they have similar ring structures and will likely give similar FID responses per mole. For cyclopentadiene (CP), the

injected sample is solid in the form of dicyclopentadiene (DCP, melting point at 32.5 °C, boiling point at 170 °C) at room temperature. It is heated to liquid at about 50 °C and injected right away. The vessel is heated to 180 °C which is above its boiling point. It takes tens of minutes to vaporize DCP and break it down into CP (we were still unable to fully convert all the DCP to CP). The DCP and CP GC response for each ppm of carbon should be very close. The ratio of DCP and CP in the column is unknown. We take the sum of peak areas, and take it as all CP in calibrations. Note that we still prefer decomposing as much DCP to CP as possible to reduce error from condensation of DCP in the sampling lines.

It should be pointed out that the retention time of 1,3-butadiene will slightly change in the GS-GasPro column when the diluent gas (Ar, He, or N_2) changes, or when the column has experienced Jet A fuel going through it. Calibration and species identification were reconfirmed in these situations.

For the liquid chemical sources, the JP10 fuel (POSF#7478) is manufactured by Dixie Chemical Company, Inc. The Jet A fuel (POSF#10325) is manufactured by Shell Corporation. Both fuels have been provided by the Air Force Research Laboratory, courtesy Dr. Tim Edwards. Dicyclopentadiene is 95% pure and purchased from Sigma Aldrich.

3 MODELLING AND ANALYTICS

3.1 GAS PHASE CHEMICAL KINETICS

A chemical kinetic model consists of a set of reactions that describe the chemistry that will occur for the initial reactants, the intermediate products, and the final products. The reactions and species form a network that describes the reaction process at a thermodynamic condition, given the thermodynamic properties of each involved species. Each elementary reaction in a detailed chemical kinetic model usually follows one of the forms below, without taking into account the third body effect:

$$A \rightarrow C + D \tag{3.1}$$

$$A \rightarrow C \tag{3.2}$$

$$A + B \rightarrow C + D \tag{3.3}$$

$$A + B \rightarrow C \tag{3.4}$$

For an artificially-configured lumped reaction, the number of reactants or products can be more than two. A general form of a reaction can be expressed as

$$\sum_{i=1}^{I} u_i X_i \xrightarrow{k} \sum_{j=1}^{J} v_j Y_j \tag{3.5}$$

where X_j represent a reactant with u_i being its stoichiometric coefficient, Y_j is a product with v_j being its stoichiometric coefficient, *I* and *J* are the total number of reactants and products in the reaction, respectively. Note that, one species can be a reactant and product at the same time in a single reaction. The rate constant of the reaction, *k*, can be expressed in the modified Arrhenius equation,

$$k = AT^n \exp\left(-\frac{E_a}{RT}\right) \qquad (3.6)$$

where *A* is the pre-exponential factor, *T* is the absolute temperature, *n* is the temperature exponent, E_a is the activation energy, *R* is the universal gas constant. The rate of change of any product for the forward reaction is given by

$$-\frac{1}{u_i}\frac{d[X_i]}{dt} = \frac{1}{v_j}\frac{d[Y_j]}{dt} = k(T)\prod_{l=1}^{I}[X_l]^{u_l} \qquad (3.7)$$

where $i, j = 1, 2, 3 \ldots, I$.

The reverse reaction rate constant k_{rev} of a reaction can be calculated from the forward reaction rate constant and the thermodynamic properties and the reactants and products, through this equation:

$$\frac{k_f}{k_{rev}} = K_{eq} = (RT)^{\Delta v} \exp\left(\frac{\Delta S}{R} - \frac{\Delta H}{RT}\right) \qquad (3.8)$$

where ΔS is the change in molar entropy from the reactants to the products of the forward reaction, ΔH is the molar enthalpy change, Δv is the molar change. An important conclusion derived from this equation is that the reverse reaction rate increases with the increase of the forward reaction rate of a reaction at a given physical reaction condition. More specifically, in building a chemical kinetic model, with a specific reaction and the thermodynamic data of involved species given, the reverse reaction rate will also increase when reaction constants of the forward reaction are arbitrarily modified to increase the forward reaction rate at a given physical condition.

The thermodynamic properties can be modelled using the NASA polynomial coefficients. The equations are given below:

$$\frac{c_p}{R} = a_1 + a_2 T + a_3 T^2 + a_4 T^3 + a_5 T^4 \qquad (3.9)$$

$$\frac{H}{RT} = a_1 + \frac{a_2}{2} T + \frac{a_3}{3} T^2 + \frac{a_4}{4} T^3 + \frac{a_5}{5} T^4 + \frac{a_6}{T} \qquad (3.10)$$

$$\frac{S}{R} = a_1 lnT + a_2 T + \frac{a_3}{2} T^2 + \frac{a_4}{3} T^3 + \frac{a_5}{4} T^4 + a_7 \qquad (3.11)$$

where a_1, a_2, a_3, a_4, a_5, a_6, a_7 are the numerical coefficients supplied in NASA thermodynamic files. Note that even these coefficients are also dependent on temperature. The NASA thermodynamic file typically provides two sets of coefficients for lower and higher temperature ranges, respectively. The data for multicomponent real fuels, including Jet A, is also available for an average molecular formula. The Jet A (POSF#10325) in this study is named POSF10325 in the thermodynamic data, while JP10 is named C10H16.

The transport properties are also needed for combustion simulations with spatial non-homogeneity. It will not be described further in this thesis, since the simulations done in this work are exclusively 0-D closed homogeneous reactors.

3.2 HYCHEM MODEL

As discussed in the introduction, the HyChem Model developed by Dr. Hai Wang's group gives a practical approach to modeling the combustion of real fuels, including JP10 and Jet A. For temperature conditions above 1000 K, the pyrolysis of a hydrocarbon fuel is quite decoupled from the oxidation process of the small intermediate products which can be modelled at an affordable computational cost in CFD simulations. The pyrolysis process of the real fuel, in which it breaks down into small intermediate species, can be lumped into just a few reactions. The HyChem model can be taken as the combination of two submodels, fuel pyrolysis and oxidation of the pyrolysis products, the latter of which is also called the foundational chemistry. The schematic of this approach is illustrated in Figure 6.

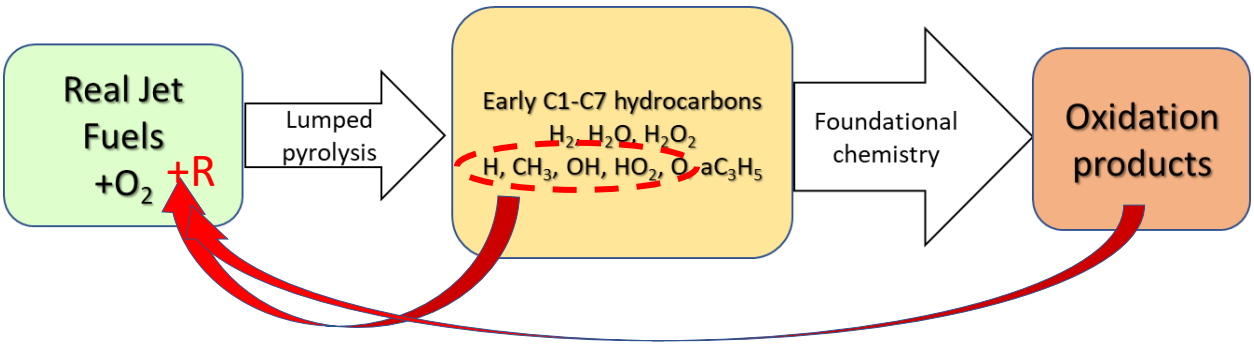

Figure 6: Illustration of the HyChem approach.

The current version of the HyChem model uses the USC Mech II as the oxidation submodel, while the fuel pyrolysis submodel was derived from experimental results obtained from time-resolved shock tube pyrolysis studies of the Hanson group and the flow reactor pyrolysis studies of Prof. Tom Bowman's group. The method for fitting the stoichiometric coefficients and rate parameters of each reaction in the fuel pyrolysis submodel takes many steps and is detailed in the HyChem paper [27]. Here, we briefly introduce the method used for Jet A.

The Jet A (POSF#10325) HyChem model consists of 119 species and 841 reactions. C_2H_4, C_3H_6, 1-C_4H_8, *i*-C_4H_8, CH_4, C_6H_6, C_7H_8, and H_2 are identified as the critical species based on the flow reactor results. The species C_2H_2, pC_3H_4, C_4H_6, and other small stable intermediates are not considered "key" species because they are assumed to be formed from the key species listed above, and are well decoupled from fuel pyrolysis. The lumped pyrolysis reactions for conventional petroleum-derived jet fuels, such as JP-8, Jet A and JP-5, are in the form of:

$$C_mH_n \rightarrow e_d\,(C_2H_4 + \lambda_3\,C_3H_6 + \lambda_{4,i}\,i\text{-}C_4H_8 + \lambda_{4,1}\,1\text{-}C_4H_8) + b_d\,[\,\chi\,C_6H_6 + (1-\chi)\,C_7H_8] + \alpha\,H + (2-\alpha)\,CH_3 \qquad \text{(R1)}$$

$$C_mH_n + R \rightarrow RH + \gamma\ CH_4 + e_a\,(C_2H_4 + \lambda_3\ C_3H_6 + \lambda_{4,i}\ i\text{-}C_4H_8 + \lambda_{4,1}\ 1\text{-}C_4H_8)$$

$$+ b_a\,[\chi\ C_6H_6 + (1-\chi)\ C_7H_8] + \beta\ H + (1-\beta)\ CH_3 \qquad \text{(R2)}$$

where λ_3, $\lambda_{4,i}$, $\lambda_{4,1}$, χ, α, β and γ are stoichiometric parameters whose values were determined experimentally in the Stanford shock tubes and flow reactor , and e_d, e_a, b_d and b_d are variables that can be determined from λ_3, $\lambda_{4,i}$, $\lambda_{4,1}$, χ, α, β and γ by elemental conservation. The possible species that R represents are H, CH_3, OH, O_2, HO_2, O. Therefore, there are 7 reactions in the fuel pyrolysis submodel. Among the coefficients, λ_3 represents the ratio of C_3H_6 to C_2H_4, λ_4 is the ratio of C_4H_8 to C_2H_4, χ is the ratio of C_6H_6 to the sum of C_6H_6 and C_7H_8, γ accounts for the yield of CH_4 aside from those formed through H-abstraction by the CH_3 radical (when γ is then generally considered 0), and α and β are the branching ratios of the H atom to the CH_3 radicals from reactions R1 and R2, respectively. R1 is the pyrolysis following the initial radical formation by the fuel, while R2 represent the pyrolysis following the H abstraction reaction of the fuel. The coefficients λ_3, $\lambda_{4,i}$, $\lambda_{4,1}$, and χ can be directly estimated from the flow reactor, while α, β, γ can be derived from shock tube time history profile of CH_4 and C_2H_4. The equations for elemental balance are

$$m = e_d(2 + 3\lambda_3 + 4\lambda_4) + b_d(7 - \chi) - \alpha + 2 \qquad (3.12)$$

$$\frac{n}{2} = e_d(2 + 3\lambda_3 + 4\lambda_4) + b_d(4 - \chi) - \alpha + 3 \qquad (3.13)$$

$$m = e_a(2 + 3\lambda_3 + 4\lambda_4) + b_a(7 - \chi) + \gamma - \beta + 1 \qquad (3.14)$$

$$\frac{n}{2} = e_a(2 + 3\lambda_3 + 4\lambda_4) + b_a(4 - \chi) + 2\gamma - \beta + 2 \qquad (3.15)$$

They can be converted into

$$e_d = \frac{\left[-(4-\chi)m + \frac{(7-\chi)}{2}n + 3\alpha + \chi - 13\right]}{3(2+3\lambda_3+4\lambda_4)} \qquad (3.16)$$

$$e_a = \frac{\left[-(4-\chi)m + \frac{(7-\chi)}{2}n + 3\beta - (10-\chi)\gamma - (10-\chi)\right]}{3(2+3\lambda_3+4\lambda_4)} \qquad (3.17)$$

$$b_d = \frac{1}{3}\left(m - \frac{n}{2} + 1\right) \qquad (3.18)$$

$$b_a = \frac{1}{3}\left(m - \frac{n}{2} + \gamma + 1\right) \qquad (3.19)$$

where $\lambda_4 = \lambda_{4,1} + \lambda_{4,i}$. The species ratios λ_3, λ_4, and χ are all obtained from the flow reactor speciation data from Dr. Bowman's group at Stanford University, in which GC-TCD is used to measure all the species. The coefficients α, β and γ, as well as the rate parameters are fit from time resolved shock tube data of CH_4 and C_2H_4 from Dr. Hanson's group at Stanford University (which includes both pyrolysis and oxidation). All the coefficients are thus obtained with the restriction of being limited to integer numbers, $m = 11$, $n = 22$ for Jet A. The real Jet A has an average molecular formula $C_{11.37}H_{21.87}$. Therefore, when we want to input *x* ppm of Jet A fuel $C_{11.37}H_{21.87}$ in the simulation, we actually need to tell the simulation software 1.028**x* ppm of $C_{11}H_{22}$ instead in order to have the same mass.

The JP10 HyChem model was constructed in a similar fashion, but with some differences in details. The main decomposition products are C_2H_4, C_3H_6, cyclopentadiene (C_5H_6), benzene (C_6H_6), and toluene (C_7H_8). The radicals formed through "direct" pyrolysis also include a significant amount of allyl radicals (aC_3H_5). The main reactions are:

$$C_{10}H_{16} \rightarrow e_d\,(C_2H_4 + \lambda_3\,C_3H_6 + \lambda_5\,C_5H_6 + \lambda_0\,H_2) + b_d\,[\,\chi\,C_6H_6 + (1-\chi)\,C_7H_8] + \alpha\,H + \gamma\,aC_3H_5 + (2-\alpha-\gamma)\,CH_3 \quad \text{(R3)}$$

$$C_{10}H_{16} + R \rightarrow RH + e_a\,(C_2H_4 + \lambda_3\,C_3H_6 + \lambda_5\,C_5H_6 + \lambda_0\,H_2) + b_a\,[\,\chi\,C_6H_6 + (1-\chi)\,C_7H_8] + \alpha\,H + \gamma\,aC_3H_5 + (2-\alpha-\gamma)\,CH_3 \quad \text{(R4)}$$

The parameters e_d, e_a, b_d and b_a are stoichiometric coefficients that can be derived from λ_3, λ_5, λ_0, χ, α, β, γ, and θ using elemental balance, while the latter group of parameters are directly fit from species profiles. The details are given in the original paper for the HyChem Model of JP10 [78].

3.3 REACTOR MODEL

All the shock tube experiments are compared against simulations of the test gas in a closed homogeneous 0-D reactor in the "Constrain Pressure and Solve Energy Equation" mode using

CHEMKINPRO [79]. Since there is no transport effect, mass flux, or surface chemistry effect from the wall in the homogeneous reactor, the basic equations can be simplified to[79]

$$(\rho V)\frac{dT}{dt}\left(\sum_{k=1}^{K} Y_k c_{pk}\right) = -V\sum_{k=1}^{K}(h_k \dot{w}_k)\mu_k + V\frac{dP}{dt} \qquad (3.20)$$

$$\dot{w}_k = \sum_{i=1}^{I}(v''_{ki} - v'_{ki})\left(k_{fi}\prod_{k=1}^{K}[X_k]^{v'_{ki}} - k_{ri}\prod_{k=1}^{K}[X_k]^{v''_{ki}}\right) \qquad (3.21)$$

Eq (3.21) basically comes from Eq (3.7), but with *X* (reactants) and *Y* (products) using the same list of species. ρ is the density of the mixture gas; *V* is the volume of the mixture gas; *P* is the pressure of the mixture gas; μ_k is the molecular weight (molar mass) of species *k*; $c_{pk}$is the specific heat of species *k*; h_k is the specific enthalpy of species *k*; Y_k is the mass fraction of species *k*; v'_{ki} is the stoichiometric coefficient of reactant X_k; v''_{ki} is the stoichiometric coefficient of product X_k; k_{fi} is the forward rate constant of reaction *i*; k_{ri} is the reverse rate constant of reaction *i*.

One needs to be aware that in the conventional approach, we simulate every reaction process at a constant pressure condition, letting the second term on the right side of energy equation Eq (3.20) be 0. But in reality, the pressure profile is not perfectly flat with time and will experience a rarefaction wave and a pressure drop. This real process, as mentioned earlier, is simulated by leaving the second term in Eq (3.20) in the equation. Then, a dilute test gas experiences an almost isentropic change of an ideal gas, which follows

$$\left[\frac{P(t)}{P(0)}\right]^{\frac{\gamma-1}{\gamma}} = \left[\frac{T(t)}{T(0)}\right] \qquad (3.22)$$

where $P(0)$, $T(0)$ stand for the initial state of the gas immediately after the shock wave passes, while $P(t)$, $T(t)$ is the state of the gas at time t. Note that this is an assumption made for cases when fuel is dilute and the diluent is an inert gas. However, it does not matter to CHEMKINPRO whether it is dilute or of high fuel mole fraction. CHEMKINPRO imposes the pressure profile that the user provides and solves the energy equation Eq 3.20 (in fact, the equation given by the CHEMKINPRO manual is more complicated, but here we simplified it for easier understanding).

3.4 MONTE CARLO ANALYSIS

For further analysis of the HyChem models, Monte Carlo analysis was done to evaluate the effect of each rate parameter in the reaction models. In each simulation, the A factors or the activation energies E_a of all, or a subset, of the reactions being studied were varied randomly and independently in a predefined distribution. The software package for the Monte Carlo analysis was originally built as described in Fridlyand et al. [80] and used with small modification here. For A factors, we used a uniform distribution in the range of ±30% of the original value in the model. The reason for the choice of this uncertainty is explained well in [80,81]. Generally, almost all reactions in well-known kinetic models have uncertainties higher than ±30%. This Monte Carlo analysis is to see how sensitive the model predictions are to a certain level of uncertainties.

Therefore ±30% is chosen without considering the actual uncertainties of the parameters. For the activation energies, we used a normal distribution with 5% of the original value as the 2σ uncertainty. There are some studies [82,83] using the specific uncertainties of rate parameters e.g. with limited number of reactions. Judging the actual values of the E_a uncertainties given in these studies, the choice of 5% is a reasonable level of guess for general sensitivity analysis purpose. For a simulation, e.g. Monte Carlo analysis of Jet A pyrolysis from 900 K to 2100 K, we choose a set of temperature points, e.g. 900 K, 940 K, 980 K, …., and ran 2000 simulations with the newly sampled parameters at each temperature point. In other words, the parameter values of any one of the 2000 runs at a temperature point will not be used again at another temperature point. Note that the A factor and E_a are independent with each other, while in reality, there are always some correlations between the rate parameters. Pearson correlation and Spearman correlation analysis are performed to evaluate effect of each rate parameter to a specific species output.

The Pearson correlation coefficient [84] measures the linear correlation between two variables X and Y. It can be calculated by

$$\rho_{X,Y} = \frac{\mathrm{cov}(X,Y)}{\sigma_X \sigma_Y} \qquad (3.23)$$

where σ_X, σ_Y are the standard deviations of X and Y, respectively. $\mathrm{cov}(X,Y)$ is the covariance of X and Y.

Another method to measure correlations is the Spearman's rank correlation coefficient[85,86], which can also measure nonlinear correlations, by converting X and Y to rank variables [86] rg_X

and rg_Y, and then apply them to the Pearson coefficient. The Spearman's rank correlation coefficient can be expressed as

$$r_s = \frac{\mathrm{cov}(\mathrm{rg}_X, \mathrm{rg}_Y)}{\sigma_{\mathrm{rg}_X}\sigma_{\mathrm{rg}_Y}} \qquad (3.24)$$

The Spearman measure of correlation was selected to report the correlations between species formation and rate parameter values in this thesis due to its capability to capture non-linear relations.

The Monte Carlo analysis in this framework is considered to be a sensitivity analysis more than an uncertainty analysis, since the uncertainty of the rate parameters should be obtained from the experimental data that yielded these parameter values.

3.5 DATA PROCESSING AND STATISTICAL METHODS

3.5.1 SOME BASICS OF STATISTICS

The combustion community has been embracing more and more uncertainty evaluation over the recent years. The reason is that, while people have a more mature understanding of the reaction pathways, precise determination of the rate parameters has met challenges. Data from different groups interpret different values for the same set of parameters, and the data themselves are often scattered. Quantified uncertainty information for each experimental data set is needed to enable

kinetic modelers more understanding of the model they build based on these data. Here, we give some basics of the statistics used in this work. The following text is an introduction to the basic mathematics involved in variance and uncertainty analysis. They will be used when estimating the uncertainty of a variable and the propagation of that uncertainty to other variables.

Given two independent variables, X_1, X_2, with expectation values $E(X_1)$, $E(X_2)$, and variance $\mathrm{Var}(X_1)$, $\mathrm{Var}(X_2)$, with k as a constant, then [87]

$$\mathrm{Var}(kX_1) = k^2\mathrm{Var}(X_1) \qquad (3.25)$$

$$\mathrm{Var}(X_1 + X_2) = \mathrm{Var}(X_1) + \mathrm{Var}(X_2) \qquad (3.26)$$

$$\mathrm{Var}(X_1X_2) = [E(X_1)]^2\mathrm{Var}(X_2) + [E(X_2)]^2\mathrm{Var}(X_1) + \mathrm{Var}(X_1)\mathrm{Var}(X_2) \qquad (3.27)$$

One can use the above equations to derive the variance of a variable, e.g. temperature, yield of species, from other variables, e.g. velocity, time, GC response factors, that are more directly measured.

If a variable x follows a Gaussian distribution (which is common in nature, and a good approximation for many cases) with mean $\bar{x}$ and variance of σ^2, then the 95% confidence interval of x will be close to $\bar{x} - 2\sigma, \bar{x} + 2\sigma$. Thus, the 95% confidence interval is sometimes presented as the 2σ-uncertainty, which is used in HyChem papers. Quite often a variable can be approximated with a Gaussian distribution, which can be used to first obtain the variance of a variable, written as $\mathrm{Var}(x)$ or σ^2, and then use the 2σ value to get the 95% confidence interval.

Quite often in our experiments when we measure the value of a variable, e.g. end wall velocity, we have a limited sample size (only 5 velocities, and 6 arrival times for end wall velocity estimation) that is not enough to make approximations of a Gaussian distribution. Instead, a Student *t*-distribution, which is used to estimate the confidence interval of a variable with a normal distribution when only a small number of samples are provided, will be used in this case. For a set of sample values $x_1, x_2, \dots, x_n$, the 95% confidence interval of *x*, which corresponds to the 2-σ uncertainty can be calculated as [87]:

$$\bar{x} \pm \frac{t_{0.025,n-1} s}{\sqrt{n}} \qquad (3.28)$$

where $t_{0.025,n-1}$ is the upper 2.5% critical point of a *t*-distribution with $n-1$ degrees of freedom (also called *t*-value). It can be calculated by computer algorithms or searched from a t-value table. The sample standard deviation s satisfies $s^2 = \frac{1}{n-1}\sum_{i=1}^{n}(x_i - \bar{x})^2$.

Consider the case for linear or nonlinear regression with only one independent variable *x*, which is the case for the velocity extrapolation. The confidence interval for the predicted value of y^* for any x^* can be calculated by *t*-statistics when the sample size is small. For any regression curve, $y = f(x)$, with samples of $(x_1, y_1), (x_2, y_2), \dots, (x_n, y_n)$, the confidence interval of y^* at $x = x^*$ is [88]

$$\hat{y} \pm t_{n_{df}} \left[\frac{\sum_{i=1}^{n}(y_i^* - y_i)^2}{n_{df}}\right] \sqrt{1 + \frac{1}{n} + \frac{(x^* - \bar{x})^2}{\sum_{i=1}^{n}(x_i - \bar{x})^2}} \qquad (3.29)$$

where $\hat{y}$ is the value of the predicted y^* from the fitted equation $y = f(x)$, at $x = x^*$; y_i^* $(i = 1,2, \dots, n)$ is the predicted values from $y = f(x)$ at $x = x_i$. $t_{n_{df}}$ is the *t*-value for 95% confidence interval, with n_{df} as the degree of freedom, as introduced earlier. Generally, $n_{df} = n - n_c$, where n_c is the number of parameters in $f(x)$. For linear regression, $n_{df} = n - 2$. The above calculation of confidence interval is used in the LPST temperature uncertainty and species uncertainty analysis.

3.5.2 SMOOTHING METHODS

There is a need for precise characterization of the pressure trace profile. For each pressure trace, the raw data is smoothed with a median filter [89], and then a horizontal cut-line(s) is applied to detect the time of shock arrival. The raw data of the post-shock pressure trace (the data without being smoothed by median filter) is then smoothed by a gaussian kernel local constant (or local linear) regression method [90]. The starting pressure of the shock wave is quite important for precise characterization of the temperature history for which Eq (3.22) is used. However, the signal is very noisy at the time of arrival of shock in the raw data, and the signal smoothing has a boundary problem that will be disturbed by the data points that actually record the rising pressure within the thin shock wave instead of the noise. There may be better approaches to determine the starting pressure of the shock from the transducer. However, the practical and effective method described above has been used. The fitted smooth curve is reviewed by eye to see if it is consistently in the center of the noisy band.

Note that the pressure before shock arrival P_1 is needed in building the post-shock profile from the pressure trace. The starting pressure shown in the pressure traces are usually around 0, but often slightly above it. This above-zero pressure is assumed to correspond to the P_1 we measured through the pressure gauge on the driven section of the shock tube.

Note that smoothing methods can be also applied to our speciation profile given decent continuity of points (not many holes). This can also generate a confidence band with temperature (basically using Eq (3.29), in order to characterize our uncertainties of the speciation profile. However, in this thesis, we will stick on the uncertainty of species mole fraction and temperature obtained from each individual shock.

The methods discussed in Section 3.5.1 and Section 3.5.2 will be used in the analysis in Chapter 6 for the temperature characterization and uncertainty analysis.

4 JET A PYROLYSIS EXPERIMENTS AND SIMULATION

4.1 JET A PYROLYSIS IN THE HPST

A significant portion of the work presented in this section is to be published in [81] which is in press.

4.1.1 EXPERIMENTAL RESULTS

Dilute pyrolysis experiments of 52.3 ppm Jet A in argon were conducted at 25 atm and 90 atm in the HPST. The nominal reaction time was 2.3 ms. The reported Jet A mole fraction of 52.3 ppm is obtained from the CO_2 conversion experiment, which is 9.4% less than the predicted value from the preparation of the fuel/Ar mixture. There is some evidence that indicates the fuel in the shock tube is not significantly changed from the original Jet A. An explanation of this statement is given in Appendix E. The experimental results from the HPST show that at the pressures tested, the major stable product species are CH_4, C_2H_4, C_2H_2, C_2H_6, C_3H_6, pC_3H_4 (propyne), aC_3H_4 (allene), 1-C_4H_8, *i*-C_4H_8, 1,3-C_4H_6, C_4H_2 (diacetylene), C_4H_4 (vinylacetylene), cyclopentadiene, 1,3,5-hexatriyne, benzene, and toluene. Figure 7 presents the results for selected species. As can be seen in the Figure 7, the experiments at the two pressure conditions show nearly the same results. In what follows, we will primarily use the data from 25 atm for discussion.

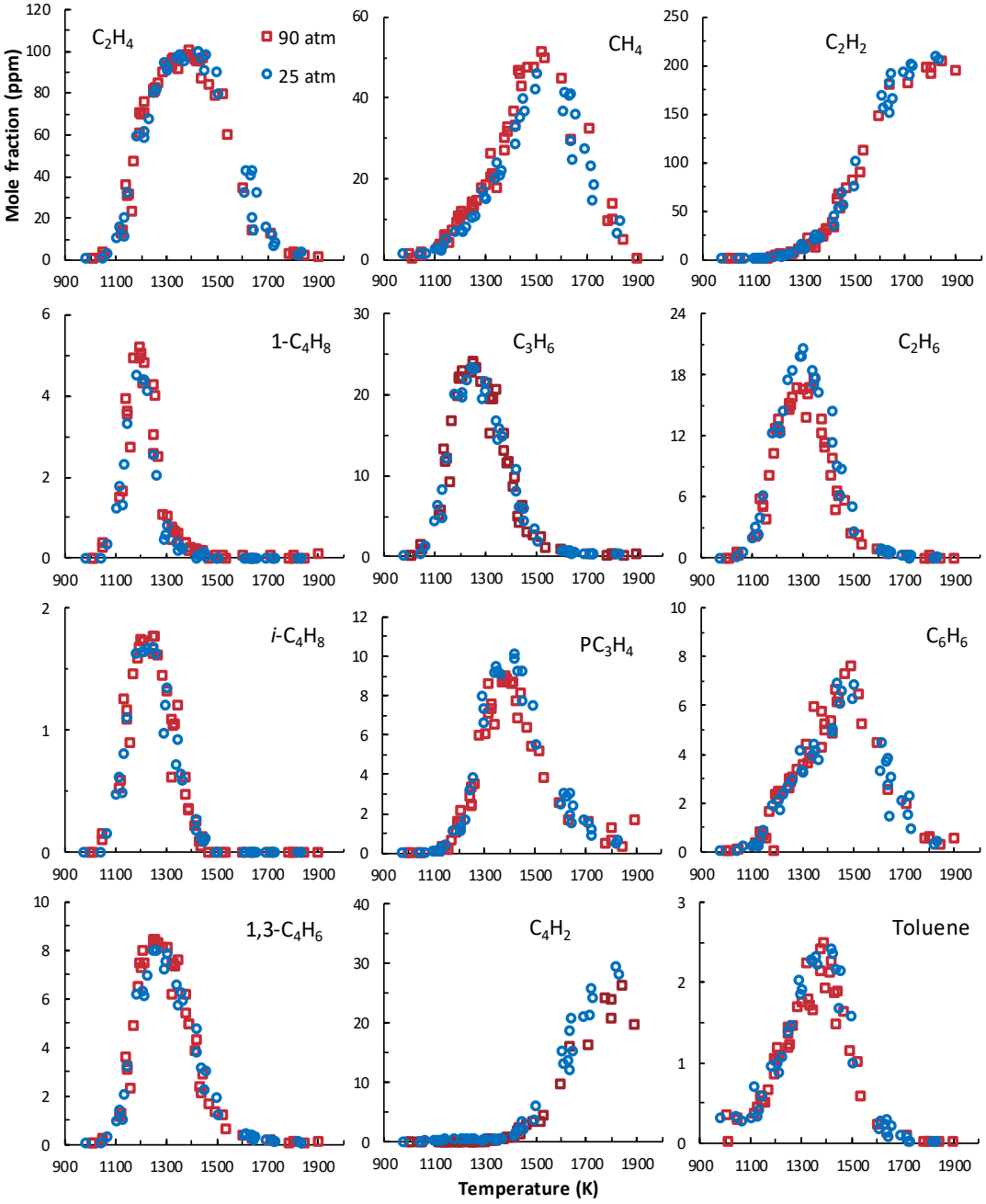

Figure 7. Species measured at 25 and 90 atm post shock pressures (P_5) and at 900 – 2000 K post shock temperatures (T_5). Initial fuel mole fraction of Jet A is 52.3 ppm in argon.

Ethylene is the dominant species below 1450 K. It starts to be formed at around 1050 K, and rises to its peak value at ~1350 K. As the temperature rises further, C_2H_2 becomes the dominant species.

There is an assumption introduced earlier [25,27] and supported by the data shown here: C_2H_4, as well as CH_4, C_2H_6, C_3H_6, 1-C_4H_8, *i*-C_4H_8, benzene, and toluene are the key species formed below ~1400 K. The peak concentrations of C_2H_4, C_3H_6, 1-C_4H_8, and *i*-C_4H_8 are in a decreased order, even after conversion to their contributions to the total ppm of carbon (carbon total). CH_4, C_2H_6, benzene, and toluene all contribute significantly to the total carbon count. CH_4, benzene, and toluene are quite stable, and are still present in significant amounts at high temperatures. On the other hand, the concentration of 1-C_4H_8 starts to decrease around 1200 K because of its decomposition just like C_2H_4, aC_3H_4 and pC_3H_4 which eventually decompose and are converted to C_2H_2, diacetylene, or polyacetylenes above 1400 K.

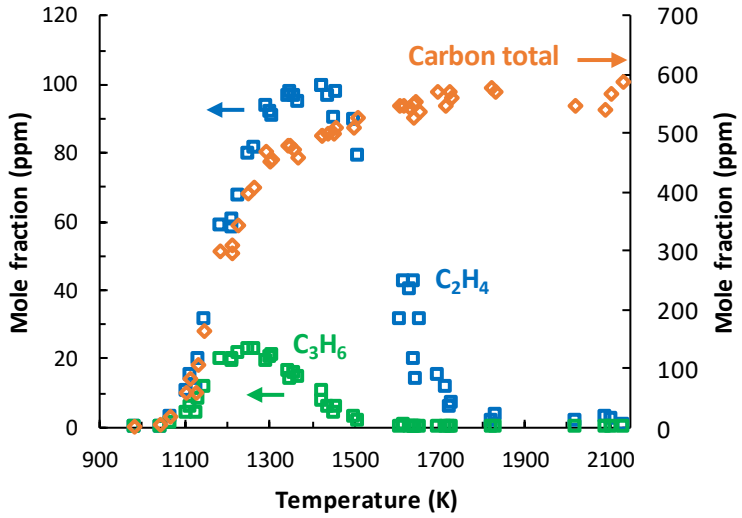

Figure 8. Formation of C_2H_4 and C_3H_6 compared to the carbon total of all major species from pyrolysis of 52.3 ppm Jet A in argon at 25 atm with 2.3 ms of reaction time.

The carbon total based on all the major products, which are the species shown in Figure 7 and also vinylacetylene, allene, cyclopentadiene, 1,3,5-hexatriyne, is plotted against shock temperature in

Figure 8. It shows that the fuel decomposition starts at around 1050 K, the same temperature at which C_2H_4 starts to appear. At 1300 K, almost all the initial jet fuel components have broken down in about 2.3 ms reaction time to the small product species since the carbon profile flattens at this temperature around 570 ppm, which is about 96% of the initial fuel's carbon total based on the CO_2 measurement. The findings further support the assumptions of the HyChem approach: almost all the jet fuel components break down into a small number of small species rapidly at relatively low temperature compared to the combustion reaction temperature.

It should be noted that a careful comparison of the experimental data between the two pressures shows some dependency of the production of C_2H_6 and C_4H_2 on pressure. C_4H_2 production is somewhat smaller at 90 atm than at 25 atm, though the difference is small.

4.1.2 COMPARISON BETWEEN THE MODEL AND EXPERIMENTS

Simulations using the HyChem model were compared with the current experimental data. Considering that the model parameters were derived earlier from shock tube and flow reactor experiments [27] under thermodynamic conditions significantly different from those of the current experiments, the agreement between the current experimental data and model predictions is good. Figure 9 shows the comparisons of major species. Overall, the predictions are in reasonable agreement with the experimental data for C_2H_4, CH_4, pC_3H_4, aC_3H_4 (not shown) and C_2H_2. Other key species, including C_3H_6 and 1-C_4H_8 (not shown) are not as well predicted. For example, the

model over-predicts the peak concentration of C_3H_6 by about 50%. It also overpredicts benzene and toluene concentrations quite significantly, while 1,3-butadiene is underpredicted.

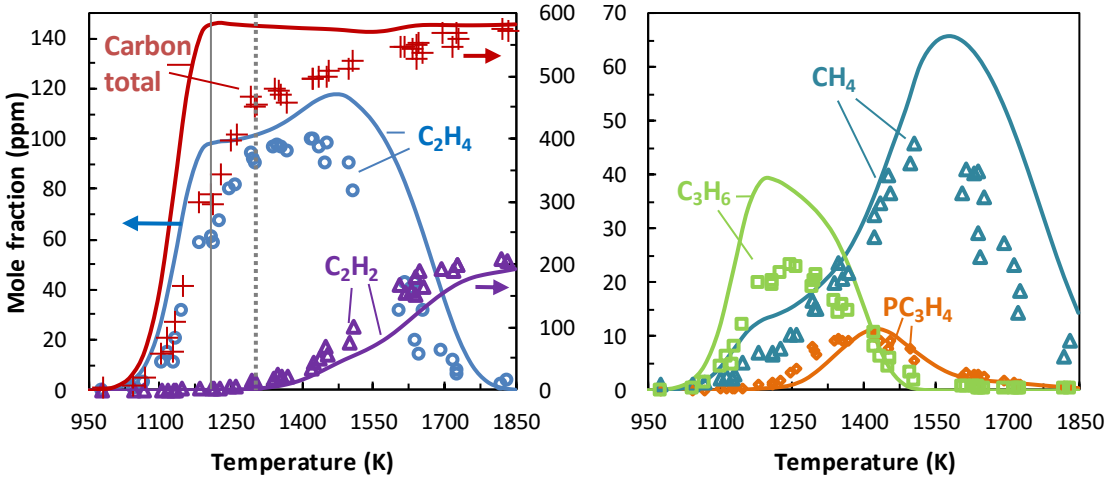

Figure 9. Comparisons of selected experimental (symbols) and predicted (lines) species concentrations in the pyrolysis of 52.3 ppm Jet A in argon at 25 atm with 2.3 ms of reaction time. The gray vertical lines represent the approximate temperature where the ethylene concentration profile first flattens with respect to temperature for simulations (solid) and experiments (dash).

The model predicts a fast fuel decomposition rate as evidenced by the comparison of carbon total profiles (Figure 9). Likewise, the rise in the predicted C_2H_4 concentration is also more rapid than the experiment. The peak value of C_2H_4 from model prediction occurs at around 1500 K, which is slightly higher than that determined by the experiment. That peak concentration predicted for ethylene is also slightly higher than the experiment. Toward higher temperatures (>1500 K), the C_2H_4 concentration becomes sensitive to the accuracy of the foundational chemistry because of the conversion of C_2H_4 to C_2H_2.

Despite the difference in the model predictions and the experimental results, an examination of the carbon total and C_2H_4 profiles indicates that both the model and experiment show that the consumption of the fuel is entirely coupled with the production of C_2H_4. When the production of C_2H_4 levels off with respect to temperature, fuel decomposition is also complete. The turning point is shown in Figure 9 by the two vertical lines corresponding to the temperatures at which the ethylene concentration profile first flattens with respect to temperature. The experimental results show that the carbon total due to the major species still rises as a function of temperature, while the model prediction reaches the plateau value at around 1200 K.

The pressure dependency of the model is also tested, as shown in Figure 10. Overall, it predicts little pressure dependency like what the experiments showed. The pressure dependency primarily lies in the high temperature region that is controlled by foundational chemistry.

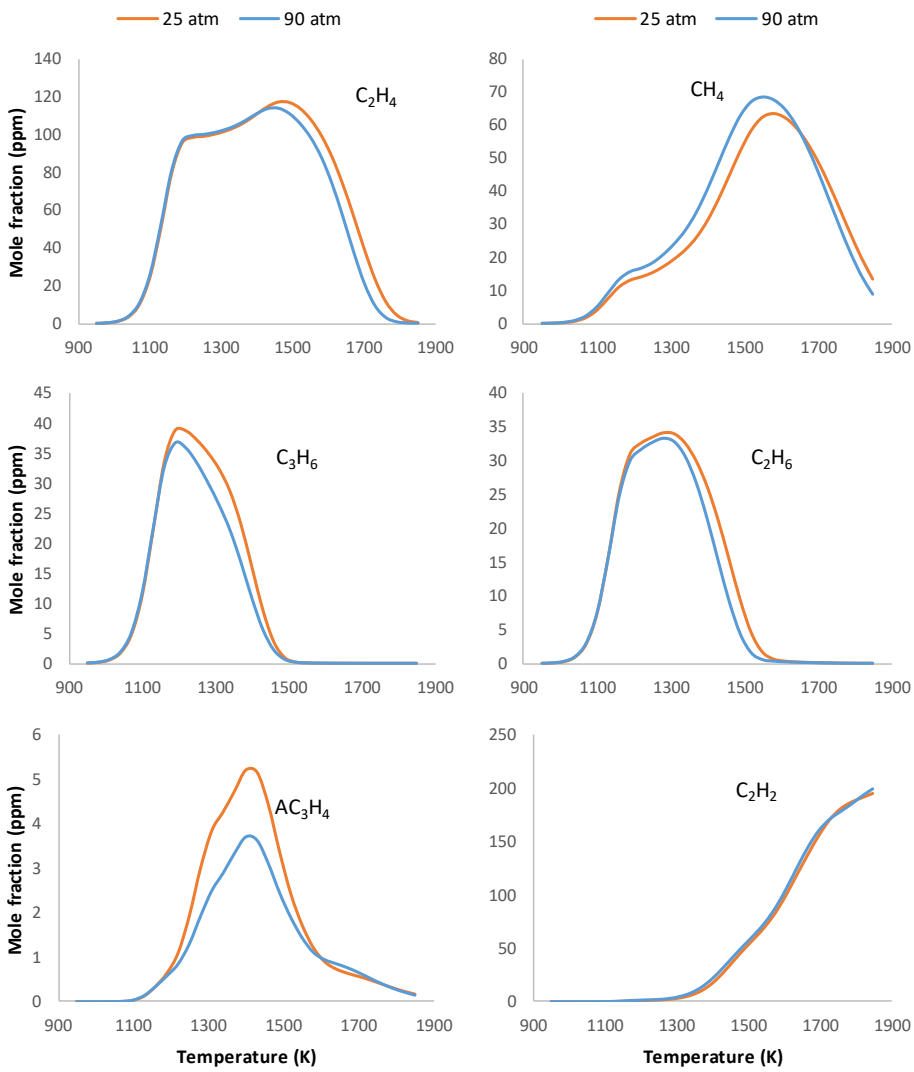

Figure 10: Comparison of the HyChem model predictions at 25 atm and 90 atm for the pyrolysis of 52.3 ppm Jet A in argon with 2.3 ms of reaction time.

Overall, there are general agreements between the model and the experiment on the important species that have an impact on the subsequent oxidation chemistry in an oxidizing environment. The main difference between the experiment and model is that the model predicts a faster fuel decomposition with respect to temperature.

As discussed earlier, the HyChem model parameters were derived from the Stanford shock tube and flow reactor experiments over the pressure range of 1 to 15 atm. For the discrepancy observed between the model and the current experiment, there are a few potential causes that could contribute to the discrepancies. First, the shock tube data used for HyChem parameter determination are somewhat inconsistent with the data from the current study. A systematic error in temperature evaluation and species evaluation in one or more apparatuses among the shock tubes from two laboratories and the flow reactor may cause this problem. The temperature used in the HPST in this study is obtained from chemical thermometer calibration using Matsugi's rate parameters for TFE. This may cause certain errors as will be discussed in Chapter 6. For the Stanford shock tube, the species measurement by laser diagnostic techniques becomes increasingly unreliable and tends to get erroneously higher than the actual species fraction as the temperature rises. In fact, only below 1400 K is the data from Stanford shock tubes used to fit or validate the model. However, it is possible that below 1400 K there are still some discrepancies in temperature. These two factors can explain the temperature discrepancy in the predicted species below 1400 K, since the rate parameters are primarily fitted against shocks from Stanford shock tubes in this temperature region. Another reason for the discrepancy in this temperature region is that the model does not align well with the Stanford shock tube data itself. This is evident in the following figure from the HyChem paper [27]:

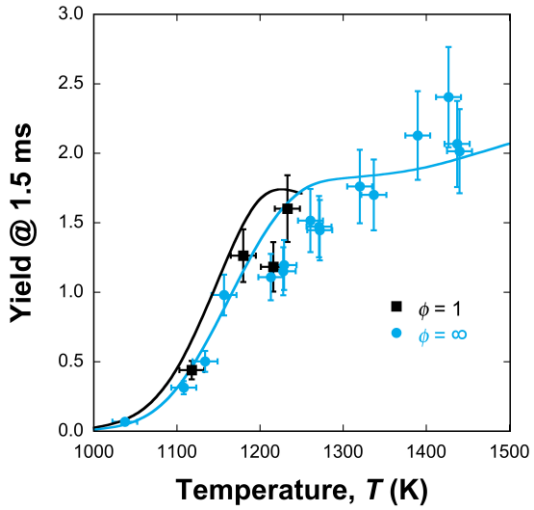

Figure 11: Experiments (symbols) and simulations (lines) of C_2H_4 yield (the ratio between species mole fraction and the initial fuel mole fraction) from the oxidation and pyrolysis of 0.4% Jet A in Ar at 1.6 atm in the Stanford shock tube, illustrated as a species-temperature profile. This figure is directly from the HyChem paper [27] **with permission from Elsevier https://www.elsevier.com/, as a coauthor.**

This figure actually shows that the Stanford shock tube data are more consistent with our data from UIC shock tube than the model is. The data from both shock tube groups tend to be lower than what the model predicts. As shown in Figure 11, the overprediction of the model for C_2H_4 is quite evident for the condition given in the figure.

The reason for the discrepancy at higher temperatures (>1400 K) in Figure 9 should be mostly due to the inconsistency of the USC Mech II submodel which is not directly fitted from the data in this HyChem project.

Furthermore, the assumption that the main fuel pyrolysis reaction will always proceed with the same parameters (including the rate parameters and the stoichiometric coefficients) and that the fuel will all be directly converted to the small product species in the reaction may contribute to the

discrepancies. The carbon total plot in Figure 9 clearly shows that the fuel cannot fully decompose into the set of products defined by the model at below 1550 K. A future study utilizing GCxGC-TOFMS with the shock tubes could possibly examine this hypothesis. At this point, we observed some discrepancies of the model between experiments and simulations in both quantitative and qualitative ways. However, the general trend of the pyrolysis in the experiments, especially for the formation of C_2H_4 which is the most important species for combustion process simulations, can still be captured by the model. A further analysis of the model will be given in the next section.

4.1.3 MONTE CARLO SENSITIVITY ANALYSIS

While the causes of the discrepancies between model and experiments are still being investigated, we performed a Monte Carlo analysis of the rate parameters of all the reactions in the model with respect to the experiments at 25 atm to examine the effect of uncertainty of the rate parameters on the discrepancies between model predictions and experiments. The Monte Carlo simulations comprise two sets, each of which cover a range of temperature with 2000 model samples for each temperature. In the first set, the A factor of every reaction was varied randomly by a uniform distribution in the ±30% band from the nominal rate value. In the second set, the activation energies were randomly varied, with a Gaussian distribution using 5% as the 2σ uncertainty. Additionally, the effect of the rate parameter uncertainties of both the fuel pyrolysis submodel and foundational chemistry submodel were also separately studied. In this additional investigation, only one submodel's parameters were randomly changed for each simulation. The results of all the Monte Carlo analysis described above are given in Figure 12.

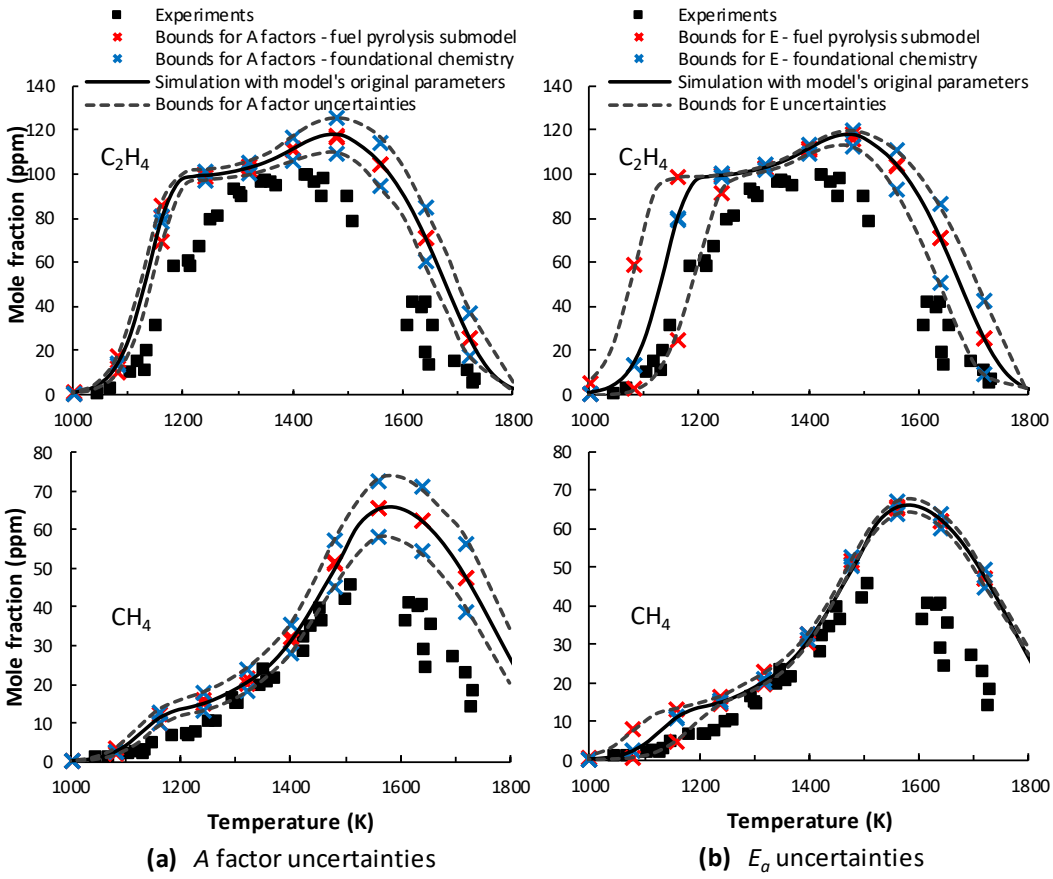

Figure 12. Monte Carlo results of the sensitivities of C_2H_4 and CH_4 to (a) the *A* factor and (b) the activation energy E_a. Symbols are experimental data at 25 atm. Solid lines are nominal predictions, and dashed lines represent 95% confidence intervals from (a) the *A* factor sampling within a ±30% uniform distribution for each *A* factor and (b) E_a sampling with a Gaussian distribution using 5% as the 2σ. The colored symbols represent bounds when the rate parameters of either only the fuel pyrolysis submodel (red) or only the foundational chemistry submodel (blue) are varied.

Uncertainties in the *A* factor could play a significant role in the high temperature region, while it shows a very weak effect on the rise of the C_2H_4 and CH_4 concentrations in the low temperature region. In this same temperature regime, the productions of C_2H_4 and CH_4 are more sensitive to the activation energy. At low temperatures, the band from the 5% uncertainties in E_a covers the experimental results of C_2H_4 and to a large extent, also CH_4. A clear separation of the influence of

the fuel pyrolysis submodel and that of the foundational chemistry submodel along different temperature regions is also observed. In Figure 12, in the low temperature region, the red symbols (simulation with fuel pyrolysis submodel uncertainties) overlap with the dashed lines for the cases of both *A* factor and E_a, while the blue symbols (simulation with foundational chemistry submodel uncertainties) overlap with the solid lines. This type of overlap indicates that the low temperature region is dominated by the fuel pyrolysis lumped reactions, and that the uncertainty from the foundational chemistry has negligible effect. In contrast, in the high temperature region, the blue symbols overlap with the dashed lines, while the red symbols overlap with the solid line. This overlap of blue symbols indicates that in the high temperature region, the foundational chemistry becomes the dominant submodel, while the uncertainties from the fuel pyrolysis submodel show negligible effect on the species output. The Monte Carlo analysis also shows that the experiments and model is in best agreement for a species when it has low sensitivity to both submodels in that region (around 1350 K for C_2H_4 and around 1400 K for CH_4). Overall, the Monte Carlo analysis shows the different effects of the two submodels at different temperature regions.

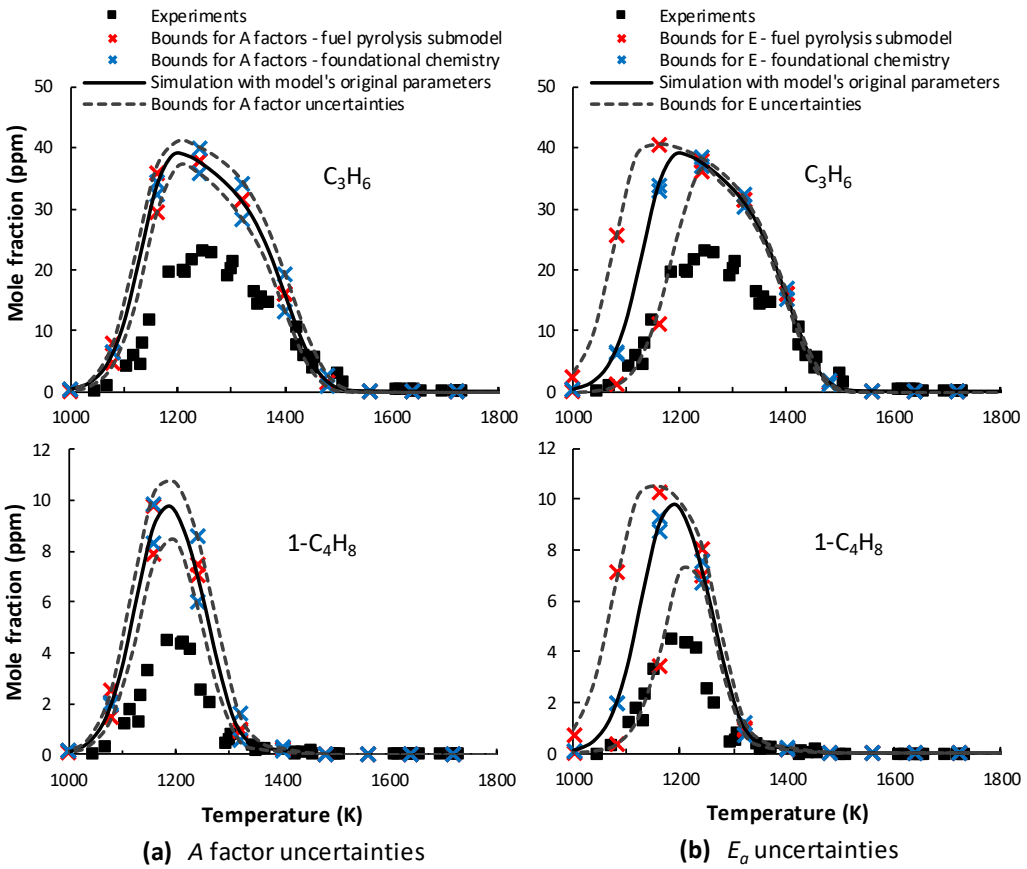

Figure 13: Monte Carlo results of the sensitivities of C_3H_6 and 1-C_4H_8 to (a) the *A* factor and (b) the activation energy E_a. Symbols are experimental data at 25 atm. Solid lines are nominal predictions, and dashed lines represent 95% confidence intervals from (a) the *A* factor sampling within a ±30% uniform distribution for each *A* factor and (b) E_a sampling with a Gaussian distribution using 5% as the 2σ. The colored symbols represent bounds when the rate parameters of either only the fuel pyrolysis submodel (red) or only the foundational chemistry submodel (blue) are varied.

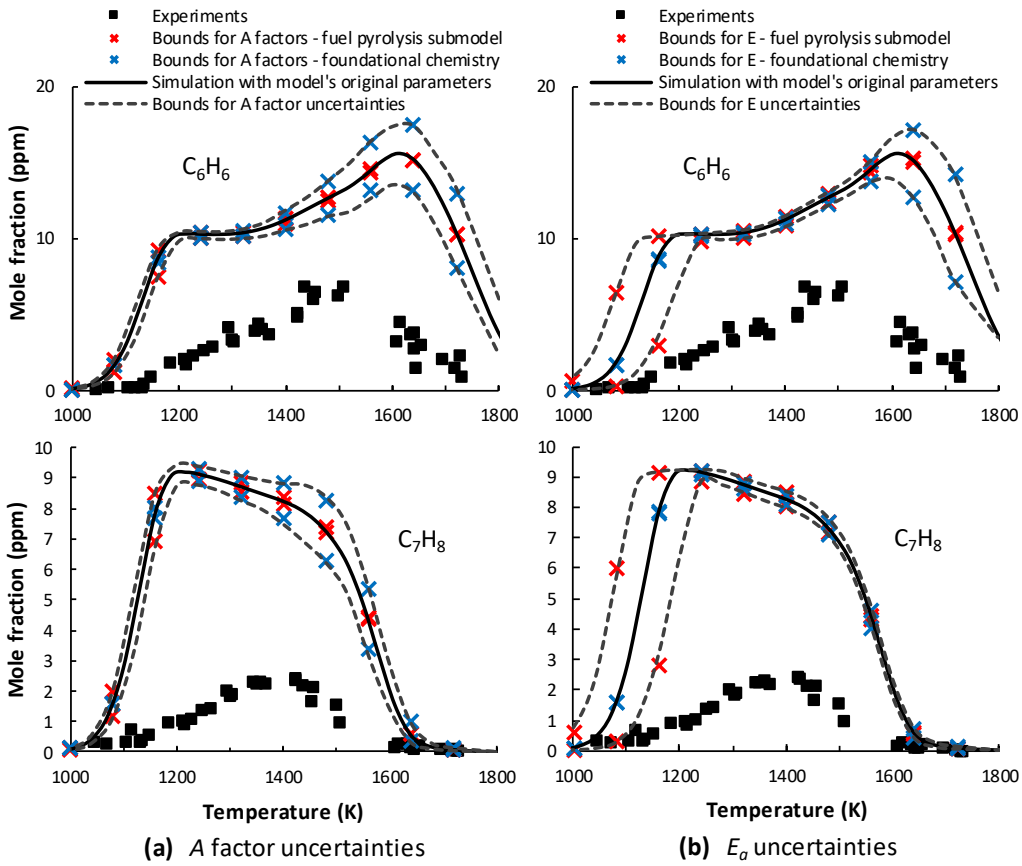

Figure 14: Monte Carlo results of the sensitivities of benzene and toluene to (a) the *A* factor and (b) the activation energy E_a. Symbols are experimental data at 25 atm. Solid lines are nominal predictions, and dashed lines represent 95% confidence intervals from (a) the *A* factor sampling within a ±30% uniform distribution for each *A* factor and (b) E_a sampling with a Gaussian distribution using 5% as the 2σ. The colored symbols represent bounds when the rate parameters of either only the fuel pyrolysis submodel (red) or only the foundational chemistry submodel (blue) are varied.

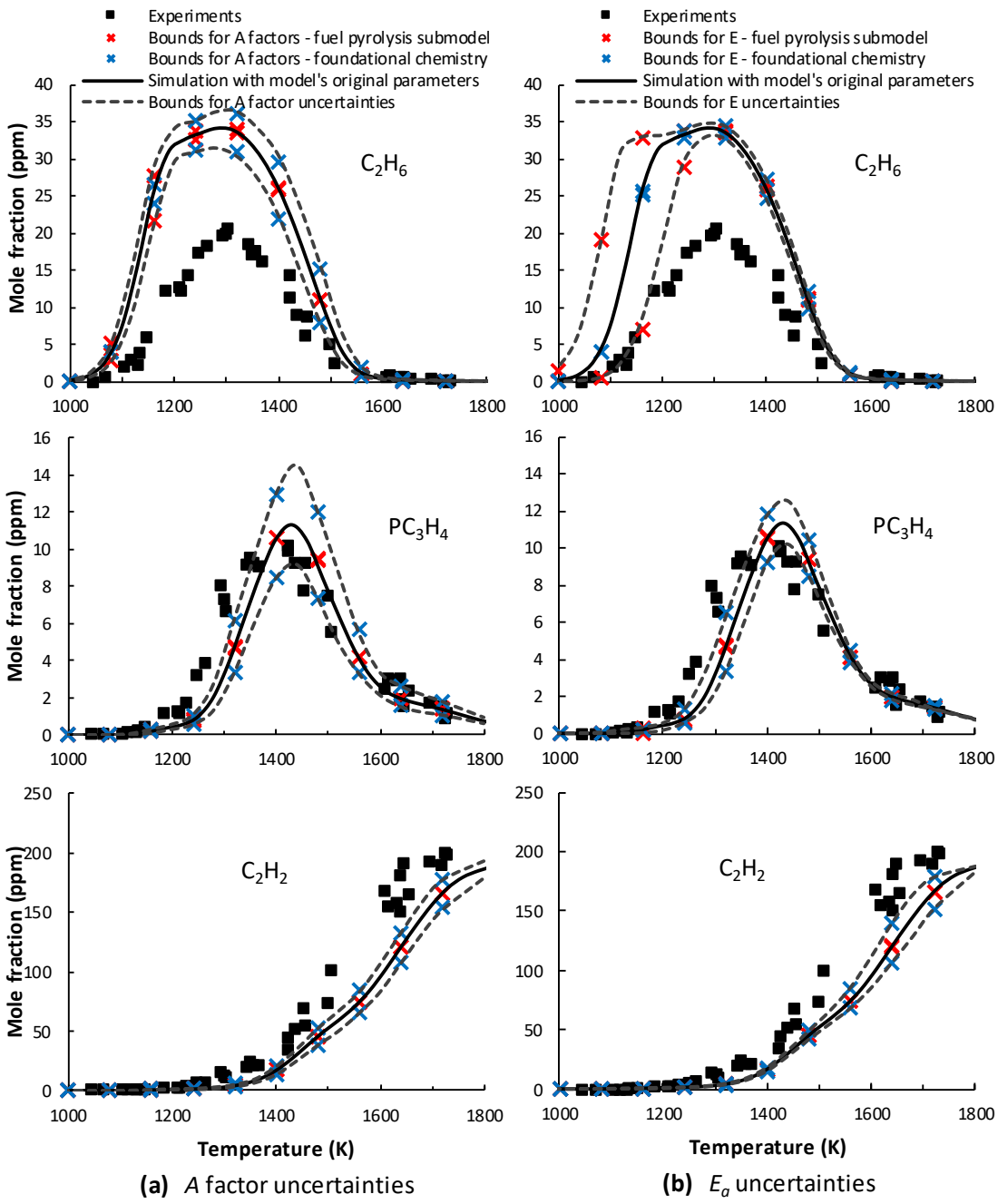

Figure 15: Monte Carlo results of the sensitivities of C_2H_6, pC_3H_4, and C_2H_2 to (a) the *A* factor and (b) the activation energy E_a. Symbols are experimental data at 25 atm. Solid lines are nominal predictions, and dashed lines represent 95% confidence intervals from (a) the *A* factor sampling within a ±30% uniform distribution for each *A* factor and (b) E_a sampling with a Gaussian distribution using 5% as the 2σ. The colored symbols represent bounds when the rate parameters

of either only the fuel pyrolysis submodel (red) or only the foundational chemistry submodel (blue) are varied.

As we can see from the Monte Carlo simulation result of other species in Figures 13-15, the pattern of the different effect of A and E_a in different temperature regions is further supported. The cause of the low sensitivity to E_a in the high temperature region may be due to this region being dominated by reactions with very low activation energy (typically lower than 20000 cal/mole), and the 5% uncertainty does not translate to significant increase in the $\exp(-\frac{E_a}{RT})$ value, because a 5% increase of E_a is equivalent to multiplying the original rate constant by $\exp(-\frac{0.05*E_a}{RT})$, which is close to 1 when the E_a is very small. On the low temperature side, the activation energy for the main reaction R1 is extremely large (87697 cal/mole).

The Monte Carlo analysis also shows that even the uncertainty band of the predictions of two aromatics C_6H_6 and C_7H_8 is still far off from the experiments, of which the profile shapes are very different between model and experiments. Note that in the HyChem model the R1-R2 reaction coefficients for the formation of these species are determined by the flow reactor data and the elemental balance of in these reactions. Therefore, there is a strong disagreement between our experiments and the Stanford flow reactor experiments in the formation of C_6H_6 and C_7H_8. The flow reactor also has a much larger time scale and a lower temperature of reactions than our shock tube data. This may have contributed to the discrepancies. C_6H_6 and C_7H_8 contributes an important amount of carbon to the carbon total. The model predicts that most of the C_6H_6 and C_7H_8 are directly formed through the fuel pyrolysis reactions rather fast, which made the carbon total of the model prediction reach its peak fast. However, our carbon total plot shows a gradually increased decomposition of Jet A up till 1700 K. We know that Jet A is a multicomponent fuel with a large

portion of cycloparaffins, iso-paraffins, and aromatic compounds that have different decomposition rates and can still form a small amount of other intermediate species not included in the model. Considering these factors, then perhaps, the species in Figure 13 and Figure 14 especially the aromatics should indeed be formed slower (this indicates a slower rise in the species-temperature plot). Note that although we do have a small amount of fuel loss in the test gas of our experiments (meaning some fuel components are preferentially reduced in the composition of the test gas) that may cause certain discrepancies with the true behavior of Jet A, but it is almost impossible to explain the so different shape of benzene and toluene profiles, as well as the carbon total profiles observed between our experiment and the HyChem model. From Figure 15, however, we also see that the species C_2H_6, pC_3H_4, and C_2H_2 that are produced through the foundational chemistry do have decent predictions, with their uncertainty bounds covering the experimental data or being close to it.

We can further study the detailed reasons about the discrepancies between model and experiments through a Spearman's rank correlation coefficient analysis using the Monte Carlo data. The Spearman's rank correlation coefficient curve between each species and individual reactions with respect to temperature can be obtained, as shown in Figure 16. The reactions with highest peak Spearman's rank correlation coefficients are selected (excluding ones that are only significant in regions where the studied species is not formed).

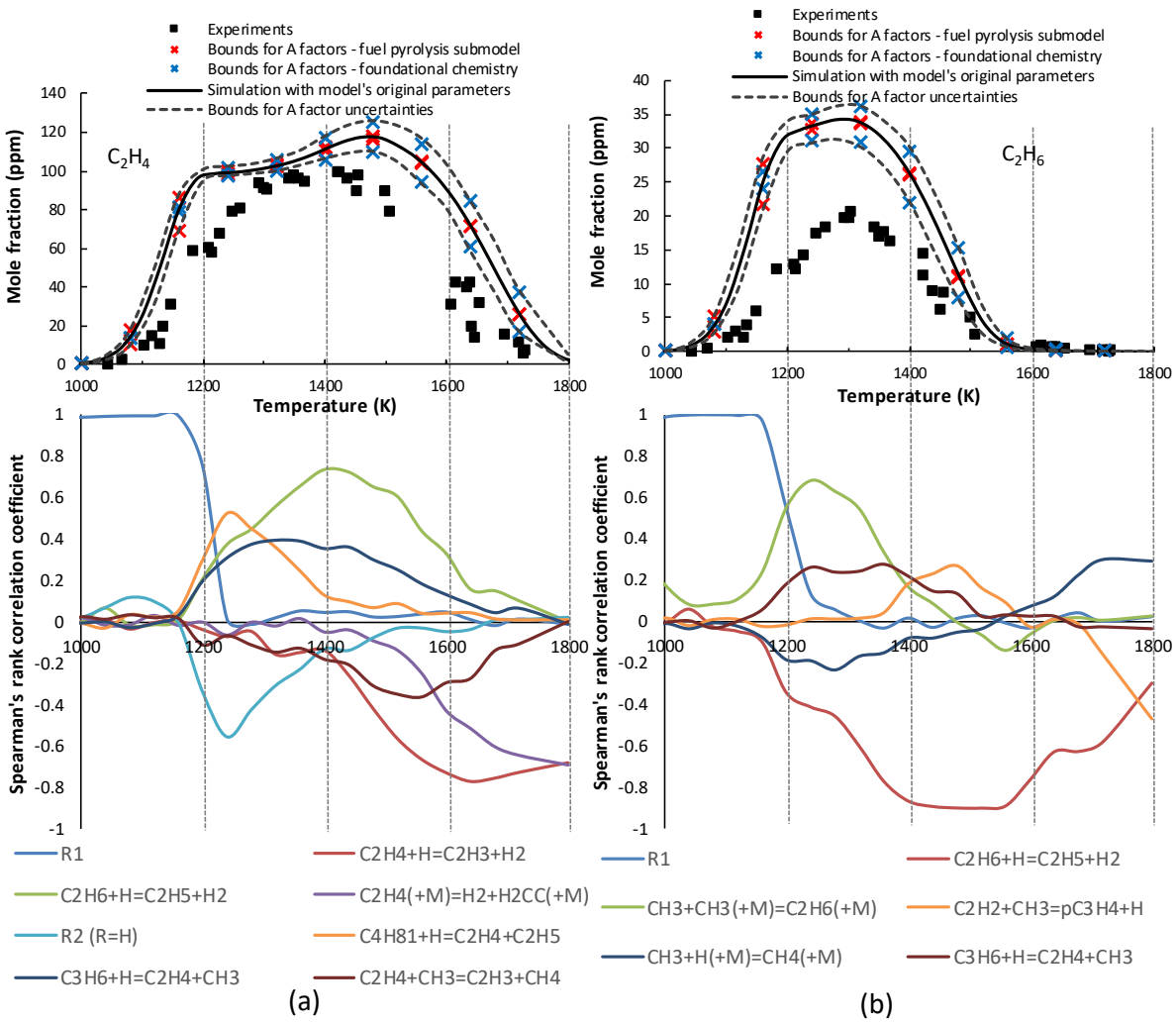

Figure 16: Spearman's rank correlation coefficients (bottom two subplots) between important reactions and certain species in the Jet A model acquired by the full model Monte Carlo simulation data with *A* factor perturbation at 25 atm 52.3 ppm fuel/Ar. The coefficients are plotted with respect to temperature. They are compared to the experiments in the HPST and simulations (top two subplots) with the uncertainty band from the *A* factor Monte Carlo simulation. (a) C_2H_4 and (b) C_2H_6. Reactions are selected based on the peak of the absolute value of the Spearman's rank correlation coefficients within the temperature region where the species has significant existence. Note that the same reactions are colored differently in (a) and (b).

From the Figure 16 (a) C_2H_4 and Figure 16 (b) C_2H_6, we can find relations between C_2H_4 and C_2H_6 formation. The major path towards C_2H_6 is through recombination of methyl radicals

$$CH_3 + CH_3 (+M) = C_2H_6 (+M) \qquad (R5)$$

In Jet A pyrolysis, C_2H_6 is formed in large amounts primarily due to the abundancy of CH_3 that is directly formed through the lumped fuel pyrolysis reaction R1. In R1, one mole of Jet A will directly form 1.5 mole of CH_3 (see Appendix G for the model details), which is large. Therefore, the formation of C_2H_6 is both sensitive to R1 and R5 at low to mid temperatures. As the temperature rises to 1500 K, the C_2H_6 mole fraction shows almost no sensitivity to the *A* factors of R1 and R5 and has very low values. At the same time, both C_2H_4 and C_2H_6 show strong sensitivity to the H-abstraction reaction of C_2H_6:

$$C_2H_6 + H = C_2H_5 + H_2 \qquad (R6)$$

This reaction will be followed by the rapid scission of C-H bond in C_2H_5 radical to form C_2H_4, and is largely responsible for the "secondary bump" of C_2H_4 at 1500 K in the simulation. Therefore, it can be inferred that C_2H_6 is immediately consumed after its formation from R5 (although it's not sensitive to it anymore, because it proceeds very fast) and eventually converted to C_2H_4 at this temperature. In this respect, C_2H_6 serves as an important intermediate for additional C_2H_4 formation at around 1500 K, according to the model. Therefore, C_2H_4 is basically dependent on the amount of CH_3 at that temperature. The secondary bump of C_2H_4 is not observed in the experiments. C_2H_6 is overpredicted by the model. Based on these facts, reducing the branch ratio (the stoichiometric coefficient) of CH_3 (thus its formation) in R1 can possibly reduce the production of C_2H_6 through R5 at high temperature and remove this bump of

C_2H_4. Although C_2H_4 is not sensitive to the A factor (reaction rate) of R1 anymore at high temperature where the foundational chemistry takes place, we believe C_2H_4 is still sensitive to the stoichiometric coefficient (yield) of CH_3 in R1. In JP10 pyrolysis, as will be shown later, the secondary bump in the C_2H_4 prediction does not exist, and this coincides with the low production of CH_3 and hence C_2H_6 from the fuel pyrolysis reaction of JP10.

The above is a great example of applying Spearman's rank correlation coefficient to analyze reactions. This example also indicates that unlike the uncertainties of the reaction rate parameters, those of the stoichiometric coefficients of the fuel pyrolysis submodel can affect the C_2H_4 formation in the high temperature region. Two other species C_3H_6 and C_6H_6 are also plotted with Spearman's rank correlation coefficient. The figure is attached in Appendix C.

Nevertheless, further investigation into the foundational chemistry is needed to improve the predictions in the high temperature region, as agreed by the other parties in this collaboration.

It should be noted that under oxidative conditions, the oxidation chemistry is coupled with pyrolysis chemistry above 1400 K and as such the oxidation chemistry can impact the pyrolysis product distribution in a major way. The level of difference observed in the model pyrolysis predictions above this temperature does not necessarily translate to a significant difference in the predicted combustion responses, e.g. ignition delay and flame speed. An analysis of this aspect of the model has been conducted in the HyChem paper [27]. This shock tube study, along with model analysis, serves the purpose of presenting experimental data under conditions (high pressure and highly dilute fuel/argon mixture) different than those from which the model was developed (lower pressure and high fuel concentration). To this end, the results of the sensitivity analysis motivates

future studies in real fuel combustion chemistry, especially in understanding the limitations of the model assumptions.

4.1.4 PREDICTIONS BY SURROGATE MODEL

The previous simulation using HyChem model shows evident discrepancies with the experiments. It is meaningful to examine a surrogate model performance and have a comparison. Currently, we have not found any available surrogate model for the Jet A we used in this study, which is POSF #10325. Previous studies by Dooley et al. [3] and Malewicki et al. [2] applied a surrogate formula called the 2nd Generation Surrogate that was developed for another Jet A (POSF#4658). A detailed kinetic model for this surrogate was developed by Malewicki et al. [2,71]. The main difference between the two Jet A fuels is that this Jet A (POSF#4658) has very little cycloalkanes (only 3.3%), while for the Jet A in our experiments (POSF#10325), that value is 31.7%, including both cycloalkanes and di-cycloalkanes. While the components are difference, Jet A fuels with different POSF numbers have generally similar physical properties. Furthermore, the previous HyChem studies [25,27] also suggest that these multicomponent jet fuels should have similar combustion chemistries. Therefore, we can use this surrogate model for our Jet A pyrolysis predictions. The surrogate fuel formula for the Jet A (POSF#4658) in the studies by Dooley et al. and Malewicki et al. is 40.41% n-dodecane, 29.48% iso-octane, 22.83% n-propylbenzene, and 7.28% 1,3,5-trimethylbenzene by mole. In our simulations, we applied the same mass balance adjustment with the approach used in the HyChem simulations, which adapts the fuel mole fraction to an equal mass to that of 52.3 ppm of $C_{11.37}H_{21.87}$ (the molecular formula of the real Jet A in our experiments).

Note that the H/C ratio of the surrogate fuel formula is 1.95 which is very close to 1.90 in the real Jet A fuel in our experiments. Thus, the carbon total of the input fuel with mass balance adjustment in the model is also consistent with our experiments. The input parameters for the simulation application is given in Table 1. The simulations at the conditions of the HPST 25 atm experiments are presented in Figure 17 and Figure 18, with comparison with the experimental data and HyChem predictions.

Table 1: Inputs for the surrogate fuel simulation to compare with the case of 52.3 ppm Jet A (POSF#10325) at 25 atm.

Fuel component	Mole fraction (ppm)
N-dodecane	24.2
Iso-octane	17.7
N-propylbenzene	13.7
1,3,5-trimethylbenzene	4.36
Pressure	25 atm
Reaction time	2.3 ms

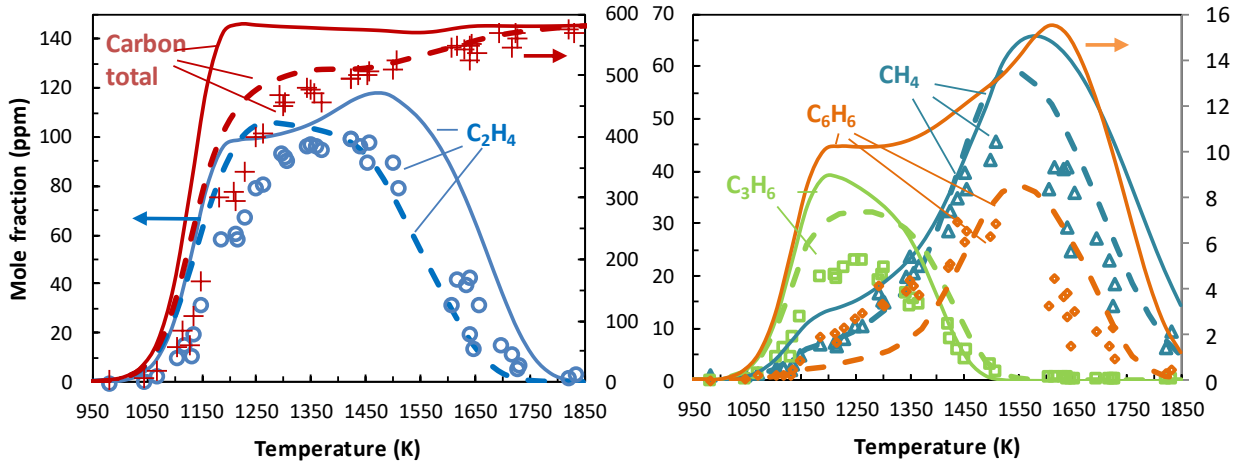

Figure 17: Comparisons of selected experimental (symbols), surrogate model predicted (dashed lines) and HyChem predicted (solid lines) species concentrations in the pyrolysis of 52.3 ppm Jet A in argon at 25 atm with 2.3 ms of reaction time. The carbon total profiles include the same set of identified major product species, without including surrogate fuel components.

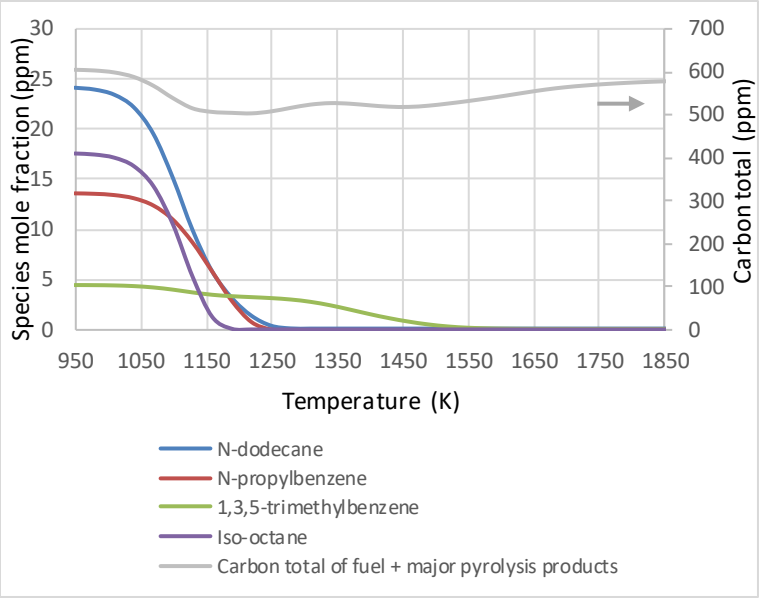

Figure 18: Decomposition of fuel surrogate component species by the surrogate model in the pyrolysis of 52.3 ppm Jet A in argon at 25 atm with 2.3 ms of reaction time. The grey line is the carbon total of all the surrogate component species and the same set of major product species in the experiments and in the HyChem model.

The simulation results in Figure 17 show a better C_2H_4 prediction by the surrogate model than by HyChem regarding the profile at high temperature and a significantly better carbon total profile that smoothly rises along temperature, which is close to what the experiments show. The predicted carbon total and C_2H_4 by the surrogate model still show decomposition of the fuel at a lower temperature than indicated by the experiments. Malewicki et al. [2] validated the surrogate model in the same HPST, but used Tsang's rate parameters for the temperature calibration with TFE, instead of the recent Matsugi parameters that we used in the HPST in this study. This can partially explain the discrepancy in fuel decomposition temperature between experiments and the surrogate model, as Tsang's rate parameters give a lower temperature than Matsugi's rate parameters do, as we will show in Chapter 6. CH_4, C_3H_6, and benzene predictions from the surrogate model are also closer to the experimental results than those from HyChem. Benzene in the surrogate model

predictions resembles the experimental data in that it is not formed rapidly in the lower temperature region below 1400 K. Figure 18 shows that the 4 surrogate components do not decompose at the same pace, unlike in HyChem model where each fuel molecule is considered to be the same single species. Most of 1,3,5-trimethlybenzene is not decomposed at 1250 K while the other 3 surrogate components have almost disappeared at this temperature. This pattern of a multicomponent fuel decomposition is one of the factors that may have caused the discrepancies we see between HyChem predictions and experiments.

Overall, the 2nd Generation surrogate model for Jet A predicted our experiments closer than the HyChem model, though it was developed for a different Jet A fuel. It would be of great value to further investigate the balance between prediction accuracy and computational efficiency, regarding the two types of models.

4.2 JET A PYROLYSIS WITH HIGH FUEL CONTENTS IN THE LPST

4.2.1 EXPERIMENTAL RESULTS

Three sets of experiments of high fuel content were conducted in the LPST for Jet A pyrolysis: 1) 2705 ppm Jet A in argon at 1 atm; 2) 6356 ppm Jet A in argon at 12 atm; 3) 6356 ppm Jet A in argon at 1 atm. The nominal reaction time was 2.1 ms. The difference in the fuel mole fraction estimated from CO_2 conversion experiments compared to that from fuel/Ar mixture preparation is

4 % lower for the 2705 ppm mixture and 1% lower for the 6356 ppm mixture. Due to some abnormal and irregular “peaks” from the GS-Gaspro column likely caused by the concentrated Jet A mixture, we were not able to detect the aromatics. The irregular peaks were also observed in studying dilute Jet A mixtures but to a much lesser extent. In future, a better choice of GC columns or pre-dilution of the sample gas may overcome this problem in the concentrated fuel experiments. The speciation results from the LPST experiments with high mole fraction and low pressure, 1 or 12 atm, are plotted together with the results from the HPST dilute mixture/25 atm experiments in Figure 19, with yield per mole of fuel as the measure of species production. Some species profiles show great degree of similarity among all four sets of experiments, regardless of the significant difference in pressure and concentration. The species quantity is presented as yield in these plots. By yield, we mean the ratio of the mole fraction of the species over the initial fuel mole fraction of the test gas.

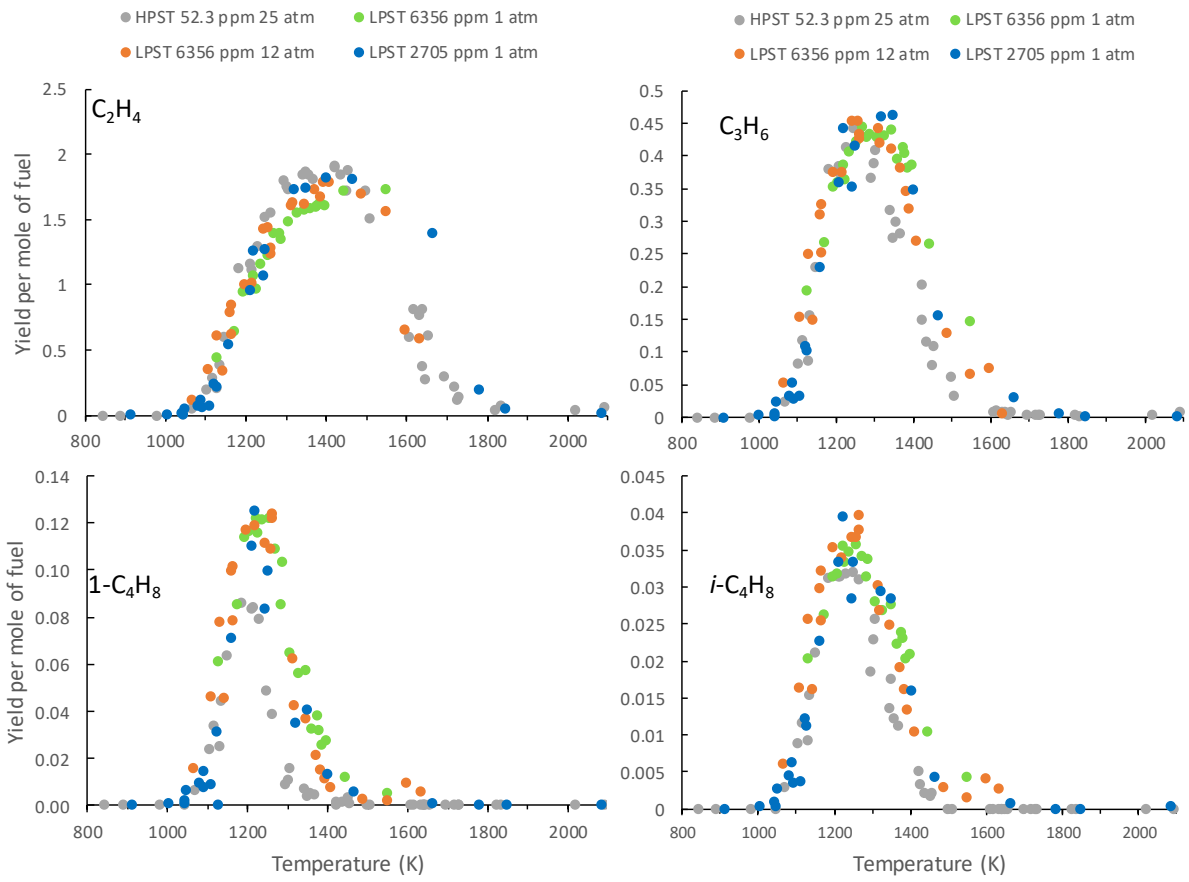

Figure 19: Formation of the alkene species C_2H_4, C_3H_6, 1-C_4H_8, i-C_4H_8, from 4 sets of pyrolysis experiments: 52.3 ppm Jet A in argon at 25 atm with 2.3 ms of reaction time in the HPST (gray); 6356 ppm Jet A in argon at 1 atm with 2.1 ms of reaction time (green) in the LPST; 6356 ppm Jet A in argon at 12 atm with 2.1 ms of reaction time (orange) in the LPST; 2705 ppm Jet A in argon at 1 atm with 2.1 ms of reaction time (blue) in the LPST.

Figure 19 shows that the formation of all the major alkene products is overall insensitive to pressure and concentration, except 1-C_4H_8, which has an evidently lower yield in the HPST dilute experiments while similar yields in the three LPST concentrated experiments.

If the chemistry of the formation of a species is not concentration dependent and not pressure dependent, there will be, nevertheless, small differences among experiments with different mole

fraction of fuel because a higher concentration of fuel will have a larger effect on the temperature due to both endothermic and exothermic reactions. For pyrolysis experiments, the overall thermal effect of the reactions is endothermic, which will reduce the temperature gradually during the reaction. Therefore, the C_2H_4 profile from a more high-fuel-content mixture during its increasing stage should show a right bending or shift, indicating a slower increase of formation with temperature due to more cooling from the endothermic reactions. This effect is observable in Figure 19, though it is visually very small. There may also exist a small bias in the temperature characterization for the two shock tubes: the temperature of the LPST is underestimated or that of the HPST is overestimated, as will be discussed later in the thesis. Either way, if we add this factor into account, then the cooling effect on C_2H_4 profile at <1400 K could be even more evident.

Overall, the minimal dependency on pressure or concentration besides the endothermic effect as we see in Figure 19 indicates that the simplification of fuel pyrolysis reactions by the HyChem model and the choice of the "directly" formed intermediate species which are primarily alkene and aromatics, is a reasonable modeling approach supported by experimental results.

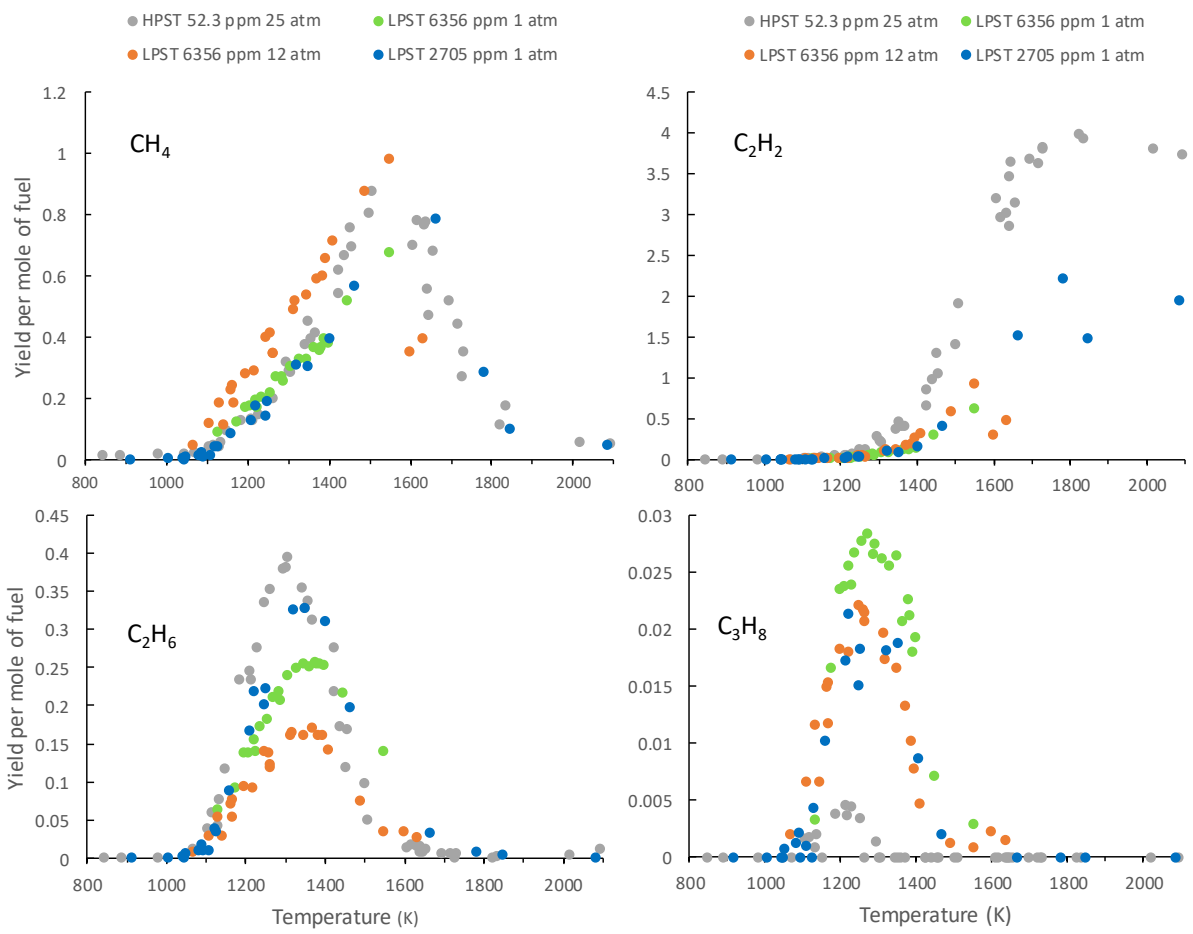

Figure 20: Formation of the small species CH_4, C_2H_2, C_2H_6, C_3H_8, from 4 sets of pyrolysis experiments: 52.3 ppm Jet A in argon at 25 atm with 2.3 ms of reaction time in the HPST (gray); 6356 ppm Jet A in argon at 1 atm with 2.1 ms of reaction time (green) in the LPST; 6356 ppm Jet A in argon at 12 atm with 2.1 ms of reaction time (orange) in the LPST; 2705 ppm Jet A in argon at 1 atm with 2.1 ms of reaction time (blue) in the LPST.

Figure 20 shows the profiles of some other small species whose formations are not solely dominated by the initial fuel decomposition β-scission reactions. The pressure or concentration dependencies of these species become very evident.

Some of CH_4 can be formed directly from the fuel pyrolysis, but more of CH_4 will be formed from other small products such as C_2H_4 through foundational chemistry. It seems that either high pressure or high concentration favors its production below 1500 K.

For the C_2H_2 profile, the HPST formation is shown to be much higher than the high-fuel-content/lower pressure experiments. The C_2H_2 formation in LPST 6356 ppm 12 atm is also higher than the other two LPST 1 atm experiments. Therefore, we believe that for C_2H_2 formation, there should be a strong pressure dependence in a certain range within 1-25 atm. At higher temperature above 1500 K, although we didn't gather many data points in this region for the LPST, it is likely that lower concentration of fuel will favor its formation. Higher concentration of fuel may lead to more consumption of C_2H_2 and the formation of large PAH and sooty species.

Two saturated species, C_2H_6 and C_3H_8, heavily rely on recombination reactions which are supposed to be favored by high fuel concentration conditions. However, ethane clearly shows increased formation as the concentration (mole per unit volume) of the fuel decreases. While C_3H_8 has very small formation with a negligible effect on the whole process. It is interesting to see C_3H_8 has a different response to pressure and concentration than C_2H_6. Model analysis could help elucidate the concentration dependent pathways for C_2H_6 and C_3H_8 formation.

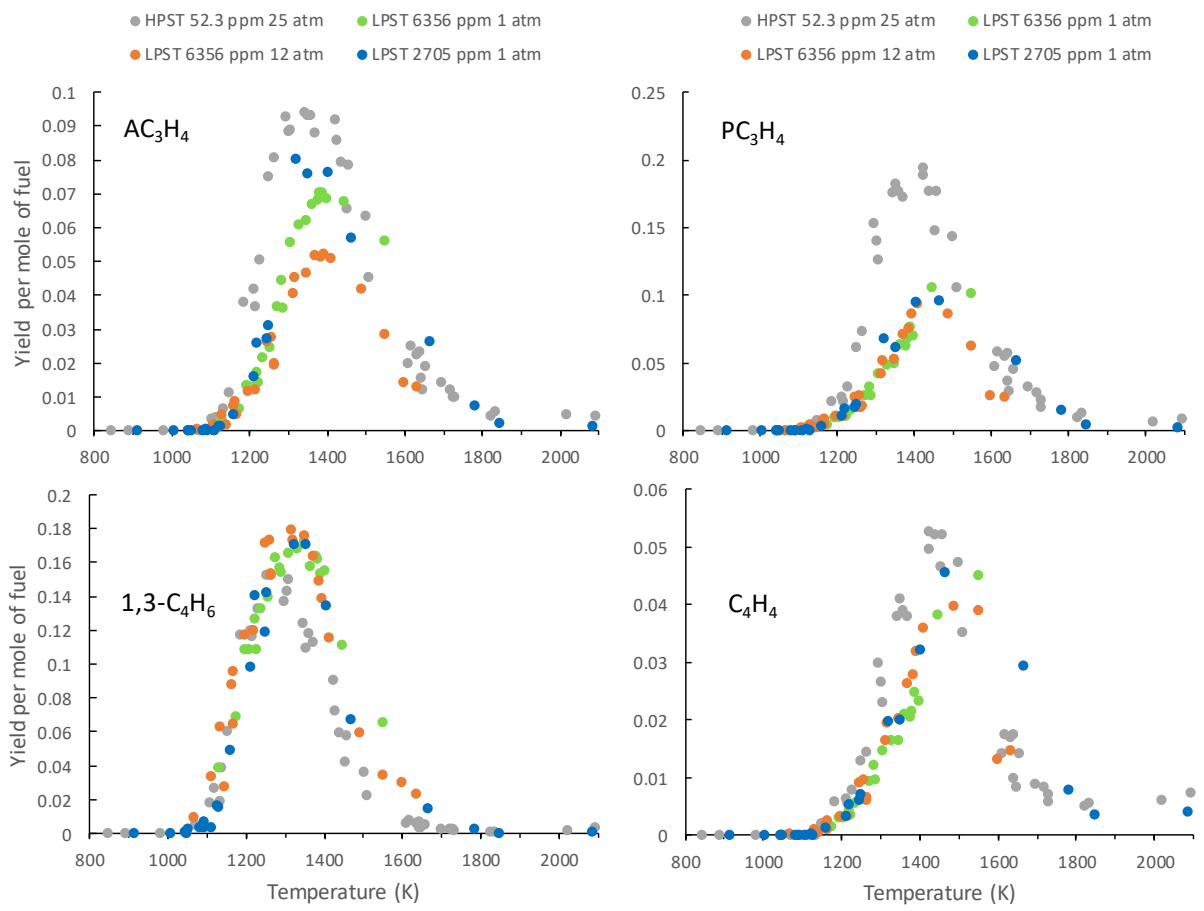

Figure 21: Formation of species aC_3H_4, pC_3H_4, 1,3-C_4H_6, C_4H_4, from 4 sets of pyrolysis experiments: 52.3 ppm Jet A in argon at 25 atm with 2.3 ms of reaction time in the HPST (gray); 6356 ppm Jet A in argon at 1 atm with 2.1 ms of reaction time (green) in the LPST; 6356 ppm Jet A in argon at 12 atm with 2.1 ms of reaction time (orange) in the LPST; 2705 ppm Jet A in argon at 1 atm with 2.1 ms of reaction time (blue) in the LPST.

Figure 21 shows the profiles of the highly unsaturated C3 and C4 species. 1,3-C_4H_6 shows very a small dependency on pressure and fuel concentration. The data suggest that aC_3H_4 peak formation is strongly dependent on the fuel volumetric concentration in the pressure range of 1 atm to 25 atm. For, pC_3H_4, the profile from the HPST experiment seems to deviate far from the rest, and the other three sets from LPST seem to overlap together. PC_3H_4 and aC_3H_4 formation are also heavily

correlated. These observations indicate a strong possibility of the presence of both a pressure and a concentration effect on the formation of aC_3H_4 and pC_3H_4.

4.2.2 SIMULATIONS OF JET A PYROLYSIS AT LOW PRESSURE AND HIGH FUEL CONTENT

Constant pressure simulations at the conditions of the 3 sets of LPST experiments were conducted. Figure 22 and Figure 23 compare simulation results to the experimental results for the important species for the 3 sets of LPST high-fuel-content experiments and the 25 atm dilute one in the HPST.

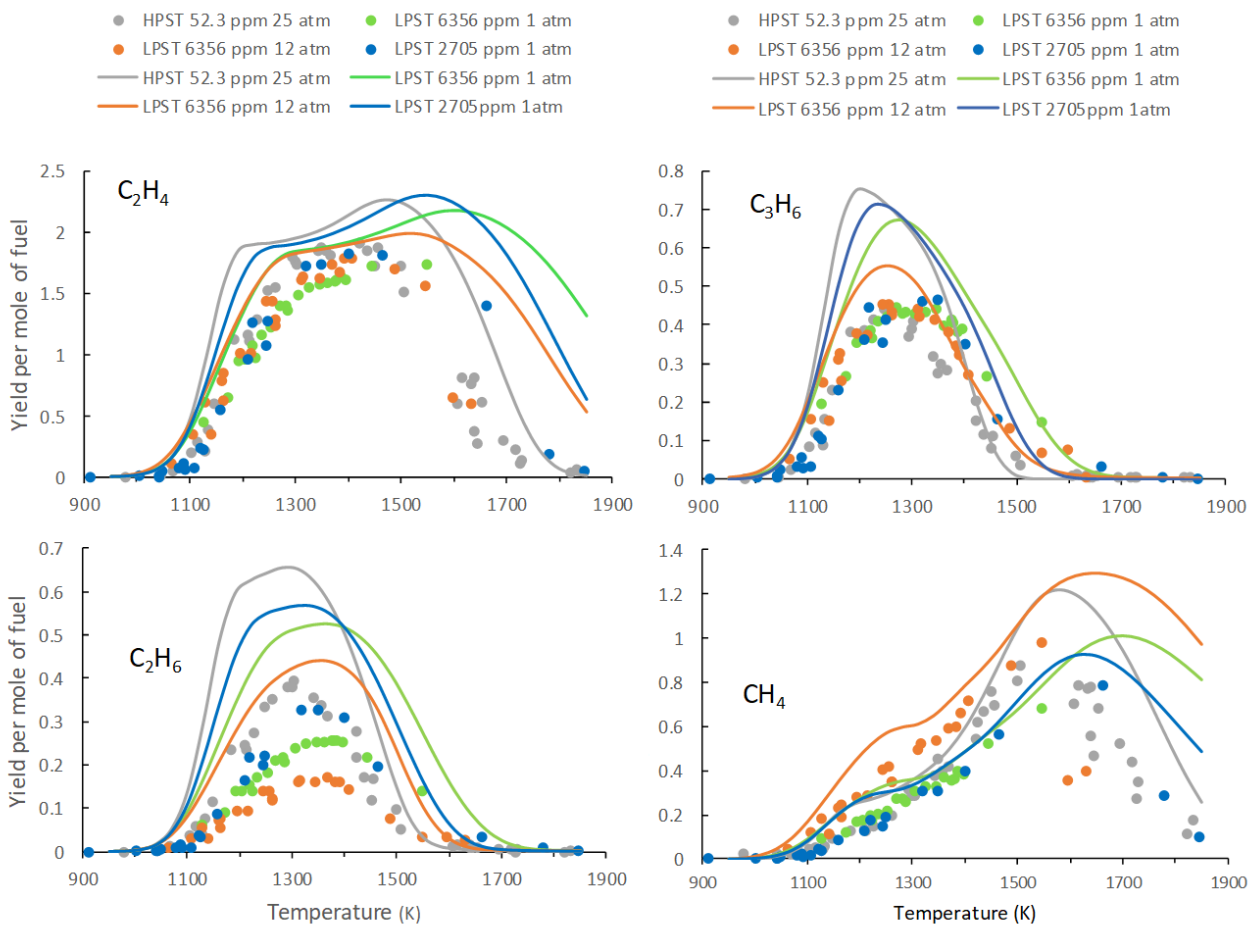

Figure 22: Comparison between the model (line) and the experiments (dot) on the formation of C_2H_4, C_3H_6, C_2H_6, CH_4, from 4 sets of conditions: 52.3 ppm Jet A in argon at 25 atm with 2.3 ms of reaction time in the HPST (gray); 6356 ppm Jet A in argon at 1 atm with 2.1 ms of reaction time (green) in the LPST; 6356 ppm Jet A in argon at 12 atm with 2.1 ms of reaction time (orange) in the LPST; 2705 ppm Jet A in argon at 1 atm with 2.1 ms of reaction time (blue) in the LPST.

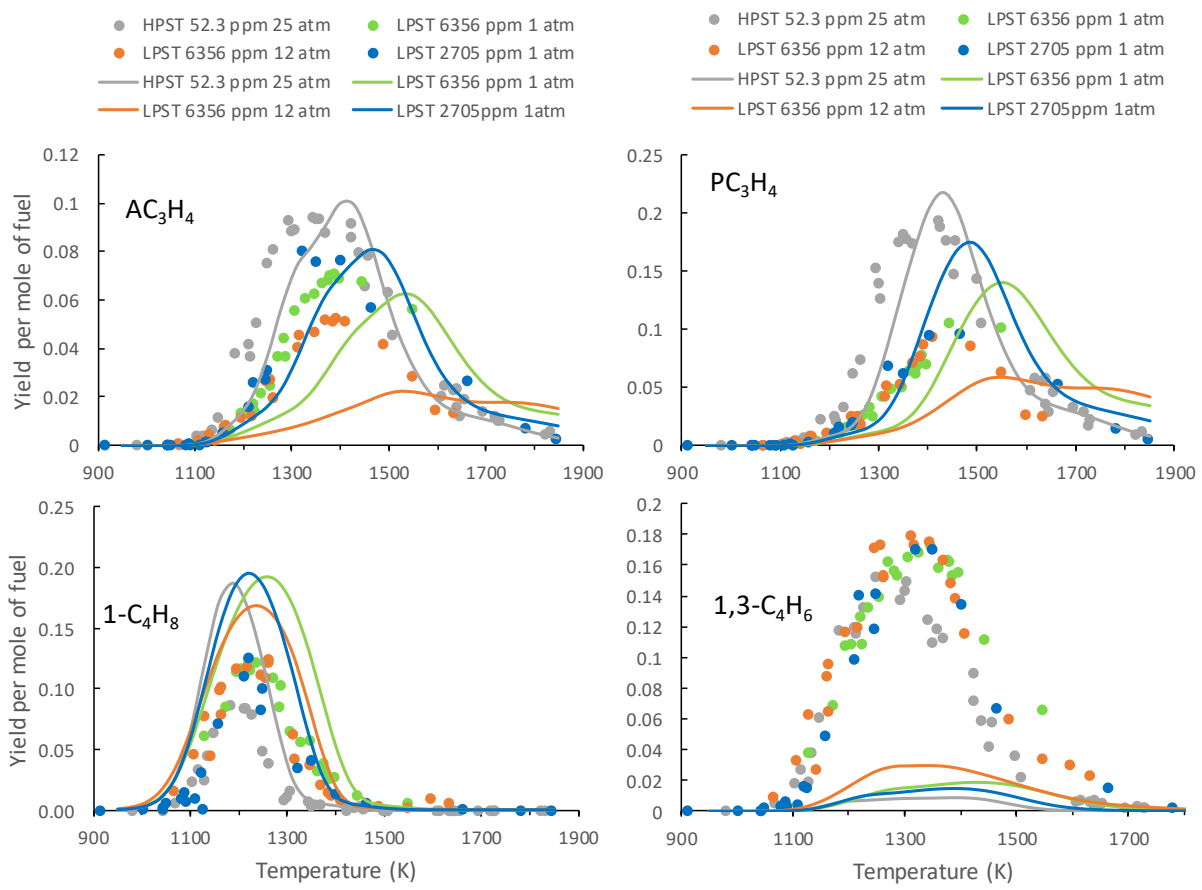

Figure 23: Comparison between the model (line) and the experiments (dot) on the formation of aC_3H_4, pC_3H_4, 1-C_4H_8, 1,3-C_4H_6, from 4 sets of conditions: 52.3 ppm Jet A in argon at 25 atm with 2.3 ms of reaction time in the HPST (gray); 6356 ppm Jet A in argon at 1 atm with 2.1 ms of reaction time (green) in the LPST; 6356 ppm Jet A in argon at 12 atm with 2.1 ms of reaction time (orange) in the LPST; 2705 ppm Jet A in argon at 1 atm with 2.1 ms of reaction time (blue) in the LPST.

A general trend can be observed from the plot. The alkenes C_2H_4, C_3H_6, and 1-C_4H_8, in addition to C_2H_6 are overpredicted by the model as was seen in the comparisons between model and experiments in the HPST. The dependency of C_2H_6 and aC_3H_4 on fuel concentration is predicted by the model, although with an exaggeration of that dependency in the aC_3H_4 predictions. It is

interesting to see that the peak of the C_3H_6 profile also shows such a fuel concentration dependency in the model predictions, while apparently not in the experiments.

The best predicted species are C_2H_4 and CH_4 below 1500 K. The prediction for CH_4 is good, not only because the predicted curves of CH_4 lie close to the corresponding experimental data below 1500 K, but also because the small relative differences in CH_4 profiles observed in the comparison among the four experiments is well predicted: the two 1 atm/high-fuel-content shocks in LPST almost overlap with each other at below 1500 K; the HPST 52.3 ppm/25 atm shock profile also overlaps with the two 1 atm shock profiles below ~ 1350 K, but rise higher after that temperature and reaches the same height with the 6356 ppm/12 atm shock profile, which is always higher than the profiles from the two 1 atm shocks below 1500 K. As shown in the Monte Carlo analysis in Section 4.1.3, this region is generally insensitive to both the A factors and activation energy E_a of the whole model. It is a similar case for the peak (plateau in simulation) of C_2H_4 that is well predicted for all experimental conditions.

The model nevertheless predicted a higher temperature for the onset of the decomposition of the alkene products and the rise of the aC_3H_4 and pC_3H_4 compared with experiments. This consistent pattern, as we also see in the HPST results, indicates that the foundational chemistry submodel, USC Mech II, overall predicts a higher temperature for the reactions compared with experiments. If we look globally at the species profiles in the above plots, it is obvious that the full species profiles of alkenes from the experiments have a narrower band of temperature than the predicted profiles. This mis-match could not be simply due to a possible bias in temperature measurement from our shock tubes. Instead, since the fuel pyrolysis submodel and the foundational chemistry submodel were developed separately, it is likely that there is an inconsistency in the temperature

measurements between the experiments that were used to fit the HyChem fuel pyrolysis model and the ones that were used to build the USC Mech II model. This, in addition to possible fundamental problems in the chemical kinetic model could be leading to the mismatch.

From the model/experiment comparisons in Figure 22 and Figure 23, it can be seen that the foundational chemistry does predict an earlier (lower temperature) decomposition of some C2-C4 species in the HPST 52.3 ppm/25 atm shocks than in the simulations from the LPST, which is especially evident in the 1-C_4H_8 profile. There are some interesting patterns predicted in the high temperature region that should be observable in experiments, but since we do not have many data points in the high temperature region in the LPST experiments at this point, comparison of predictions with experiments will be left to future work.

Another pattern worth noticing is that the model accounts for, as seen in Figure 19, the cooling effect of the endothermic reactions during the decomposition of the fuel, which results in a faster rise of the C_2H_4 profile in a test gas with lower fuel ppm, as shown in Figure 22. Our experimental data shows this effect to be a little less than predicted. This difference may be partially due to the incomplete decomposition of the fuel to the small intermediate species when C_2H_4 rises to its peak, as opposed to the fast completion of decomposition assumed in the HyChem model, as we see in the carbon total profile in Figure 9.

Overall, the model works satisfyingly in predicting the overall trends of the small product species, although with a large room for improvement.

5 JP10 PYROLYSIS EXPERIMENT AND SIMULATION RESULTS

5.1 JP10 EXPERIMENTAL RESULTS

Dilute pyrolysis experiments of 72 ppm JP10 in argon were conducted at 25 atm and 90 atm in the HPST. Another set of experiments of 75 ppm JP10 in argon at 12 atm was conducted in the LPST with the main purpose to compare the two shock tubes. The experimental results show that the main products of JP10 pyrolysis are CH_4, C_2H_4, C_2H_2, C_2H_6, C_3H_6, pC_3H_4 (propyne), aC_3H_4 (allene), 1-C_4H_8, *i*-C_4H_8, 1,3-C_4H_6, C_4H_2 (diacetylene), C_4H_4 (vinylacetylene), cyclopentene, cyclopentadiene, 1,3,5-hexatriyne, benzene, and toluene. There are also many minor peaks observed in the chromatogram, including indene, naphthalene, etc. Cis-2-butene was not detected, in contrary to what other parties in this project found. The 25 atm and 90 atm shocks in the HPST show identical product mole fractions results as shown in Figure 24. Selected species are plotted together in Figure 25 for comparison.

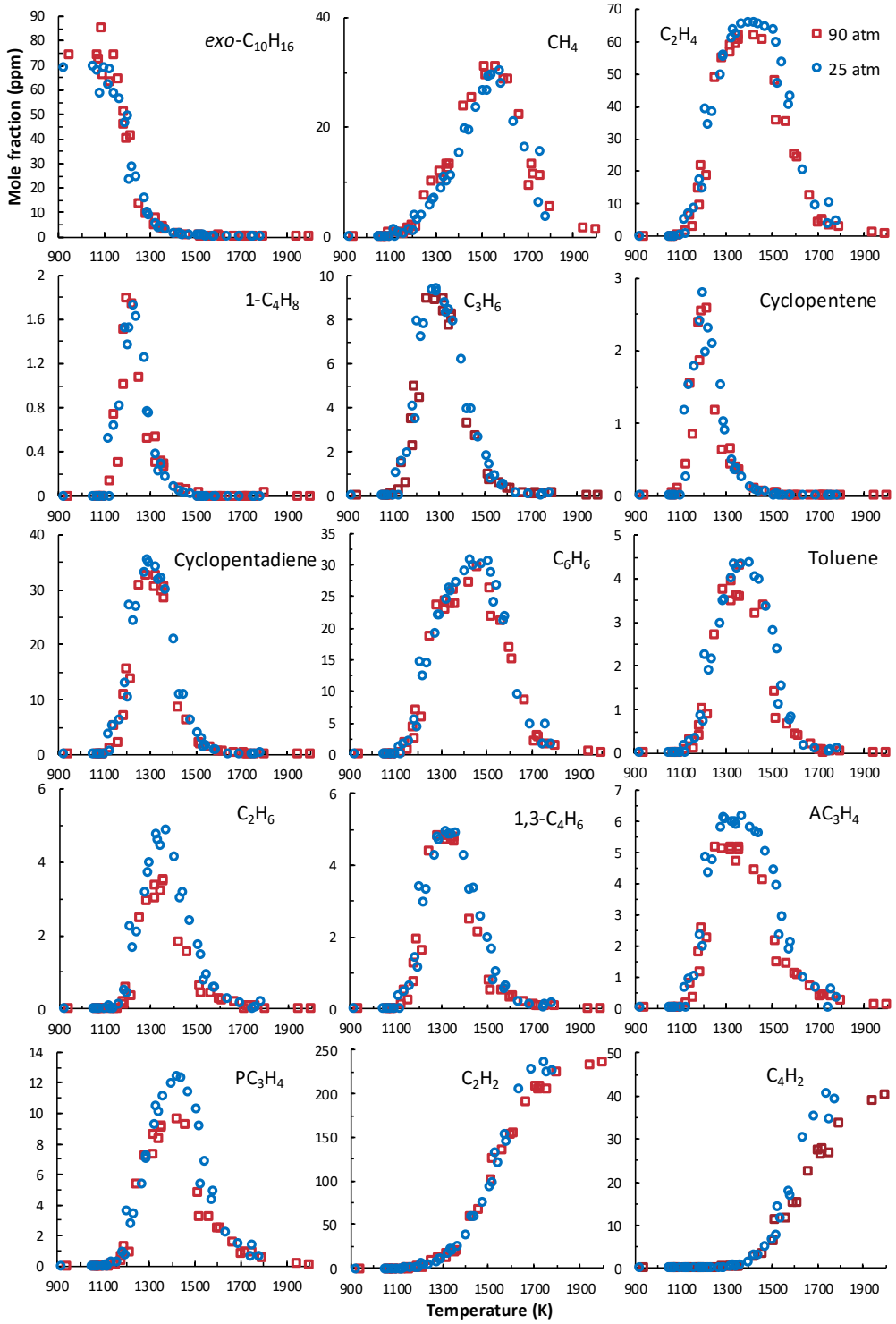

Figure 24: Species measured at 25 and 90 atm post shock pressures (P_5) and at 900 – 2000 K post shock temperatures (T_5). Initial fuel mole fraction of JP10 is 72 ppm in argon. The nominal reaction time is 2.3 ms.

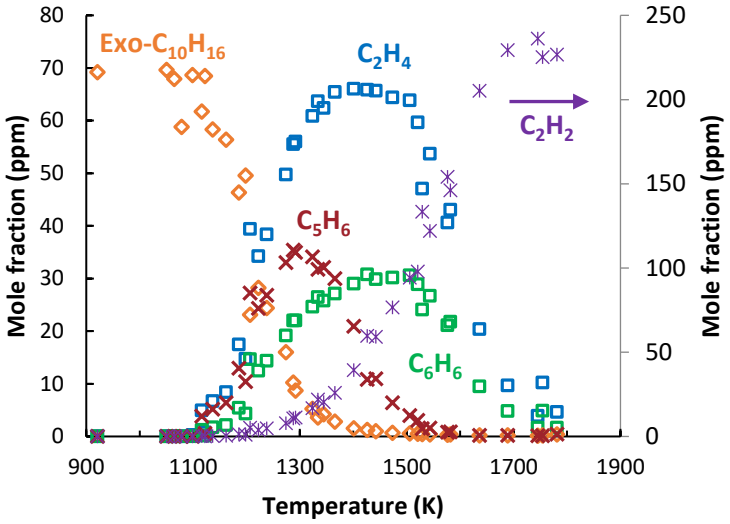

Figure 25: A comparison plot of the formation of the most significant species in JP10 pyrolysis: exo-$C_{10}H_{16}$, C_2H_4, C_5H_6, C_6H_6, and C_2H_2 in the 25 atm HPST experiments. The test mixture is 72 ppm JP10 in argon. Nominal reaction time is 2.3 ms.

If we look at the peak mole fraction of the products, JP10 produces evidently less C_2H_4, which forms around 18% of the fuel carbon at its peak, compared to Jet A, of which around 34% of its carbon is converted to C_2H_4 at its peak. A significant portion of JP10 is converted to cyclopentadiene, which forms ~25% of carbon at its peak, and benzene, which forms 26% of the total carbon at its peak, compared to much lower percentages, 2% and 7% respectively, from Jet A pyrolysis. This significance of cyclopentadiene formation, along with the appearance of cyclopentene formation from JP10, suggests reaction pathways that will keep one of the two 5-member rings unbroken in the pyrolysis of JP10. Previous studies have pointed out the importance of cyclopentene in JP10 pyrolysis. However, cyclopentene seems to quickly break down at low temperatures, making its profile a very narrow one with a peak at around 1200 K. Cyclopentadiene and benzene are relatively stable at mid and low temperatures. These two ring species make up a

large share of the products. The other major species observed in the pyrolysis of JP10, e.g. CH_4, C_2H_4, C_2H_6, C_3H_6, 1-C_4H_8, are formed significantly less compared to the case in Jet A pyrolysis in the mid and low temperature region which is not surprising since their initial compositions are very different. Iso-butene is almost unobservable in JP10 pyrolysis. The other highly unsaturated products, e.g. pC_3H_4, aC_3H_4, 1,3-butadiene, which are considered to be formed indirectly from the fuel molecule, still have an important amount of formation. Overall, JP10 pyrolysis favors slightly more the production of highly unsaturated species and ring species. At high temperature, C_4H_2 and C_2H_2 gradually take up majority of the pyrolysis products from JP10.

A summary of the contribution of species to the carbon balance is shown in Figure 26 below and the carbon total for 25 and 90 atm in Figure 27.

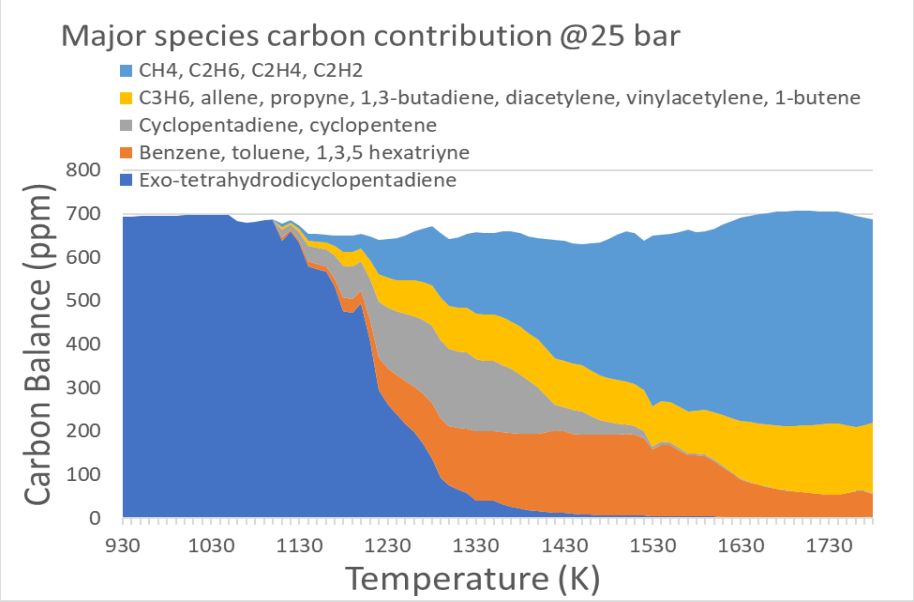

Figure 26: Carbon balance of species of different sizes along temperature in the pyrolysis of 72 ppm JP10 in argon at 25 atm in the HPST, with 2.3 ms reaction time.

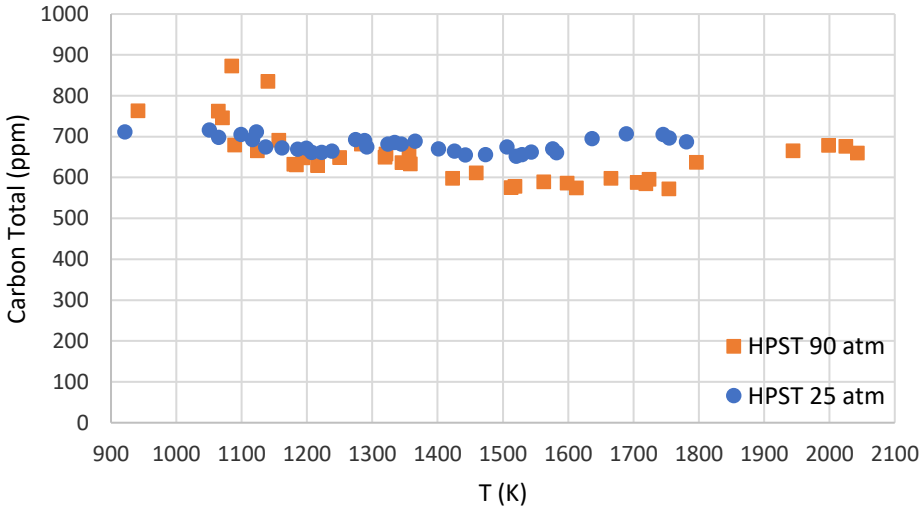

Figure 27: Comparison of carbon total between 25 atm and 90 atm shocks for 72 ppm JP10 pyrolysis in argon in the HPST with 2.3 ms reaction time.

From Figure 26, one can see that the majority of the detected pyrolysis products from JP10 are a limited set of simple small species that have a relatively well-known combustion chemistry. These species, along with the remaining fuel, can recover most of the carbon total from the original fuel. This result strongly supports the hypothesis that the HyChem model is based upon. It shows that for JP10, it is probably sufficient to include these species in the kinetic model without having to include larger intermediate species. In addition to this observation, the smooth decomposition curve of JP10 also suggests that the HyChem approach that is used for Jet A can also be applied here to JP10 which is approximately a single component fuel.

While the pressure dependence in these two set of experiments is negligible for most species, C_2H_6, aC_3H_4, pC_3H_4, and C_4H_2 show some pressure dependency. These species have higher yield at lower pressures at the same fuel mole fraction. The carbon total also shows a small pressure dependency

to the case in Jet A experiments, which may be due to high sooting at high pressures. The C_4H_2 profile as shown in Figure 24 displays evident pressure dependence, which is possibly due to its conversion to sooty matter at higher pressure and high temperature.

The data from the LPST JP10 pyrolysis at 12 atm with 75 ppm fuel is compared with the 25 atm data from the HPST with 72 ppm fuel in Figure 28. The results show that the LPST experiments can reproduce an important portion of the results in HPST.

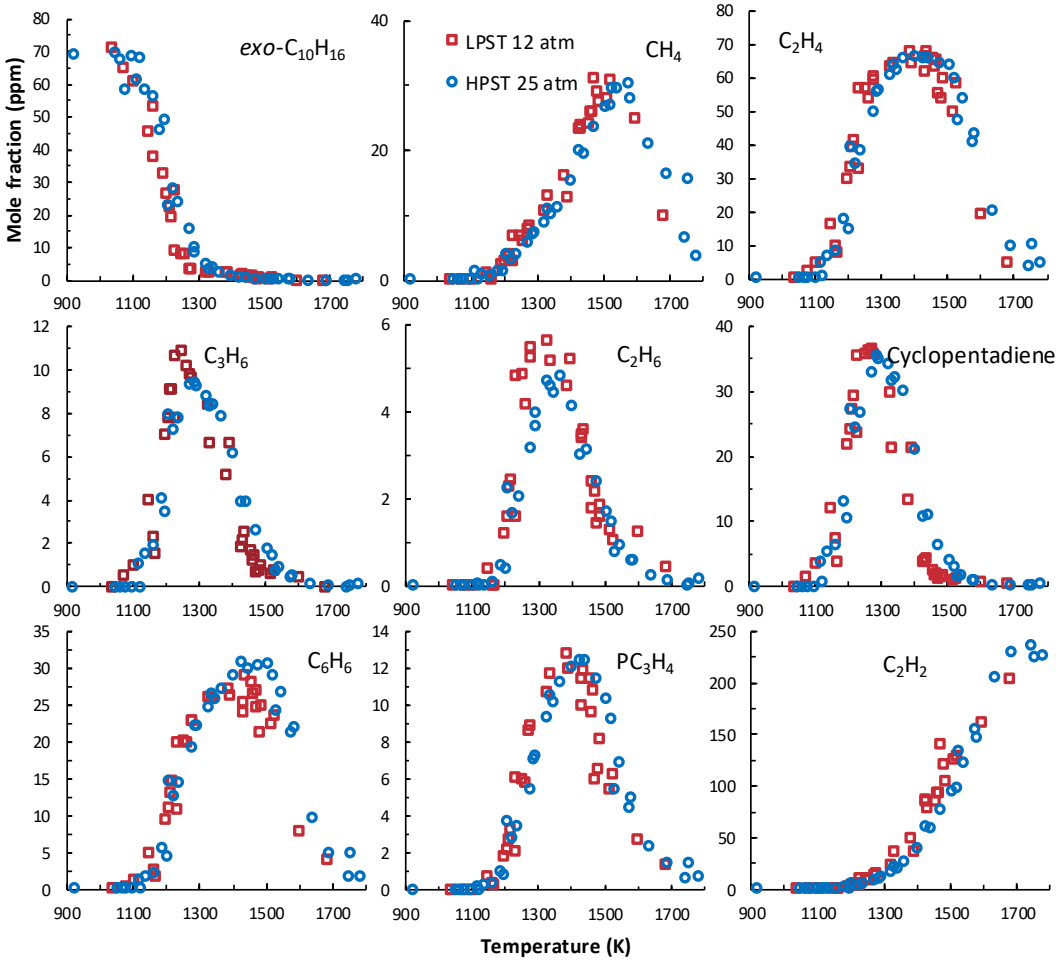

Figure 28: Comparison of the species measured from experiments at 75 ppm 12 atm in the LPST (red) and 72 ppm 25 atm in the HPST (blue) and at 900 – 2000 K post shock temperatures (T_5). The nominal reaction time is 2.1 ms for LPST (red) and 2.3 ms for HPST (blue).

The profiles of most species from the two shock tubes are identical except that there is a slight temperature shift, with the LPST having a ~30 K lower temperature than the HPST profile as evidenced by all the LPST points shown in red in Figure 28 being systematically shifted to the left, i.e. towards lower temperatures. This should be mostly due to the difference in temperature characterization between the two shock tubes. As mentioned in the Jet A profile comparison in the last chapter, as we will discuss this in detail later in the next chapter. The higher C_2H_6 peak in the

LPST 12 atm shocks again should be due to the reduced pressure, thus reduced concentration of CH_3, which forms C_2H_6 through bimolecular recombination.

It should be noted that the LPST has a very flat reflected shock pressure time profile, while the HPST has a much larger post-shock pressure increase. The implications of this will be further discussed in Chapter 6.

5.2 SIMULATION RESULTS OF JP10 PYROLYSIS

The constant pressure simulations of JP10 were conducted using the HyChem Model of JP10 pyrolysis and oxidation, with a fixed time of 2.3 ms. The results are compared with the experimental data at 25 atm, as shown in Figure 29 and Figure 30. The Monte Carlo analysis and pressure dependence analysis are also conducted. Most species match well with the simulations. The pressure dependence is minimal. For conciseness of interpretation, the results of the Monte Carlo analysis and pressure dependence analysis are shown in Appendix D.

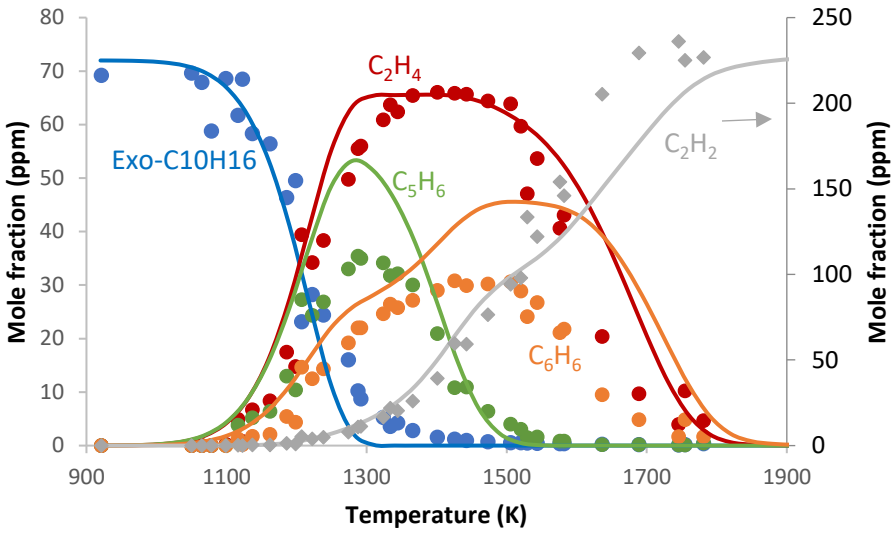

Figure 29: Comparison between experiments (symbols) and simulation (lines) regarding the formation of the most significant species in JP10 pyrolysis: exo-$C_{10}H_{16}$, C_2H_4, C_5H_6, C_6H_6, and C_2H_2 in the 25 atm HPST experiments. The test mixture is 72 ppm JP10 in argon. Nominal reaction time is 2.3 ms. The simulation and experimental plots for a species have the same color.

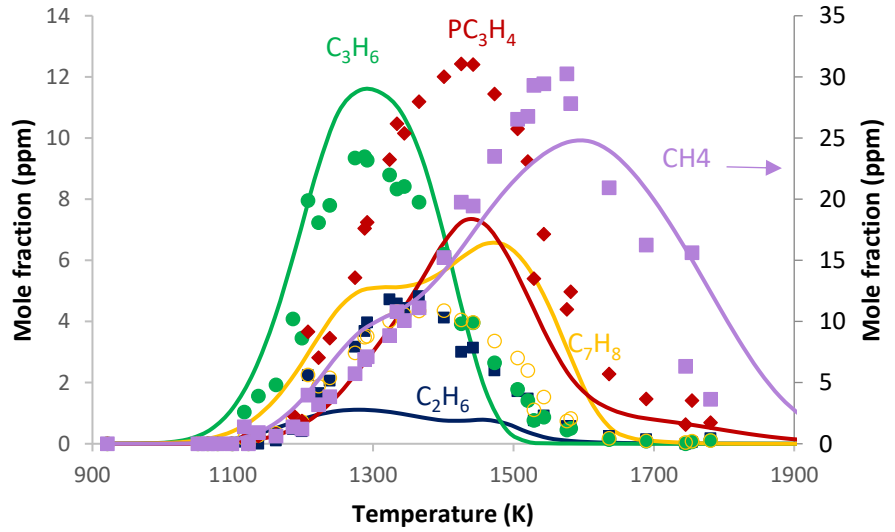

Figure 30: Comparison between experiments and simulation regarding the formation of some important products in JP10 pyrolysis: C_3H_6, pC_3H_4, C_2H_6, C_7H_8 and CH_4 in the 25 atm HPST experiments. The test mixture is 72 ppm JP10 in argon. Nominal reaction time is 2.3 ms.

The decomposition of JP10 is well predicted. The prediction of the C_2H_4 is very good in both its rising and dropping region, and almost perfect on its peak amount. The formation of the equally important species, benzene, is also very good, below 1400 K. Cyclopentadiene is overpredicted to an extent, and the predicted temperature profile is realistic, regarding the temperatures at which it rises or drops. Moreover, C_3H_6 and CH_4 are both very well predicted. Toluene is overpredicted to a small extent. The above 6 products are the stable hydrocarbons that can be directly formed from the fuel pyrolysis in the HyChem model, with C_2H_4, cyclopentadiene, and benzene being the most important. This shows that the fuel pyrolysis submodel of HyChem for JP10 matches our experimental results in the UIC shock tubes.

At the peak formation temperature of cyclopentadiene, around 1300 K, JP10 in the experiments has not completely disappeared while the model shows no JP10 left. The simulation predicts that cyclopentadiene mostly decompose into C_2H_2, C_3H_3, aC_3H_5, and CH_4. At around 1400 K, JP10 in our experiments has almost completely been consumed, and all the major species in Figure 29 show close agreement between experiments and model. At above 1400 K, certain species such as benzene and toluene start to show large disagreement with the model, while other species especially C_2H_4 still show decent agreement.

There are also some unexpected observations. C_2H_6, which was over overpredicted by a factor of about 50% in the Jet A shocks at 25 atm, is now significantly underpredicted by the HyChem model for JP10, that uses the same foundational chemistry submodel. The very low level of C_2H_6 production (around 4 ppm in peak area) in this case may contribute to the observed discrepancy. Still, both the model and experiment do give a good qualitative prediction that C_2H_6 is not very

important in JP10 pyrolysis. The low production of C_2H_6 from the model is made possible by the very low branching ratio of CH_3 from the main fuel pyrolysis reaction R3.

Overall, the HyChem model performs reasonably well for most species especially at or below 1400 K. This shows that the HyChem model can be successfully applied to this single component fuel with complex decomposition pathways.

6 TEMPERATURE CHARACTERIZATION

6.1 INTRODUCTION

Chemical kinetic models are developed and/or validated by experiments. In many cases, a full model is built upon experiments from different sources of experimental data. Disagreement among different models for the same reactions and species is very common even for the most basic foundational chemistry describing the reactions for C1-C4. A key issue is that the characterization of temperature of chemical kinetic experiments can be inconsistent among experiments causing a temperature displacement for species profiles with respect to the temperature predicted by different kinetic models, or when a model that is built upon experiments from one research group is then used to simulate experiments from another research group. Consequently, temperature consistency among the various experimental laboratories was a key concern in the HyChem project. It has been challenging to find out the reasons for disagreements in temperature with data from different laboratories and with the HyChem model in this large collaborative project. So far, we have only pointed out that the effect of reactions from a high fuel content initial reactant mixture will affect not only the initial T_5 after the reflected shock, but also the following temperature history of the reactants. A few other important contributions have been considered in order to evaluate and improve temperature characterizations. These contributions will all be discussed in this Chapter after a brief description of them that immediately follows.

First, the effect of the changing pressure time profile after formation of the reflected shock has been investigated. This is especially important because we use the GC for species measurements in our shock tubes at UIC to measure the end result of each shock (after the test gas cools down), while the Stanford shock tube laboratory applies time resolved laser diagnostics that has

information (though limited in species) from the starting of reaction to a certain time. The laser diagnostics measurement in Stanford shock tubes typically only measures the species before the cooling wave arrives and the reaction time is directly measured. However, there are still reactions going on during the cooling wave. In GC measurements, people typically use the 80% rule to get a nominal reaction time that is from an empirical evaluation to adapt to the changing pressure including the cooling wave. These may cause certain discrepancies between GC method and laser diagnostic methods. Another concern is that the HPST has a narrow bore of 1", and has an effective boundary layer that can cause considerable rise (~ 20 %) to the post-shock pressure profile. This issue has generally been addressed by chemical thermometer calibrations. The validity of this approach has previously been discussed by Tang et al. [73]. The authors also discussed an alternative approach, which is to use a changing pressure simulation derived from the real pressure trace of each experiment. In this work, we have further investigated the chemical thermometer approach and changing pressure simulation with more support from experimental data and simulations, as well as some more analysis similar to that done in the previous study by Tang et al.[73].

Secondly, the temperature uncertainties in our measurement have been investigated. There has been a trend in the chemical kinetic community to include more precise evaluation of the uncertainties of both species and temperature measurements. This will provide important information for model fitting as well as the interpretation of the results of model validation. We investigated many sources of uncertainties, such as the velocity measurement, uncertainties of temperature that comes from the uncertainty of species component that will affect the T_5 temperature.

Lastly, we will introduce a preliminary study on the shock wave behaviors in the fluid dynamic sense, i.e. the reflected shock wave speed, based on pressure trace data in the LPST to find relevant information to see how ideally the shock behaves.

6.2 TEMPERATURE CALIBRATIONS WITH CHEMICAL THERMOMETERS

Basics about the chemical thermometer approach can be found in [73,91]. Generally, a species with a simple thermal decomposition pathway that has well-studied rate parameter values is tested in the shock tube with the exact same procedure as for ordinary shocks used to study reacting mixtures. From the species decomposition response to these shocks, the incident velocity to reaction temperature relation curve can be derived using Eq. (2.10) for the temperature and the measured velocity as described in Section 2.6.2. Commonly applied chemical thermometers include 1,1,1-trifluoroethane [47,73–75,91–94] (TFE), cyclopropyl cyanide [76,77] (CPCN), cyclohexane [95], carbon disulfide [96], etc. Each has a different range of temperature suited for calibration. In our study, CPCN (900 K to 1100 K) and TFE (1200 K to 1500 K) are applied. The calibration curve in the HPST is shown in Figure 31.

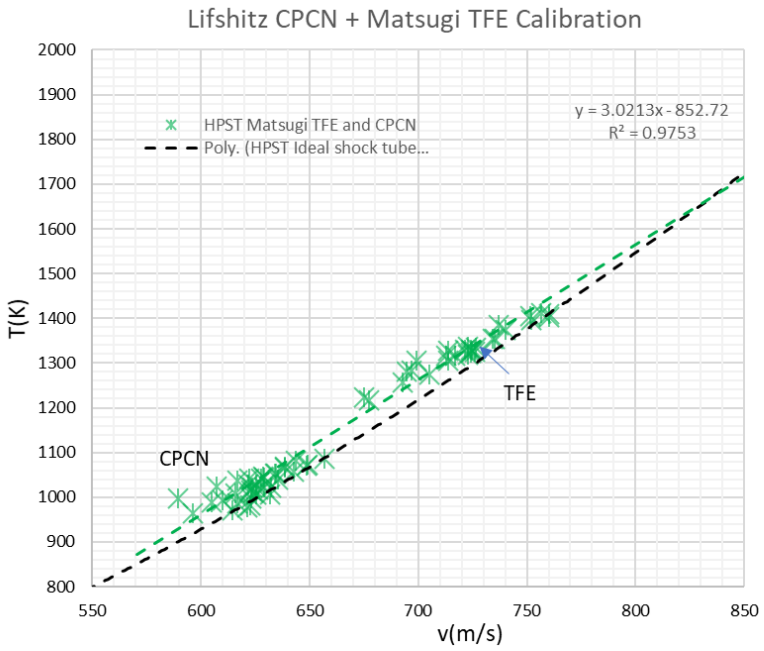

Figure 31: HPST calibration curve obtained from CPCN (100 ppm in argon) and TFE (100 ppm in argon) experiments at 25 atm. The rate parameters for TFE are from Matsugi at high pressure limit.

In the LPST, the calibration curves are obtained similarly. Figure 32 is the calibration curve using both CPCN and TFE together. Note that for the temperature calibrations in the LPST, the velocity at the end wall is extrapolated by the velocities measured by side wall transducers. In the Jet A and JP10 study in the LPST, the temperature from the arrival-time-extrapolated velocities and ideal shock relations are reported and used in the plots. However, it will be shown that the two methods essentially do not have a significant difference (only in average about 6 K). To give a fair comparison with the HPST chemical thermometer calibration data (which used side-wall-velocity-extrapolated data), we use the side-wall-velocity-extrapolated end wall velocity in the temperature calibration data.

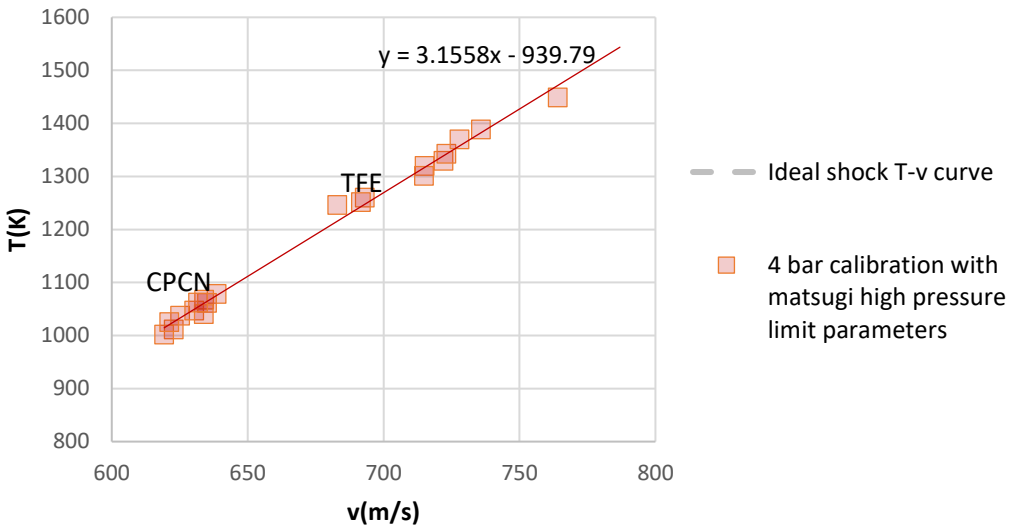

Figure 32: LPST Calibration using CPCN (100 ppm) and TFE (100 ppm) at 4 atm. The TFE rate parameters are the Matsugi high pressure limit ones.

The rate parameters for CPCN isomerization and subsequent decomposition has been obtained theoretically and validated experimentally by Lifshitz [76]. There are three isomerization pathways, which sums up to one global consumption rate

$$k_{\infty} = (3.802 \times 10^{15}) \exp\left(-\frac{29086}{T}\right) [s^{-1}] \qquad (6.1)$$

TFE is the most important thermometer we use because its applied temperature range is where large hydrocarbons break down significantly given HPST standard of 2 ms of reaction time. TFE by itself typically undergoes a unimolecular decomposition at elevated temperatures and forms 1,1-difluoroethylene (DFE) and hydrogen fluoride.

$$\text{TFE} \rightarrow \text{DFE} + \text{HF} \qquad (R7)$$

Many studies[47,74,75,92–94] have been done in the past for the evaluation of the rate parameters of the TFE decomposition reaction. Currently, there are two sources of rate parameter for TFE. The earlier one is by Tsang et al.[94], which gives rate constants in the high pressure limit as

$$k_{\infty} = (4 \times 10^{15}) \exp\left(-\frac{39020}{T}\right) [s^{-1}] \qquad (6.2)$$

At 2.5 bar, the rate constant with low pressure falloff becomes,

$$k_{2.5\ bar} = (7 \times 10^{15}) \exp\left(-\frac{37260}{T}\right) [s^{-1}] \qquad (6.3)$$

The high pressure limit rate parameters are derived from the 2.5 bar rate parameters. The latter are obtained from t-butanol pyrolysis experiments.

Another commonly used source of rate parameters for the TFE decomposition reaction is from Matsugi [74,75,92]. This set of parameters is derived from an RRKM model. The rate constants are given as

$$k_{\infty} = (3.33 \times 10^{14}) \exp\left(-\frac{37363}{T}\right) [s^{-1}] \qquad (6.4)$$

$$k_{1-3\ bar} = (5.71 \times 10^{46}) T^{-9.341} \exp\left(-\frac{47073}{T}\right) [s^{-1}] \qquad (6.5)$$

Note that the $k_{1-3\ bar}$ rate constant expression in Eq. (6.5) is derived by fitting shock tube experimental data in Matsugi et al. [74]. Matsugi in a later study [75] provided new rate constant parameters with Troe's [97] falloff parameters. The two versions of rate constants for 1-3 bar both are assumed to fit well with the experimental data. However, in our later discussions of back calculation, the changing rate constants from Troe's falloff formula cannot be directly applied. Since for the LPST, the temperature calibration is primarily used to understand how temperature calibration works, using the earlier version as Eq. (6.5) is good enough. The falloff from the high pressure limit at 1-3 bar is small, and should be good enough to approximate the 4 bar case.

Our study, as well as other shock tube studies, have adopted these rate parameters from Matsugi, e.g. Lynch et al [47]. In [47], the Matsugi parameters are tested in a miniature shock tube. The discussion in that article also included comparisons with the results from other studies [93,98]. Lynch's article [47] and Matsugi's own articles [74,75,92] are the most recent investigation of the TFE decomposition reaction, with more sophisticated discussions and validation by different groups' data [47,98]. Therefore, Matsugi's parameters are more reasonable at this point.

A comparison of the HPST calibration curve using only TFE alone with rate parameters in the high pressure limit from Matsugi and Tsang is given below in Figure 33:

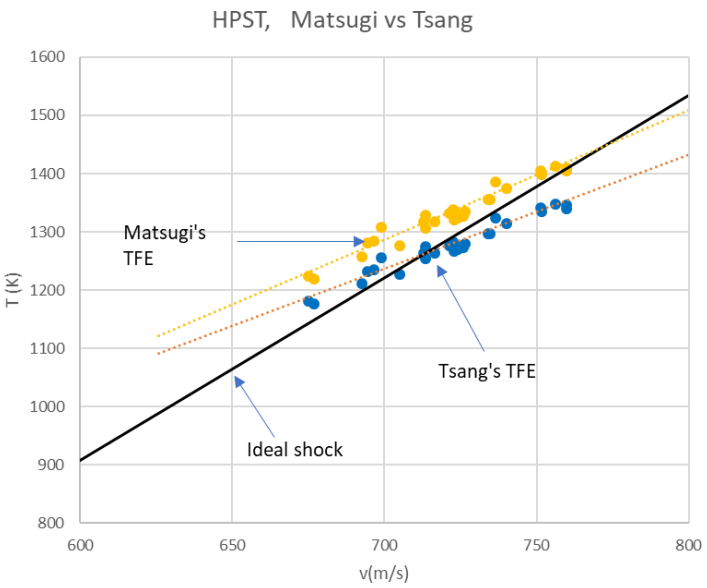

Figure 33: Comparison of TFE calibration results between Matsugi's and Tsang's rate parameters (both in the high pressure limit) in the HPST.

As one can see, Matsugi's parameters tend to predict a higher temperature than Tsang's parameters by about 50 K or more. A direct comparison of the rate constant curves by all the TFE rate parameters discussed above is given in Figure 34:

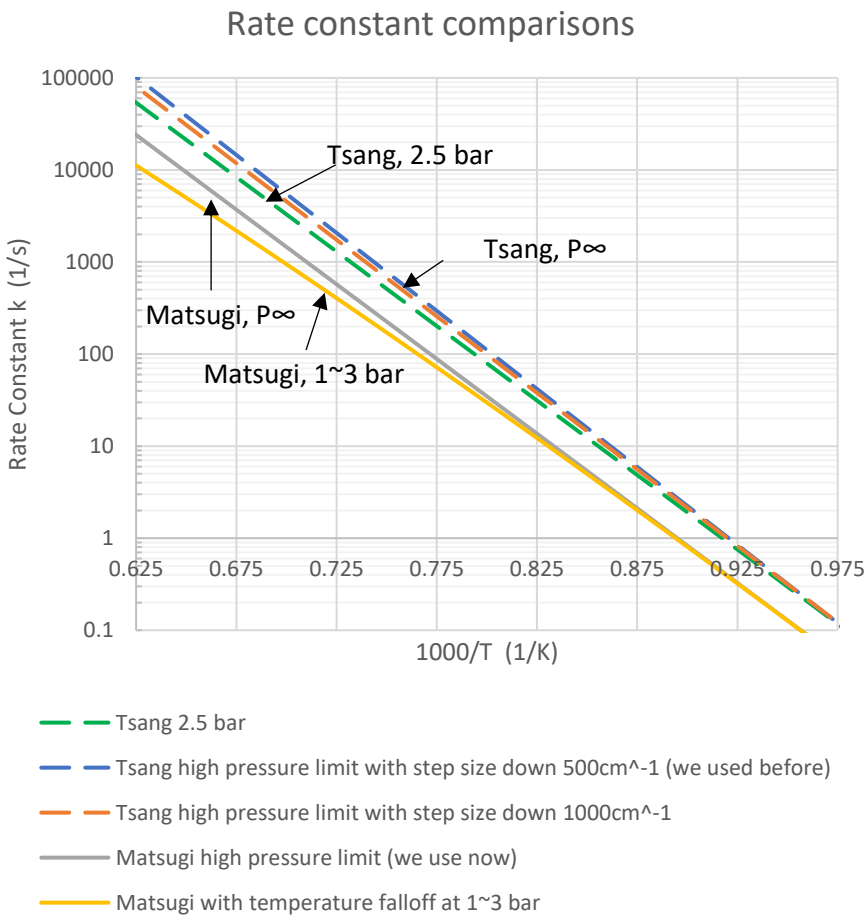

Figure 34: Comparison of all the relevant rate parameters of TFE unimolecular decomposition reaction, including Tsang's high pressure limit by step size down 500cm^{-1} and 1000 cm^{-1}, Tsang's 2.5 bar, Matsugi's high pressure limit, and Matsugi's 1-3 bar.

We did more shocks and compared all the rate parameters previously given for TFE calibration using LPST data, as shown below:

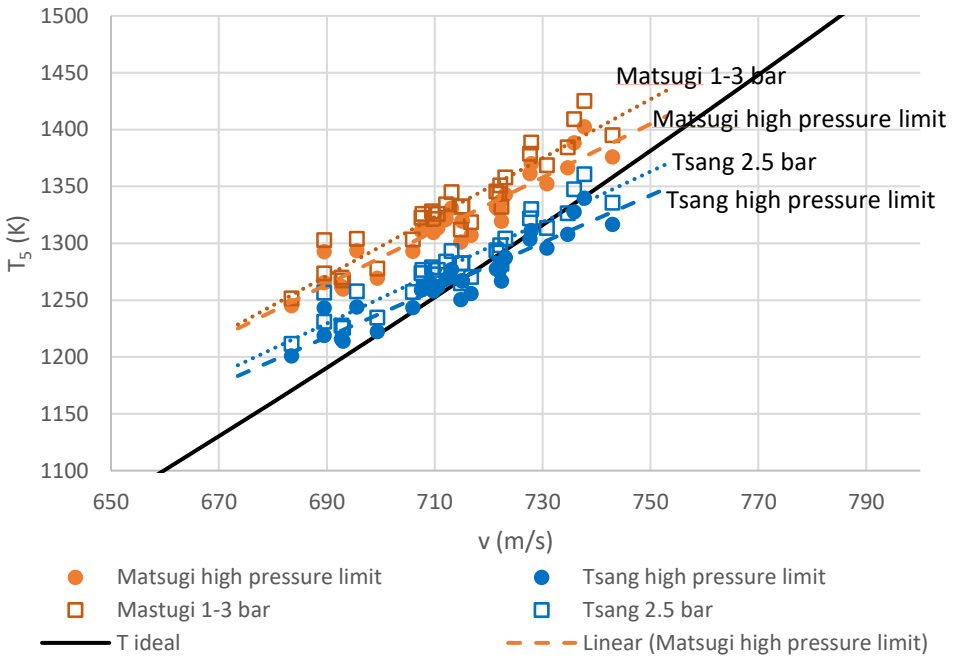

Figure 35: Calibration by TFE in LPST using 4 sets of rate parameters. The shocks are done at 4 atm. TFE mole fraction is 100 ppm and 200 ppm (combined two sets of data).

From Figure 35, we can see that the rate parameters with pressure falloff give a calibration result with a very small difference (5 K – 20 K) with that obtained from the high pressure limit ones.

We now have a comparison between the different rate parameters. Even though there are still uncertainties regarding the rate parameters' qualities, since Matsugi's rate constants are relatively better discussed in recent studies as mentioned earlier, we adopted Matsugi's rate constants for our HPST experiments at this point. For the LPST, since it is a shock tube with well-behaving shocks that is likely to be close to ideal ones, we will use the ideal shock relations to obtain temperature.

6.3 CHANGING PRESSURE SIMULATIONS

6.3.1 BACKGROUND

As we mentioned in Chapter 3, the post-reflected-shock pressure rise exists, and that the dwelling rate (pressure dropping rate) after the rarefaction wave arrives is finite. If it were infinite, the shock would end suddenly with instantaneous vertical pressure drop with respect to time. A shock wave profile from the HPST with a significant finite pressure drop starting around 3.5 msec is shown in Figure 36. The post-reflected-shock pressure rise is especially significant in HPST, because it has a narrow bore of 1" and a strong boundary layer effect. This brings up a concern that whether or not we can take each shock as a constant pressure constant temperature shock if the peak pressure is not constant and does not drop instantly. In this chapter, we will show that though it is better to simulate chemical kinetic results using the actual changing pressure profile such as the one shown in Figure 36, however using the constant pressure approximation is also valid. This makes it convenient for reporting shock tube speciation data and comparing data across laboratories because it provides conditions of a single pressure and time for each experiment.

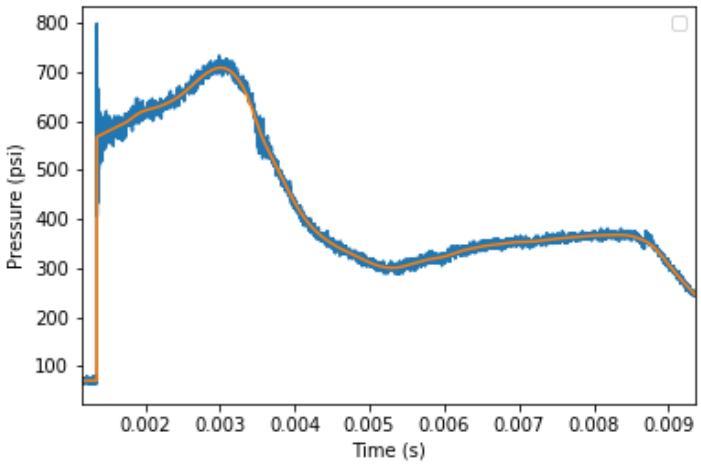

Figure 36: A pressure trace with significant post-shock pressure rise. The trace is taken at end wall of the higher pressure shock tube (HPST) at the UIC High Pressure Shock Tube Laboratory.

A typical way to address this is simply to use the chemical thermometer method as discussed in Section 2.6.2 and Section 6.2, which presents the temperature as a constant for a test gas with diluted mixtures. Another way to address the changing pressure profile as shown in Figure 36 is to use the initial value of T_5 immediately after the reflected shock and the full pressure trace and use that to build or validate a chemical kinetic model by simulating the whole reaction process in the changing pressure mode. The latter method should give the most accurate representation of the physical condition of the reaction process because it accounts for the change in temperature with the change in pressure. However, it is very inconvenient for modeler to use this detailed pressure information for every single shock tube experiment. Both methods have advantages and disadvantages. However, we will later prove that in most cases, the simpler temperature calibration method works well enough to represent the data.

6.3.2 SINGLE REACTION SIMULATION

We can first start from a single reaction model to compare the changing pressure simulation and the constant temperature approach. Recall that isentropic process of a calorically perfect gas can be described by Eq (3.22):

$$\left[\frac{P(t)}{P(0)}\right]^{\frac{\gamma-1}{\gamma}} = \left[\frac{T(t)}{T(0)}\right] \qquad (3.22)$$

This equation can be applied to a dilute mixture of TFE (~100 ppm) in argon undergoing reaction R7 after the arrival of reflected shock, in order to calculate the temperature history $T_5(t)$ (t is a time within the isentropic process), associated with the pressure history, given $T_5(0)$ which ideally can be obtained from the incident shock velocity. The pressure history from the pressure trace is obtained through smoothing methods discussed in Section 3.5.2. An example of the regression is the orange curve in Figure 36, which is a smoothing curve of the noisy raw pressure trace in blue. An example of a $T_5(t) - t$ curve calculated from $P_5(t) - t$ curve is shown in Figure 37:

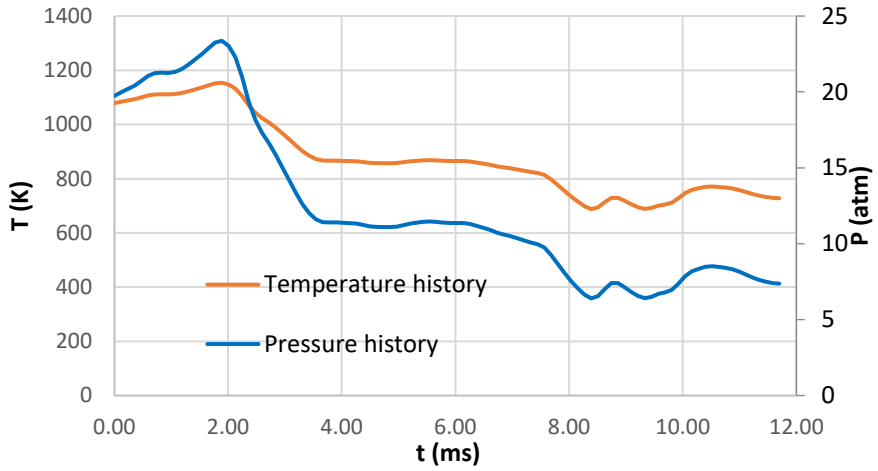

Figure 37: Schematic of temperature history obtained from the pressure history after arrival of a reflected shock wave in the HPST.

Once we have the temperature history, we can simulate the reaction timewise to obtain the extent of reaction. Now we want to see whether it can be presented as a constant temperature process in a schematic below.

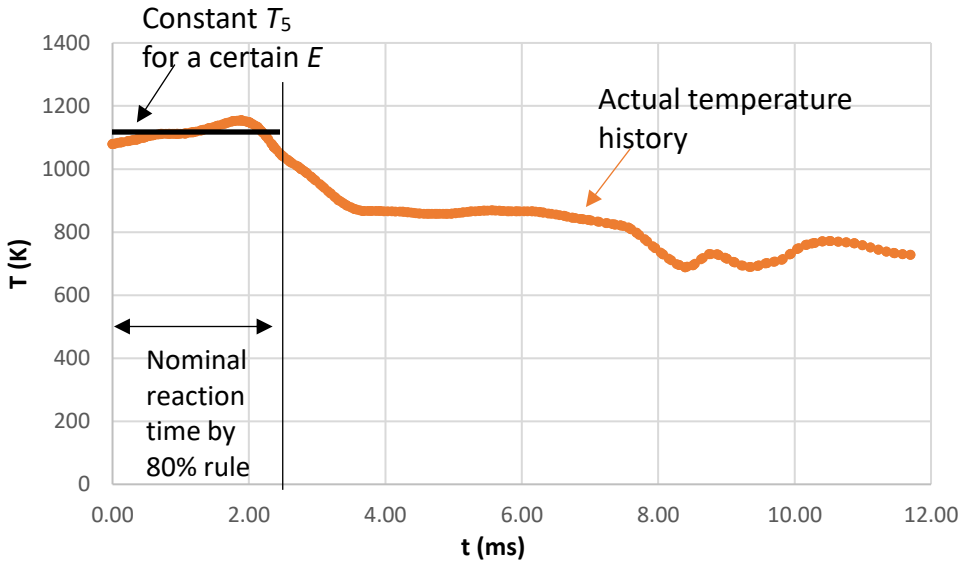

Figure 38: Schematic for the constant temperature obtained from the actual temperature history in the HPST, using a reaction time by the 80% rule. *E* is the activation energy of a specified reaction.

Tang el al [73] discussed this problem, and gave Equation (6.6) that gives the relation between an averaged constant temperature $T_{5,avg}$ and a changing temperature history profile. We rewrite the equation with slight modification here (t_∞ replacing τ in the integral of original expression of the equation):

$$\int_0^{t_\infty} e^{-E/(RT_5(t))}dt = \tau e^{-E/(RT_{5,avg})} \qquad (6.6)$$

where $T_5(t)$ is the temperature at time t, $T_{5,avg}$ is the "averaged" temperature for this process starting from $t = 0$ to $t = t_\infty$. $T_{5,avg}$ could be used as a constant temperature, coupled with the corresponding reaction time τ, in the constant pressure simulation. While Eq (6.6) is primarily used in Tang's study to back calculate from an experimentally obtained $T_{5,avg}$ the value $T_5(0)$,

here we can use this relation in the forward direction to obtain an averaged constant temperature $T_{5,avg}$ from the unimolecular single reaction process under changing pressure integrated on the left side of Equation 6.6. One can always calculate a $T_{5,avg}$ for a unimolecular single reaction process that can perfectly duplicate the simulation result from the changing pressure result, given a reasonable choice of τ. This conclusion holds even if we do not have a very precise value of activation energy E for the reaction. The predicted $T_{5,avg}$ from the changing temperature history shown in Figure 38 with a nominal reaction time determined by the 80% rule is plotted as a function of E/R as used in Eq. (6.6) in Figure 39.

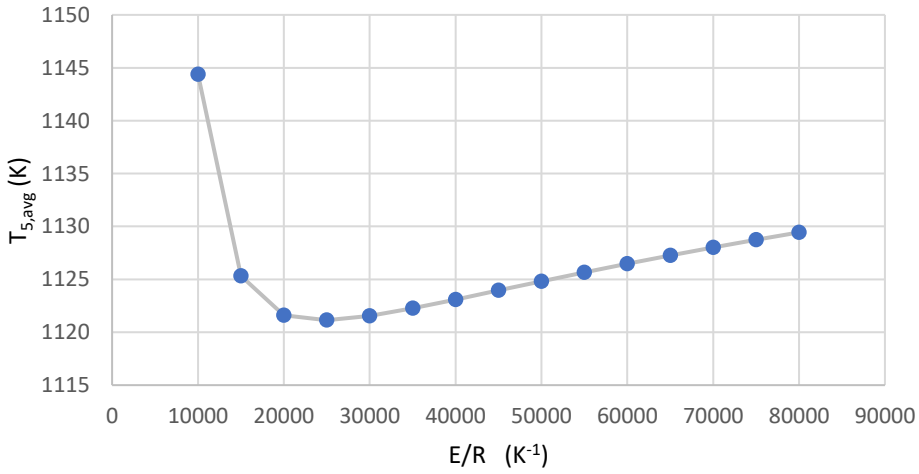

Figure 39: $T_{5,avg}$ calculated when using one step decomposition chemical reactions of different E (activation energy).

It is shown in Figure 39 that the average temperature $\boldsymbol{T_{5,avg}}$ does not strongly depend on the activation energy $\boldsymbol{E}$ except for very low values of $\boldsymbol{E/R}$. For TFE, the value for $\boldsymbol{E/R}$ from Tsang (39020 K^{-1}) and Matsugi (37363 K^{-1}) only has 1637 K^{-1} of difference in the high pressure limit, which only results in less than 1 K of difference in $\boldsymbol{T_{5,avg}}$. As long as the arbitrary value of $\boldsymbol{E}$ is

not too low for the corresponding temperature, $\boldsymbol{T_{5,avg}}$ will not be very sensitive to it. This is important because it means that the calibrated temperature $\boldsymbol{T_{5,avg}}$ generated by the chemical thermometer TFE can account for the changing pressure profile in our shock experiment and that we can apply $\boldsymbol{T_{5,avg}}$ to other unimolecular reactions with a large-enough $\boldsymbol{E}$ in a new shock experiment without a concerning loss of precision, if a similar pressure history can be replicated with the same $\boldsymbol{T_5(0)}$ (or velocities) in that shock. The new reactions can be, for example, the C-C scission of hydrocarbons like $C_4H_{10}(+M) = nC_3H_7+CH_3(+M)$, or even the HyChem lumped fuel pyrolysis reaction R1. More specifically, if we use the $\boldsymbol{T_{5,avg}}$ obtained from TFE decomposition and apply it to another reaction like above to simulate the species profile, then we will most likely see only a very small temperature shift. This temperature shift should be well within the temperature uncertainties of current shock experiments and kinetic models. For reactions such as the H-abstraction reactions that have far lower activation energy, they cannot be calibrated by the chemical thermometers such as TFE. However, we consider that the reaction rates of these reactions in complex reaction networks in combustion may be limited by the species concentration instead of the rate constant values. The case in complex reaction networks are more complicated to analyze. It will be discussed later in the chapter.

Note that when the $n \neq 0$ in the modified Arrhenius equation, we also need to consider n. A simulation in the same manner can be performed using:

$$\int_0^{t_\infty} T_5(t)^n e^{-E/(RT_5(t))} dt = \tau T_{5,avg}^n e^{-E/(RT_{5,avg})} \qquad (6.7)$$

Anyway, a theoretical basis is presented for unimolecular single reactions that allows using a chemical thermometer to derive a reliable constant temperature that corresponds to a $T_5(0)$ or velocity, when shock pressure profiles are repeatable over experiments.

6.3.3 BACK CALCULATION FOR POST SHOCK INITIAL TEMPERATURE

In the ideal condition, $T_5(0)$ should be directly obtained from the v-T relation of ideally behaving shock through Eq (2.6) for dilute fuel or the FROSH code [61] when there is a high content of fuel. However, practically there are some potential factors that may affect the result of either approach. These factors include a small bias of the arrival time reading of the pressure transducer which affects the measured shock velocity and boundary layer effects[47,66,67] that will change the $T_5(0)$ value of the reflected shock wave. The discrepancy between the back-calculated $T_5(0)$ and the $T_5(0)$ obtained from the ideal shock relation (ideal v-T curve) can be observed through back-calculation. Tang et al.[73] used equation (6.6) (with $T_{5,avg}$ replaced by $T_{5,cal}$) to back-calculate the initial $T_5(0)$. Typically, the calibrated temperature $T_{5,cal}$ is first obtained from a chemical thermometer such as TFE. The right side of Eq (6.6) is thus experimentally obtained, and the $T_5(0)$ can be calculated from the left side of Eq (6.6) iteratively by a simple search method. It should be pointed out that no matter how the nominal reaction time τ is defined, the value of the right side of Eq (6.6) stays intact when we do the temperature calibration. It only depends on the extent of reaction x and the *A* factor of the reaction. This is because Eq (2.9) which is used in the calibration can be rewritten as:

$$\tau e^{-E/(R\boldsymbol{T_{5,avg}})} = -\frac{\ln(1-x)}{A} \qquad (6.8)$$

The left side of Eq. (6.8) is the same as the right side of Eq. (6.6). In fact, Eq. (6.6) originates from Eq. (6.8), and uses it to equate the changing temperature expression form to the constant temperature form through the common *x*. The value of $T_{5,cal}$ will adjust to τ through Eq (2.9) for a given extent of reaction. The E on the left side of Eq (6.6) has to be the same activation energy used in Eq (2.9) in the temperature calibration. Therefore, Eq. (6.6) can be used for back-calculation and gives the same $T_5(0)$ value even when a person is not using the 80% rule, e.g. using 75%, 85% rules.

Back-calculation was applied to our new experiments of TFE and CPCN in the HPST, as shown below in Figure 40. The end time, t_∞ of the integral in Eq (6.6) is 12 ms, which is long after the pressure has dropped below 80%.

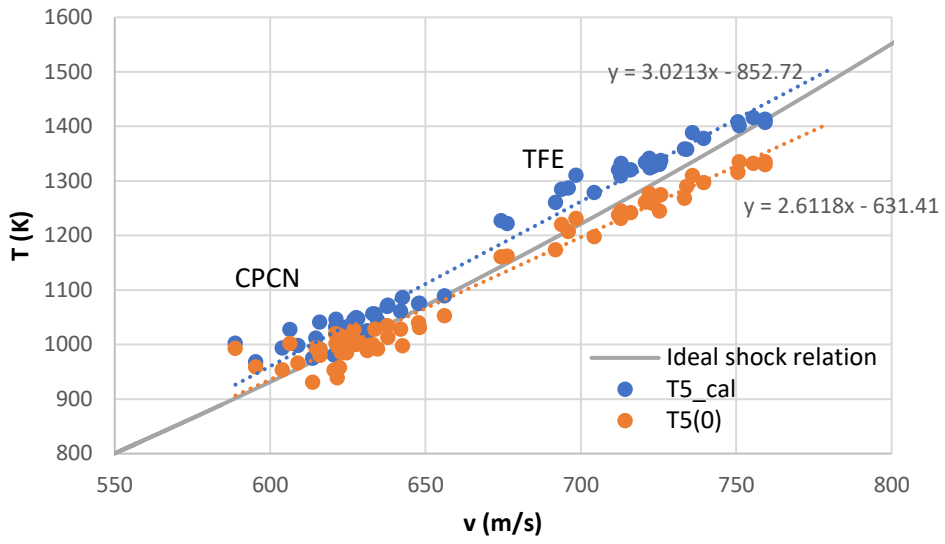

Figure 40: Comparison of $T_{5,avg}$ and $T_5(0)$ derived from back calculation on the CPCN and TFE calibration (Matsugi's high pressure limit) in the HPST at 25 atm.

There are discrepancies between our calibrated/back-calculated $T_5(0)$ and that derived from the ideal relation Eq (2.6) in the HPST, with the former being lower in the temperature range of our most interest (1150 K to 1400 K), as can be seen from the orange dotted line and the gray line in Figure 40. This difference becomes larger with temperature. If Tsang's rate parameters for TFE were applied here, the back calculated $T_5(0)$ would be even further below the ideal shock relation curve. One reason may be that the CPCN data is too scattered and causes a strong uncertainty in the slope of the linear fit, or that the linear fit approximation creates too large a bias. Nevertheless, the scatter of CPCN does not change the fact that most of $T_5(0)$ from the TFE back calculation (orange in Figure 40) is below the $T_5(0)$ calculated from the ideal shock v-T curve (gray in Figure 40). One can observe in Figure 40 that the TFE calibration data form a slope that is smaller than for the ideal v-T curve, which partially contributes to the difference between the calibrated $T_5(0)$ and ideal v-T, i.e. ideal $T_5(0)$ curve at higher temperatures. This is also observed in previous study

done by Malewicki [71] on this same shock tube, though they used Tsang's rate parameters. Judging from the above analysis, it is highly possible that the $T_5(0)$ derived from the ideal shock relation and the velocity measured in the HPST is truly higher than the actual $T_5(0)$. The physical reason, i.e. fluid dynamical effects, or measurement reason for this difference will be investigated in the future.

There are three potential reasons for this discrepancy. One is that the shock wave does not behave ideally at higher temperature due to some fluid dynamics reasons. The second possible reason is that the velocity measurement is incorrect. The third one is that the TFE is not measured correctly, or the rate parameters are somewhat off from the real values.

One can also observe that the gap between the $T_5(0)$ and $T_{5,cal}$ increases with velocity. The reason is that the pressure rise of a shock wave in the shock tube will increase with velocity and temperature. This should be due to the boundary layer effect becoming more significant as Reynold's number increases and as the viscosity grows due to the temperature rise.

The back calculation of $T_5(0)$ was also done for the LPST. The shocks in this wide bore shock tube (2.5" ID) has a low pressure rise in the post-reflected shock region, as shown in Figure 41, in contrast to Figure 36 which came from the HPST. The results of the back calculation for the LPST are shown in Figure 42.

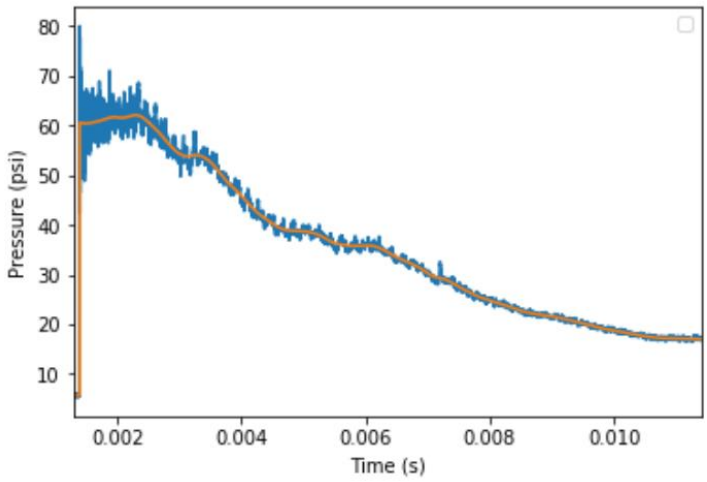

Figure 41: A sample pressure trace profile from the end wall pressure transducer in the LPST. Blue curve is the raw signal. Orange line is the smoothed curve.

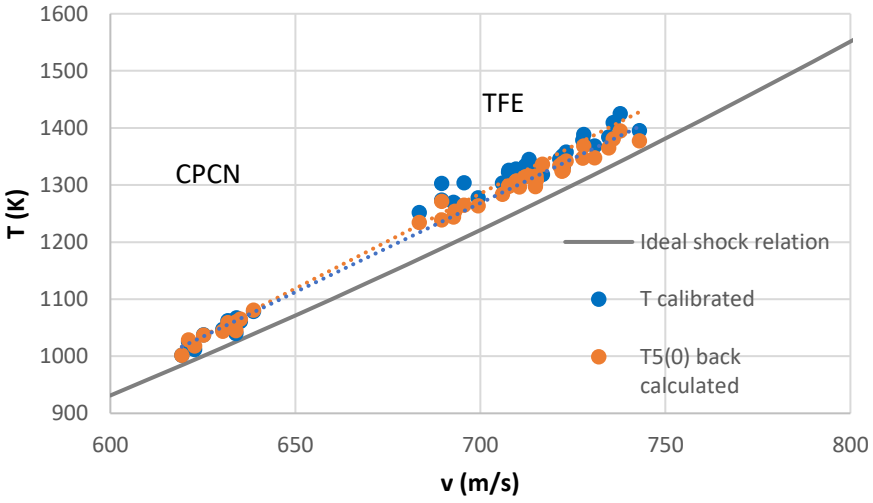

Figure 42: Comparison of $T_{5,avg}$ and $T_5(0)$ derived from back calculation on the CPCN and TFE calibration (Matsugi's 1-3 bar parameters) in the LPST at 4 atm.

As one can see here, in the LPST, since the pressure rise is significantly reduced, the back-calculated $T_5(0)$ is very close to the calibration curve. However, it is in this case higher than the

ideal v-T curve. The reason for this discrepancy is not understood yet. As a temporary solution, we consider this shock tube as one close to behaving ideally and take use the ideal shock relation for the $T_5(0)$, instead of the TFE back-calculations. This issue, along with the discrepancy of $T_5(0)$ in the HPST, will be discussed regarding some preliminary results and future work later in the chapter.

6.3.4 CHANGING PRESSURE SIMULATIONS OF COMPLEX REACTION NETWORK

So far, only the single reaction scenario has been discussed regarding the changing pressure simulation and its constant-pressure-simulation approximation, as well as the temperature calibrations using chemical thermometer on shocks with non-negligible pressure attenuation. For simulations on complex reaction networks, we need to apply Eq (3.20) and Eq (3.21). The reaction network forms a highly non-linear process in which species concentrations are determined by multiple reactions. The formation reactions and consumption ones dominate at different reaction times in a shock experiment. Some reactions will only be significant later in the reaction time because their reactants are only available after being generated by some other reactions. In this case, a calibrated temperature may not be valid for averaging the reaction history of all the reactants under the changing pressure and temperature. This raises concerns about using a constant pressure simulation to replicate shock tube speciation results obtained using GC and MS instruments. Therefore, simulations of the complex chemistry of Jet A pyrolysis were conducted using both the constant pressure and changing pressure simulation techniques. The changing pressure simulations were conducted for the experiments, i.e. using experimentally measured

conditions as input, including the pressure trace, and use the HyChem models to simulate each experimental data point. The simulations were done using CHEMKINPRO in batch, with automated pressure history profile generation for the software input.

As a starting point of all the scenarios in which the two pressure simulation approaches will be compared, our first attempt will be to use the ideal shock v-T relation curve to get the $T_5(0)$ in the HPST for use in the changing pressure simulation. The results of selected species for the Jet A pyrolysis experiments at 25 atm in the HPST are shown in Figure 43.

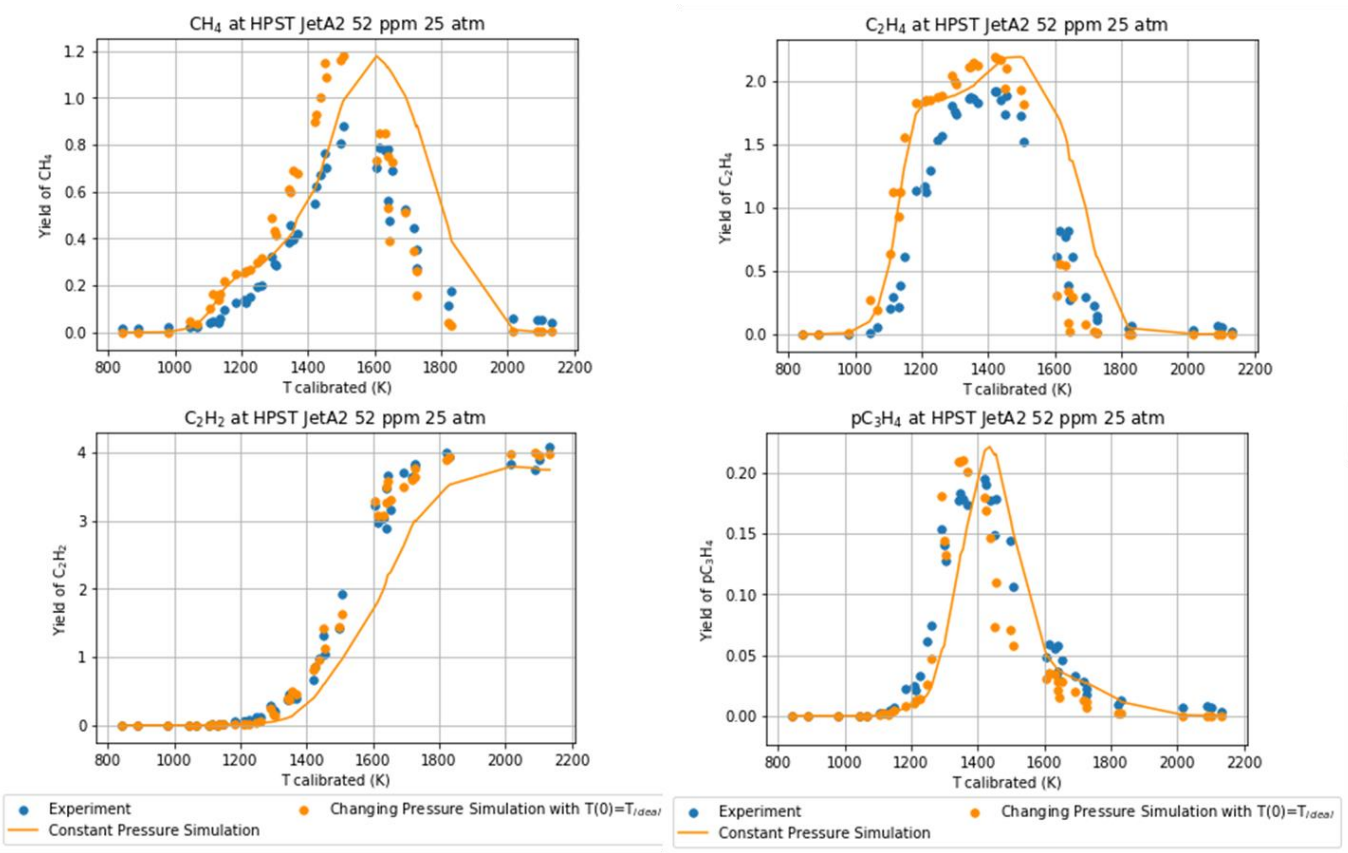

Figure 43: Comparison between the changing pressure simulation (orange dots) and constant pressure simulation (orange line) of Jet A pyrolysis in the HPST at 52 ppm 25 atm. The $T_5(0)$ used

in the changing pressure simulation is simply from the ideal shock v-T relation. The constant pressure simulation applies calibrated temperatures from CPCN and TFE. Both changing and constant pressure simulations are plotted against the calibrated temperature of each shock for convenience of comparison. Experimental data (blue dots) are also added for comparison.

As one can see, the changing pressure simulation is giving similar results to the constant pressure one below 1300 K. At higher temperature, this is changed dramatically as shown in Figure 43. The dramatic change could be due to the predicted $T_{5,cal}$values above 1350 K are simply from the extrapolation of the fitted line of $T_{5,cal}$ derived from the calibration data. Its slope differs from the ideal v-T curve strongly as temperature rises and eventually extrapolates to below the ideal v-T curve. However, it is surprising that using the $T_5(0)$ from the ideal v-T curve makes our changing pressure simulations fit the experimental data much better in the high temperature region, especially for C_2H_2. This may be just a coincidence but merits further investigation.

What is also interesting shown in Figure 43 is that quite often the fluctuations in experimental data from each shock experiment are to a certain level replicated by the changing pressure simulation. For example, the peak region of C_2H_4 at around 1300 K and the dropping region of CH_4 at between 1600 K to 1800 K, are both captured by the changing pressure simulation. This replication demonstrates that the experimental result of each shock is dependent on the pressure history of each shock and suggests that a more consistent pressure profile of the shocks should give a less scattered speciation profile.

To evaluate how the changing pressure simulation compares with a constant pressure simulation, we need to conduct the former simulation with the $T_5(0)$ back calculated from the same $T_{5,cal}$ that is used in the latter simulation since as was discussed earlier, the $T_5(0)$ obtained from the

calibrated temperature is not the same, although close, as the $T_5(0)$ obtained from the ideal shock relations. This back calculation of $T_5(0)$ was done on the same Jet A fuel pyrolysis experiments at 25 atm in the HPST as shown in Figure 43. The results in this case are shown in Figure 44 and Figure 45.

The changing pressure simulation and constant pressure simulation match well over the whole temperature domain. In Figure 44, the species that can be directly formed from the HyChem fuel pyrolysis submodel are given, e.g. the alkenes, aromatics, and CH_4. Since in the rising part of the profiles in lower temperature, only one single pyrolysis reaction R1 has significance, it is not surprising to see a good match, given our previous discussion on single reaction simulations. However, in this comparison, even the chemical species produced in the temperature region dominated by the foundation chemistry show excellent matches between the two prediction approaches. Figure 45 shows the comparisons for the species C_2H_6, C_2H_2, pC_3H_4, and aC_3H_4, which are not directly formed by the fuel pyrolysis in the HyChem model. In the Monte Carlo simulation analysis in Section 4.1.3, we have shown that the formation of these species is dominated by the foundational chemistry. We can thus assume that constant pressure simulation results and changing pressure simulation results would also match each other in simulating the complex reaction network of the foundational chemistry and Figure 45 shows that they do. This excellent match between the constant pressure and changing pressure simulations when the appropriate $T_5(0)$ is used in the changing pressure simulation is a significant result, given the concern and suspicion on the temperature calibration method, narrow bore shock tubes, and the GC sampling approach for speciation. The results shown in Figure 44 and Figure 45 justifies these experimental methodologies which is a major conclusion of this thesis.

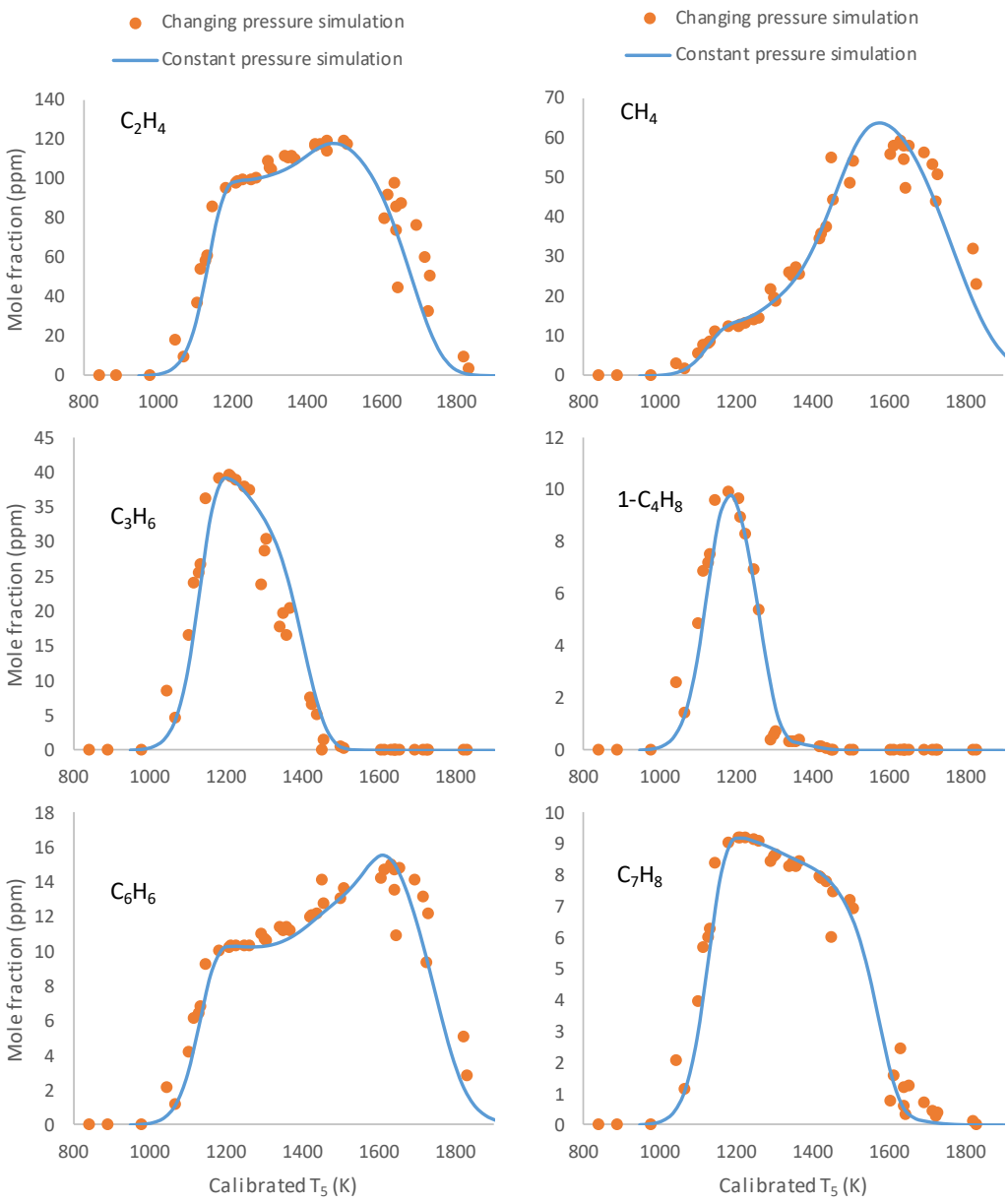

Figure 44: Comparison between the changing pressure simulation (orange dot) and constant pressure simulation (blue line) of Jet A pyrolysis in the HPST at 52 ppm 25 atm. The $T_5(0)$ used in the changing pressure simulation is from the result of back-calculation of the CPCN-TFE calibration curve. The constant pressure simulation applies calibrated temperatures from CPCN and TFE. Both changing and constant pressure simulations are plotted against the calibrated temperature of each shock for convenience of comparison. The species selected are ones that can be "directly" formed from the fuel pyrolysis submodel in the HyChem model.

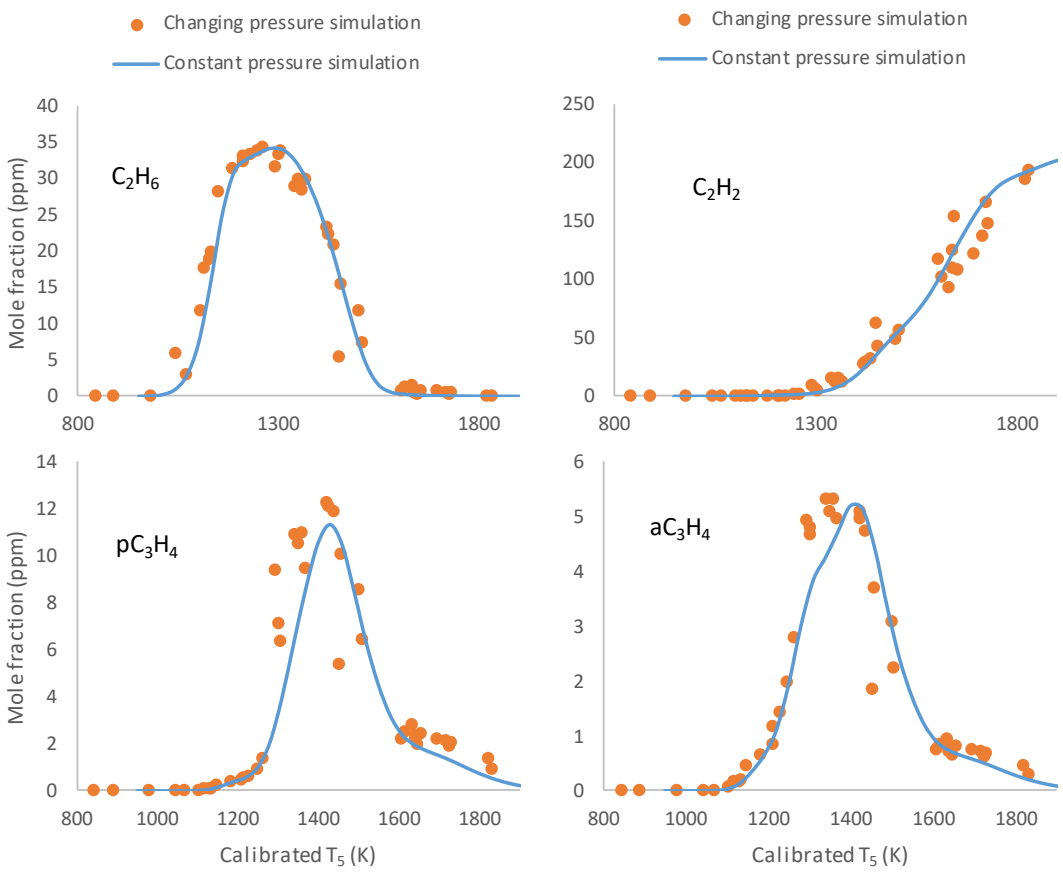

Figure 45: Comparison between the changing pressure simulation (orange dot) and constant pressure simulation (blue line) of Jet A pyrolysis in the HPST at 52 ppm 25 atm. The $T_5(0)$ used in the changing pressure simulation is from the result of back-calculation of the CPCN-TFE calibration curve. The constant pressure simulation applies calibrated temperatures from CPCN and TFE. Both changing and constant pressure simulations are plotted against the calibrated temperature of each shock for convenience of comparison. The species selected are ones that cannot be "directly" formed from the fuel pyrolysis submodel in the HyChem model, but rather have to go through additional steps of the foundational chemistry.

Despite the overall agreement between the two different simulation approaches, there are still some evident mismatches such as between 1300 K to 1400 K for pC_3H_4. This mismatch may be due to the difference in the individual pressure profiles between the shocks fired for Jet A and those fired

for TFE in the same temperature region. These mismatches mostly happen in the region where the Monte Carlo analysis shows large sensitivity of the species to rate parameters, e.g. the pC_3H_4 peak, the decomposition region of C_2H_4 and CH_4. Therefore, maybe the Monte Carlo analysis can give us also some suggestions on a species' likelihood of being sensitive to perturbations other than rate constants at a certain temperature.

6.3.5 MORE COMPARISONS OF THE CONSTANT/CHANGING PRESSURE

In the previous section, we compared the constant and changing pressure simulation approaches only on the Jet A model and experimental conditions in the HPST (dilute mixture, high pressure, high rise of pressure). In this section, such analysis is extended to a few more domains. The JP10 HyChem model, LPST conditions, and concentrated Jet A/argon mixtures will be tested as well in the simulation comparisons.

The simulations for the experimental conditions of the JP10 72 ppm/25 atm experiments in the HPST were conducted using the JP10 model. The results shown in Figure 46 and Figure 47 indicate that for the majority of the species, the two simulation approaches match well with each other, just as for the Jet A simulations (52.3 ppm/25 atm in HPST) in the last section. The decomposition region of C_2H_4 between 1500 K to 1800 K shows some difference between the two predictions, which can be seen as an estimated 30 K temperature displacement. Among the species that can only be formed through foundational chemistry, as given in Figure 47, aC3H4 and pC3H4 show significant improvement compared to the earlier Jet A case. One species, C_2H_6 shows considerable difference between two predictions. However, in the previous analysis of the HPST Jet A

simulation, C_2H_6 showed one of the best matches. However, it may be because C_2H_6 in the JP10 simulation has a very small formation, and the mismatch is more obvious. The small differences between the two predictions seen for other species may also be caused by the overall strong mathematical nonlinearity of the chemical kinetic model (the average temperature cannot represent the temperature history of a complex reaction network that has complex mathematical relations among species and complex shapes of species concentration history). However, it is also possible that it is caused by shocks not fired in a perfectly consistent way with the TFE ones, especially in the high temperature region. Nevertheless, the overall pattern in the JP10 simulation analysis still strongly support our previous conclusion that most of the important species profiles show good consistency between the changing pressure simulations and the constant pressure simulations. Only certain regions that are sensitive to foundational chemistry have limited number of species showing some evident difference but in an acceptable degree. The foundational chemistry submodel forms a complex reaction network, rather than the simpler one formed by the 7 parallel reactions in the fuel pyrolysis submodel. This indicates that the constant pressure approach (or temperature calibration) can be applied to complex reaction networks with satisfying qualities, at least in the cases presented here.

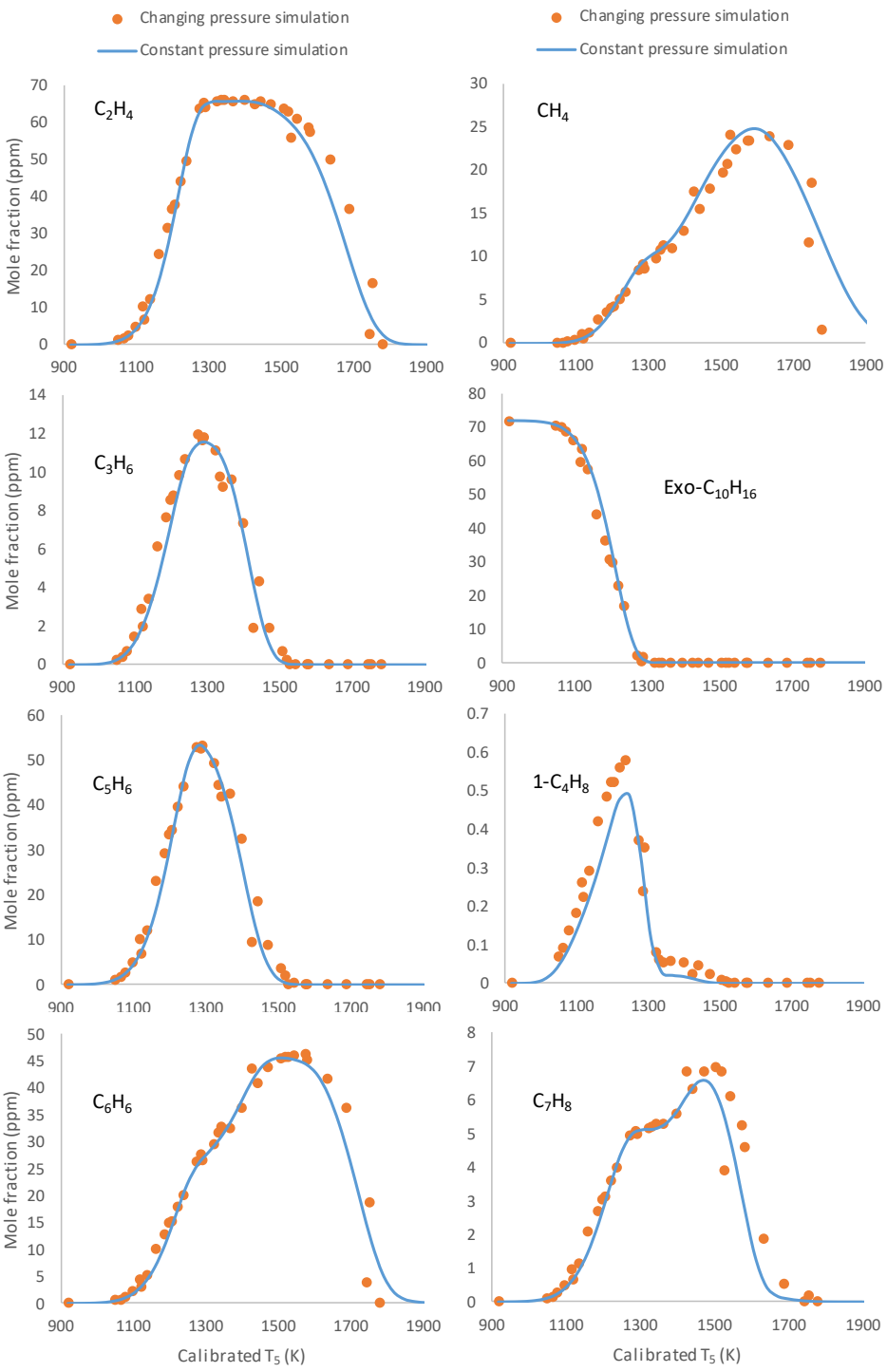

Figure 46: Comparison between the changing pressure simulation (orange dots) and constant pressure simulation (blue line) of JP10 pyrolysis in the HPST at 72 ppm 25 atm. The $T_5(0)$ used in the changing pressure simulation is from the result of back-calculation of the CPCN-TFE

calibration curve. The constant pressure simulation applies calibrated temperatures from CPCN and TFE. Both changing and constant pressure simulations are plotted against the calibrated temperature of each shock for convenience of comparison. The species selected are ones that can be "directly" formed from the fuel pyrolysis submodel in the HyChem model.

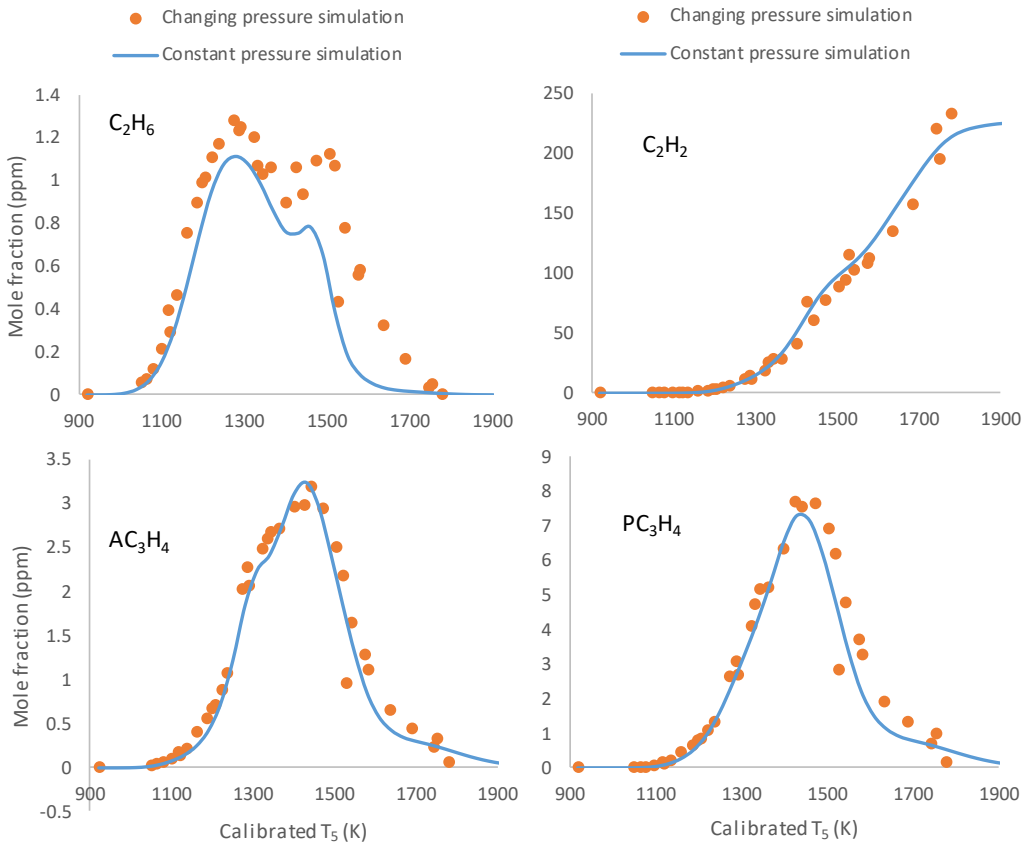

Figure 47: Comparison between the changing pressure simulation (orange dots) and constant pressure simulation (blue line) of Jet A pyrolysis in the HPST at 52 ppm 25 atm. The $T_5(0)$ used in the changing pressure simulation is from the result of back-calculation of the CPCN-TFE calibration curve. The constant pressure simulation applies calibrated temperatures from CPCN and TFE. Both changing and constant pressure simulations are plotted against the calibrated temperature of each shock for convenience of comparison. The species selected are ones that cannot be "directly" formed from the fuel pyrolysis submodel in the HyChem model, but rather have to go through additional steps of the foundational chemistry.

The HPST analyses comparing the two simulation approaches are complete. The comparisons were initiated because the pressure traces for the HPST shocks have more attenuation (sometimes even over 30% pressure rise in the peak pressure), which has raised significant concerns about the quality of both our simulation and experimental data that is presented as under constant pressures. The analyses nonetheless demonstrate that the species predictions from the constant pressure simulation for the two jet fuels using the calibrated temperature from our TFE and CPCN experiments can well replicate the changing pressure simulation approach when using the back calculated $T_5(0)$ from TFE and CPCN calibrations.

We now further analyze the situation in the LPST. We consider the pressure attenuation to be small and that the shock waves behave close to ideal. In the changing pressure simulations, we did not need to use the back-calculated results, and directly used the ideal shock v-T relation to get our $T_5(0)$. Moreover, for the constant pressure simulation, T_5 cannot be approximated as a constant value determined either by calibration or by the velocities for the high-fuel-content Jet A simulations, because endothermic reactions of the concentrated fuel change the temperature during the course of the reaction progress. Therefore, we also use the same $T_5(0)$ from the ideal v-T curve as the initial post-shock temperature and solve the energy equation in the constant pressure simulation for the LPST. $T_5(0)$ is also the temperature that is reported in the experimental data. The constant pressure simulation result is also presented in a pointwise mode in the plots in Figure 48 and Figure 49, to reflect actual reaction time fluctuations and the trivial differences of changing/constant pressure results that will otherwise be unobservable in a line

plot. The comparison results of the Jet A concentrated simulations are shown below in Figure 48.

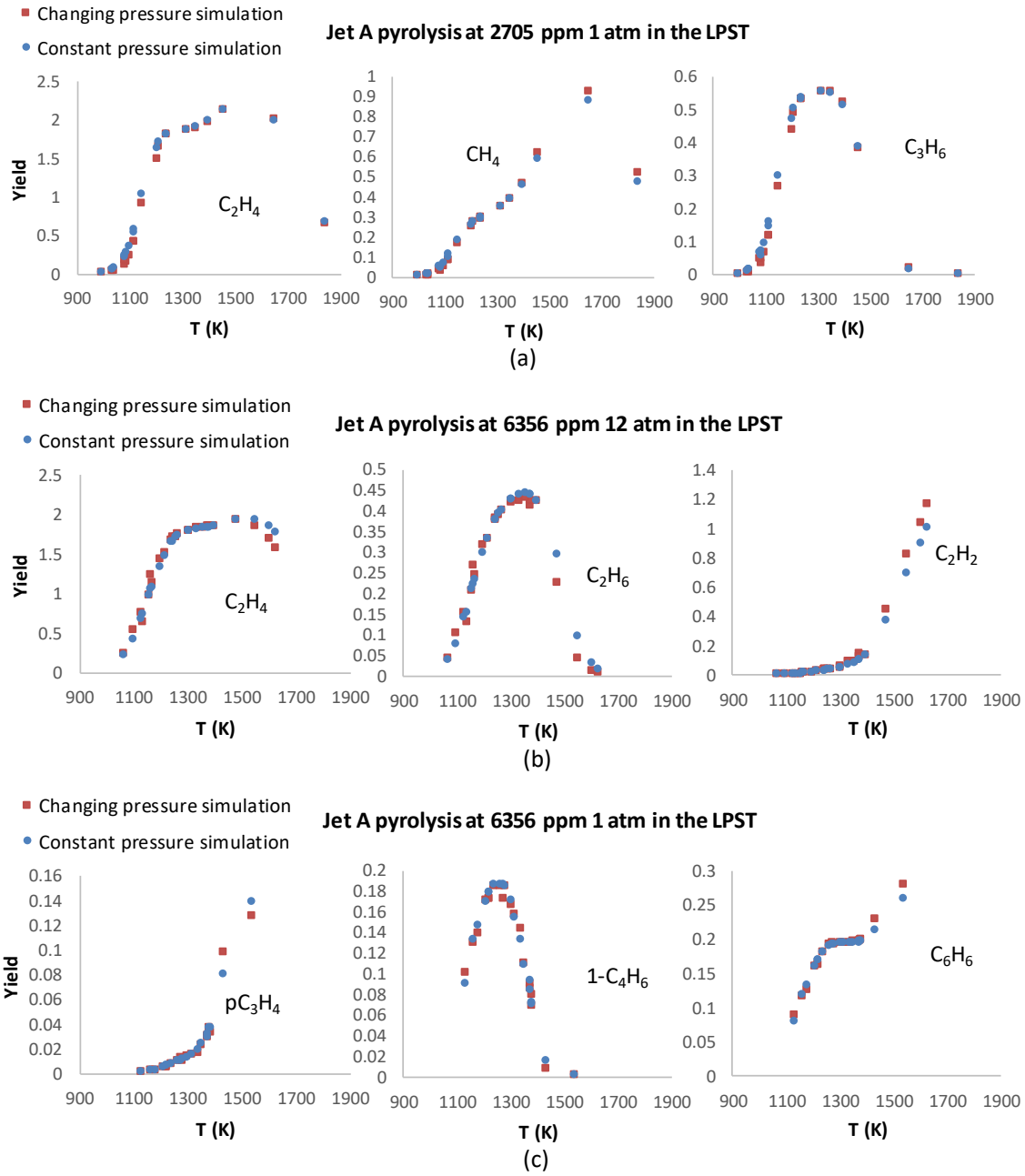

Figure 48: Selected examples of the comparisons between changing pressure simulation (orange dots) and constant pressure simulation (blue dots) in the experimental conditions of three sets of experiments in the LPST: (a) Jet A 2705 ppm 1 atm; (b) Jet A 6356 12 atm; (c) Jet A 6356 1 atm.

The $T_5(0)$ of the changing pressure simulation and the $T_5(0)$ for the constant pressure simulation are both from ideal shock v-T relation.

In general, the simulations match each other better than for HPST dilute cases. These results show that the high-fuel-content simulations as well as the LPST profile also work well in mapping changing pressure history chemical processes to constant pressure ones. Note that for the LPST we did not use any back-calculation curve to get $T_5(0)$ and that we also used that same $T_5(0)$ instead of a calibrated or averaged T_5 in the constant pressure method as well, unlike in the HPST case. The fact that we see great match by using the same $T_5(0)$ in both changing pressure simulation and constant pressure simulations in the LPST indicates that the shock profiles in the LPST are flat enough to be approximated as constant pressure reaction process, at least for relatively low temperatures. Note that this doesn't mean an equally flat temperature profile, since the energy equation will account for the temperature change due to the reactions.

Indeed, in a pointwise way, the difference between changing pressure and constant pressure simulations can be interpreted as large on a percentage basis for the mole fraction of a species at a specific fixed temperature. However, that difference can be greatly reduced by basically a small temperature displacement.

Finally consider the JP10 75 ppm 12 atm comparison simulations for the LPST, as shown in Figure 49. As expected, the results have a far better match and less scatter compared to the HPST case. It can still be observed that in the C_2H_4 decomposition profile above 1600K, the displacement in the vertical direction between the two simulations is large. It is due to the high attenuation rate in the high temperature region, making it hard to assume a flat pressure profile.

Therefore, we probably need to refine the high temperature case for this LPST simulation comparison but overall, we have demonstrated that the LPST simulations can also use constant pressure approximation. It is also shown that in contrast to the HPST, the flat pressure profile in the LPST enables its simulation to be approximated as a constant pressure one using the initial temperature $T_5(0)$, instead of using an average temperature by calibration or Eq (6.6) as in the HPST. This enables us to provide a temperature input in the constant pressure simulations for high-fuel-content test mixtures, even though the temperature will drop during the reaction process.

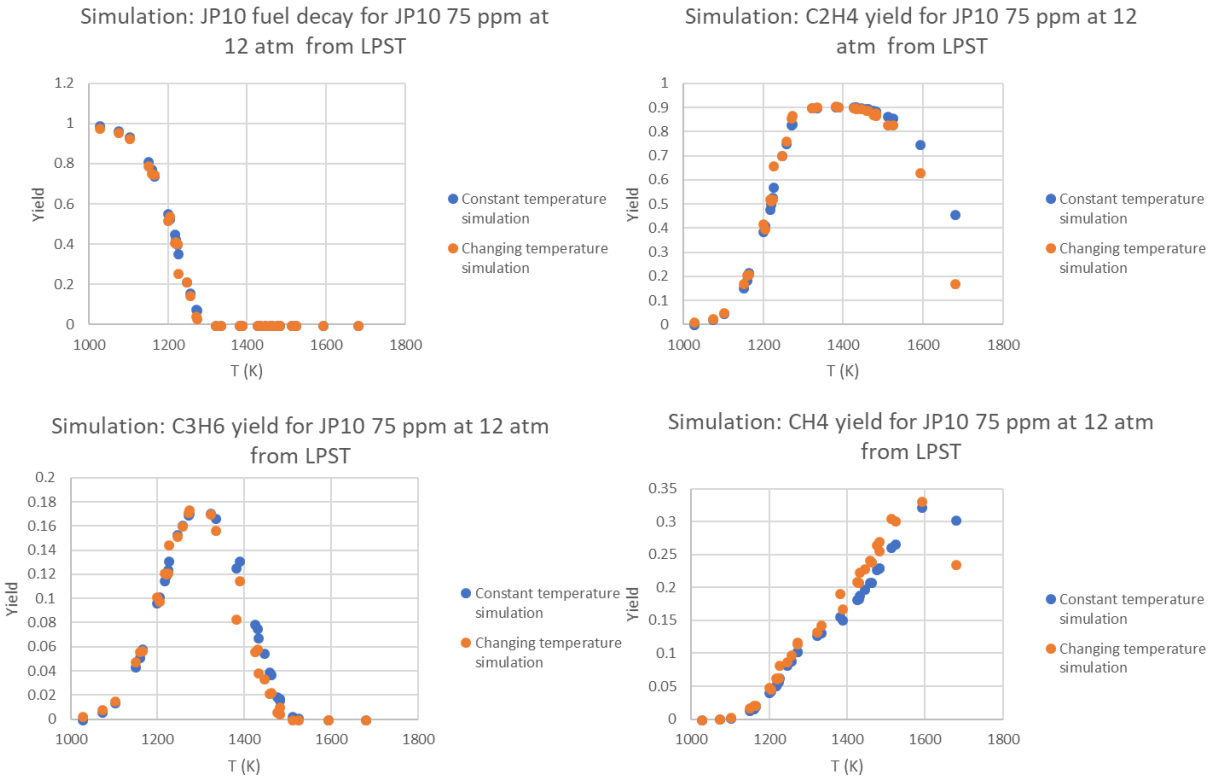

Figure 49: The comparisons between changing pressure simulation (orange dot) and constant pressure simulation (blue dot) for the experiment of JP10 75 ppm 12 atm in the LPST with 2.1 ms as the nominal reaction time.

6.3.6 FURTHER SUPPORT FOR THE CONSTANT PRESSURE APPROXIMATION

In addition to all the successful simulation comparisons from both the HPST and the LPST, there is an even more important implication arising from the simulations and experiments of JP10. Recall in Section 5.1, we compared the speciation data from two similar JP10 experiments which were conducted in different shock tubes, the HPST and the LPST, as shown in Figure 28. The comparison showed that the experiments matched very well for all species. We also just showed that the JP10 experiments in LPST at similar conditions, due to their close-to-flat pressure profiles, are close to constant pressure processes, unlike those from the HPST. Therefore, the very good match between the two experiments of JP10 with similar experimental conditions (72-75 ppm, 12-25 atm), but with largely different level of pressure attenuation (HPST high, LPST low), can be considered as an experimental validation that the changing pressure simulation can indeed be approximated as a constant pressure one.

Another important study supporting the approximation of changing pressure process by a constant one is the HyChem model theory with its two main assumptions. First, the fuel pyrolysis and the oxidation of the pyrolysis products are decoupled in practical combustion processes. This indicates less interference between the reactions from the two submodels. Second, the complex fuel pyrolysis process can be approximated by a small number of parallel reactions, e.g. reactions R1-R4, with a limited number of small products. This makes the lower temperature simulation of fuel pyrolysis resemble a single reaction model, which is previously suggested to be robust in constant pressure approximations in Section 6.3.2, and also observed in the simulation results in Figure 44 and Figure 46. These assumptions greatly reduced the complexity of the reaction process. The only difference in a new fuel's model will be the lumped reactions of fuel pyrolysis, while the foundational chemistry is intact. The fuel pyrolysis lumped reactions, which dominate the lower

temperature region, should in most cases work well with the constant pressure approach. If enough experience and study show the foundational chemistry part works satisfactorily with the constant pressure approximation for shock tube speciation studies, then it should be reasonable to believe that the combination of the two highly decoupled submodels will also work well enough when applied to new fuels.

Up to this point, we do have great support for simulations using the constant pressure condition to approximate the changing pressure condition that resembles what happens in real shock tube experiments. This in turn supports using chemical thermometers to obtain the v-T relation curve for the calibration temperature in a shock tube and applying the curve to other experiments. An additional remark is that these approaches are better suited when the shocks are fired in a very repeatable and consistent way in all experiments in a shock tube.

6.4 UNCERTAINTY CHARACTERIZATION

As we mentioned before, uncertainty characterization has been increasingly important in the chemical kinetic community. It helps a modeler understand the experiments better and also helps an experimentalist understand why a model built upon another experimental group's work shows discrepancies will his/her data. We herein lay out some details of our latest efforts to evaluate the uncertainties of our experimental data.

6.4.1 TEMPERATURE EVALUATION AND ITS UNCERTAINTY

The temperature of a shock experiment is mapped by a v-T curve. The end wall velocity is typically extrapolated linearly through a set of velocities along the axial direction of the shock tube. This set of velocities is calculated from the neighboring arrival times of the incident shock wave detected as a pressure increase by the side wall pressure transducers. Using *t*-statistics and Eq (3.28-3.29), the 95% uncertainty bound can be calculated, as shown in Figure 50 below.

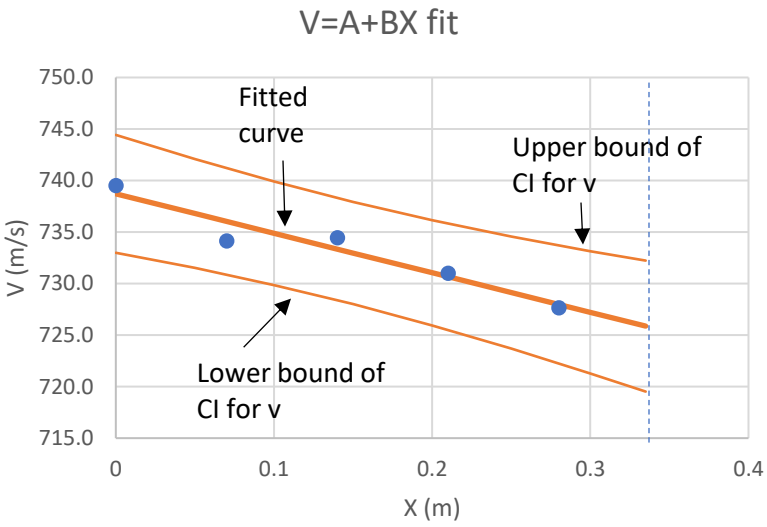

Figure 50: Illustration of the uncertainties of the end wall velocity value through the extrapolation of the 5 velocities. The data is from a shock in the LPST. CI means the 95% confidence interval.

The resulting velocity uncertainty at the end wall in the above seemingly good velocity profile actually gives about ±6.3 m/s 2σ uncertainty in velocity (we call the uncertainty representing 95% confidence bound as 2σ uncertainty) at the end wall. This is a very large uncertainty that will convert to around ±20 K 2σ uncertainty in temperature at the end wall. There are shocks that have less smooth velocity profile and can reach ±30 K or even higher uncertainties.

That temperature uncertainty may be an overestimation due to method of evaluating the uncertainties in the end wall velocity. We can actually reduce the uncertainty of the velocity calculation at the end wall by using the raw arrival time data. The methods for doing so are given in the following.

Calculation of the uncertainty of the end-wall shock arrival time

Arrival times at the 6 side-wall pressure transducers are used to predict the velocity v and uncertainty of it at the end wall. Assume, as experimental evidence has previously shown, the velocity linearly decreases as a function of distance x, and that for the first transducer that detects the shock wave, the distance $x = 0$. Since it is the time relative to the first transducer that matters, we can let the time $t = 0$ at $x = 0$. Table 2 is a set of arrival times and their corresponding distances used for calculating the velocity of a sample shock, assuming t=0 at the time of the shock arrival at the first transducer. The end wall is at $x = 0.37\ m$.

Table 2 Reading of arrival time from transducers.

Arrival time	t_0^*	t_1^*	t_2^*	t_3^*	t_4^*	t_5^*
Transducer reading	0.000818	0.000912	0.001007	0.001102	0.001197	0.001295
Converted Value	0	0.000094	0.000189	0.000284	0.000379	0.000477
Distance x (m)	0	0.07	0.14	0.21	0.28	0.35

Then we get the below equations.

$$\frac{dx}{dt} = ax + b \qquad (6.9)$$

With condition $t = 0$ at $x = 0$, we can get

$$=> \quad t = \frac{\ln(\frac{ax+b}{b})}{a} \qquad (6.10)$$

We use $t_i,\ i = 1,2,3,4,5$ that corresponds to the arrival times at each of the 5 transducers after the first transducer, respectively. The distance x from the first transducer of these five transducers is 0.07, 0.14, 0.21, 0.28, 0.35, in meters, respectively. We can get the parameters a and b by finding the best fit of Eq (6.10) for the five measured points of (x, t), as shown in Figure 51. This calculation is done by a solver in Excel or computer by searching for the optimal value of *a* and *b*. Once we have a and b calculated, from Eq (6.10) we can get t at $x = 0.37$, which is the end wall shock arrival time, and also get its variance and 95% confidence interval (CI) from Equation (3.29) based on *t*-statistics, see Figure 51 and Figure 52. Both t and its CI are used later in the calculation of the CI of the velocity. With Eq (6.9), we can directly get the end wall velocity $v = \frac{dx}{dt} = a * 0.37 + b$.

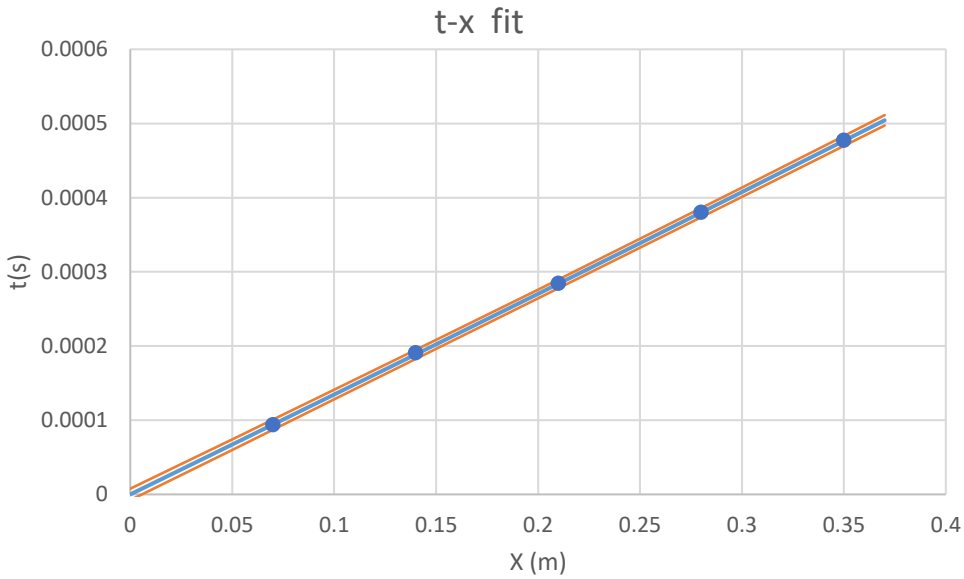

Figure 51: Fitted curve of Equation (6.9) to five (*x*, *t*) points (blue dotted line) and the 95% confidence interval (orange band).

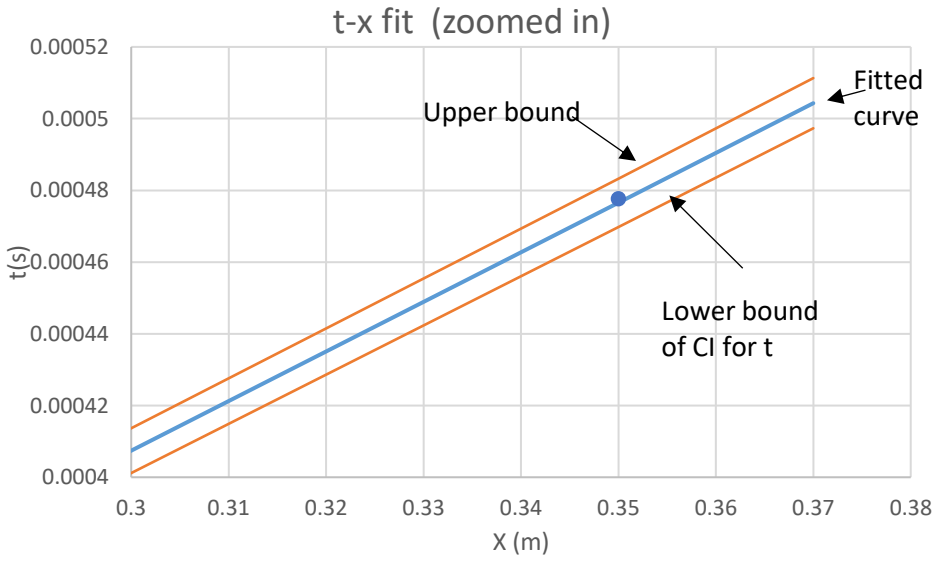

Figure 52: Expanded view of the curve fit between points 4 and 5 (blue dot) of Figure 51, as well as the arrival-time extrapolation to the end wall (solid blue line) and the upper and lower uncertainty bounds of arrival time (orange lines).

The uncertainty level of the arrival times derived from the above method can potentially be underestimated, due to not including the uncertainty associated with having only 3 significant digits here recorded for arrival time at the transducers. In recent experiments, we improved the precision level of transducer readings, so let's neglect that uncertainty factor at this point. Next, we need to convert the uncertainty in arrival time *t* to uncertainty in velocity *v*, and thus temperature *T*.

Temperature uncertainty

Given the arrival time CI (t_l, t_u), we can get the velocity CI $(v - \Delta v_l, v + \Delta v_u)$, where

$$\Delta v_l \approx \frac{x_{endwall}}{t} - \frac{x_{endwall}}{t_u} \qquad (6.11)$$

$$\Delta v_u \approx \frac{x_{endwall}}{t_l} - \frac{x_{endwall}}{t} \qquad (6.12)$$

Δv_l is the difference between the results using t and t_u in calculating the average velocity over the distance from $x = 0$ to end wall, and Δv_u is that for using t and t_l. The subscripts $_u$ and $_l$ refer to upper and lower respectively. These two values, Δv_l and Δv_u are imposed on the end wall velocity to give an estimate of the velocity CI at end wall. This method is an approximation based on that the velocity uncertainty being approximately constant along the distance, although it is slightly

larger at the two ends ($x = 0$ and $x = 0.37$). The mathematical justification of this approximation can be found in Appendix F.

After the CI for the velocity at end wall is obtained, the shock temperature and temperature CI due to velocity can be obtained by using the ideal shock relations of the specific gas mixture by calculating the corresponding temperatures of the velocities on the CI bounds. The FROSH code needs to be utilized to calculate the temperature and temperature CI bounds from the velocity CI bounds when the fuel fraction of the test gas is high (>200 ppm).

Another two sources of temperature uncertainty are the uncertainty of initial fuel fraction for concentrated fuel/argon mixtures and that of the pre-shock temperature. For the former one, the initial fuel mole fraction CI is input to the FROSH code with the velocity as the average velocity of each shock to get the CI of temperature. We found that the former will only add a negligible difference (~1 K) to the total CI of temperature even for our highest fuel fraction 6356 ppm of Jet A at shock temperature less than 1500K when using FROSH, while at above 1500K, it is approximately 2-4 K. For the pre-shock test gas temperature effect, it is calculated that the shock temperature is insensitive to it. Even a 20 K difference in initial test gas temperature will result in only about 7 K difference in the shock temperature.

Overall, we have a much improved understanding of our temperature evaluation and uncertainty. A more complete investigation on all the potential cause of uncertainties and how to reduce them is suggested as future work.

6.4.2 COMPARISON OF NEW TEMPERATURE TO OLD TEMPERATURE

Now we have a new temperature from t-x fit for each shock with lower uncertainty than that obtained from the typical t-v fit. The new temperature will be in average about 6 K higher than the old one. However, occasionally, a shock will even result in a 20 K higher temperature evaluation. The effect of the two temperature determinations is shown in a comparison plot for the ethylene profile from the LPST below in Figure 54.

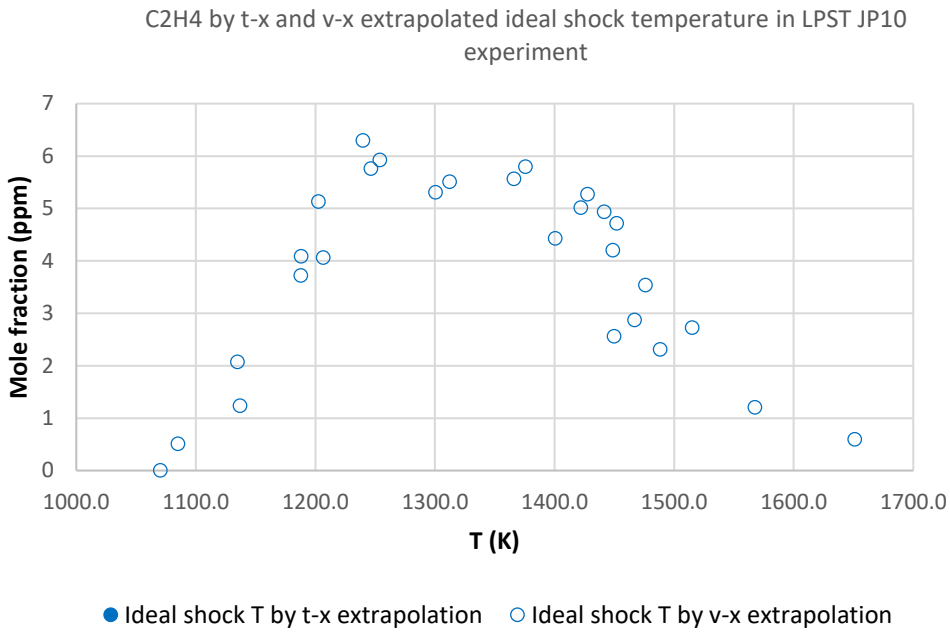

Figure 53: Comparison of the shock temperature values between from t-x extrapolation (filled circle) and v-x extrapolation (hollow circle) on the C_2H_4 profile from the LPST JP10 75 ppm 25 atm experiments.

The change is very small, and thus does not change any qualitative conclusions from our data. We adopted the temperature from arrival time extrapolation for all the Jet A and JP10 data in the LPST

plotted in this thesis, since we directly used the $T_5(0)$ as our shock temperatures in the LPST and the uncertainty of velocity is important in this case. However, we also included in Appendix B the velocity-extrapolated velocity for each LPST shock of Jet A and JP10, along with the t-extrapolated velocity reported in the plots and the uncertainties associated with them. The uncertainty in the HPST is more complicated, since it uses chemical thermometers. We reported the temperature from the temperature calibration curve and the velocity-extrapolated velocity for all data in the HPST reported in this thesis. The chemical thermometers data in the HPST is obtained using the velocity extrapolated velocity, too.

6.4.3 UNCERTAINTIES OF SPECIES YIELD

Given the carbon total determined from the amount of CO_2 which is used to get the fuel input, the variance of the mole fraction of species A, the yield of species A can be obtained. We normalize all species fraction variables by their own mean values. Then each normalized variable of species has a mean of 1, so that we only need to use the percentage variance of each species (e.g. for species A, it's ±3%; for CO_2 it's ±2%). According to the formula for the variance of the product of independent variables in Eq (3.27), if we use percentage variance, the variance of species A's yield, $Var(y_A)^*$, can be expressed as [90]

$$Var(y_A)^* = 100\%\{[Var(x_A)^* + 1][Var(x_{CO2})^* + 1]\left[Var\left(x_{A,calib.gas}\right)^* + 1\right]\left[Var\left(x_{CO2,calib.gas}\right)^* + 1\right] - 1\} \quad (6.13)$$

Here, $Var(X)^*$ denotes the variance of X normalized to the mean square of X, which is $Var(X)^* = Var(X)/E(X)^2$. The variances of species calibration measurement x_A, CO_2 calibration measurement x_{CO2}, as well as that of species calibration gas mole fraction $x_{A,calib.gas}$ and CO_2 calibration gas mole fraction $x_{CO2,calib.gas}$, as specified by the manufacturer on the calibration gas cylinders, are all counted as independent contributors to the total variance, with all of them normalized to give a percentage uncertainty. We then get the 95% confidence interval by doubling of the square root of percentage variance $Var(y_A)^*$ – as is standard for a normal distribution.

Below is the result of our uncertainty analysis for one representative set of experiments compared with simulation results, with error bars representing the 95% confidence interval.

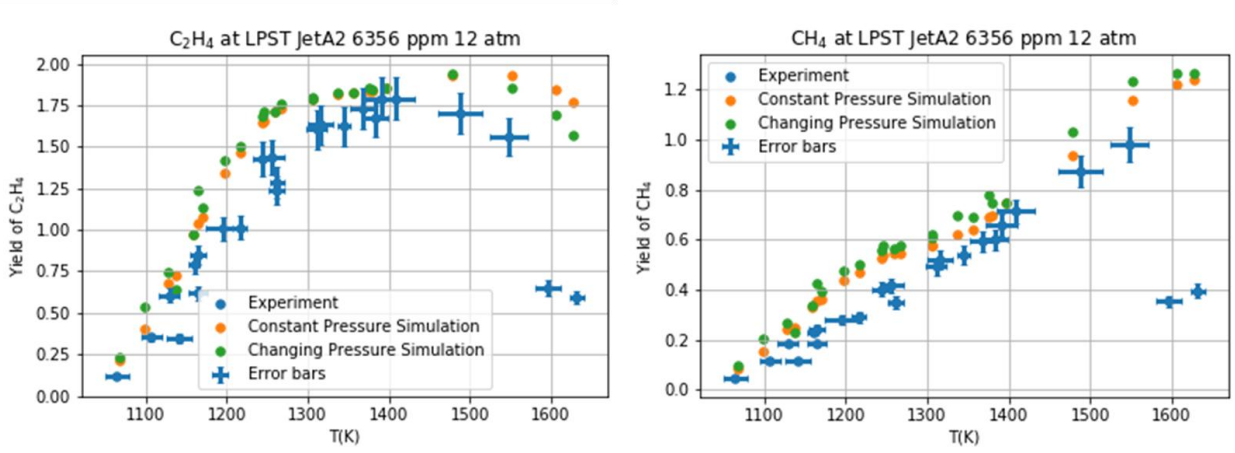

Figure 54: Illustration of the uncertainty plots. Comparison of species yield between experimental data (blue dots with error bars) and two types of simulations (orange for constant pressure and green for changing pressure) from the HyChem model in the case of LPST Jet A 6356 ppm 12 atm. Nominal reaction time is 2.1 ms. Selected species are ethylene (left) and methane (right).

As one can see, the simulation results are close to the experiments for Jet A in the LPST, although the simulation results still do not lie in the confidence interval of our experiments for certain temperature regions.

6.5 BEHAVIOR OF THE REFLECTED SHOCKS IN THE LPST

The behavior of the reflected shocks can reveal how close the shocks are to the ideal case. Lifshitz in [90] even used the reflected shock wave velocity to derive the temperature. Therefore, we examined the reflected shock behavior in our LPST to understand how close our shock temperature $T_5(0)$ can be evaluated by the ideal shock relation given by Eq (2.6). We extracted the reflected shock information from the side wall pressure transducers from a batch of 314 shocks from the past experiments at 4 atm in the LPST, all of which were done on dilute test mixtures of fuel/Ar. For computational convenience, we extrapolated the end wall reflected shock velocity W_R using the v-x method mentioned above. Knowing the incident shock velocity W_S (thus Mach number) of each shock, we can use Eq (2.3) and Eq (2.8) to obtain a predicted reflected shock velocity W_R^*. We then compared the difference between W_R and W_R^*. The difference is plotted against the incident velocity in Figure 55. The generation of velocities are automated by a computer code. It sometimes gives wrong estimations in the signal processing of pressure traces, possibly due to noise when it does, these outliers are removed.

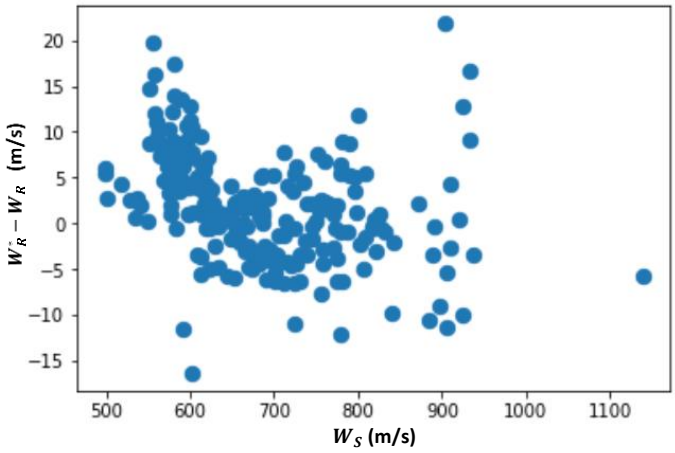

Figure 55: Distribution plot of difference between the measured reflected shock wave velocities and the predicted ones against the incident shock velocity in the LPST 4 atm experiments.

The resulting average value of $\Delta W_R = W_R^* - W_R$ is only 2.02 m/s, which means there is very little bias in the measured reflected shock velocity against our understanding of the ideal shock behavior in the LPST. The range of incident velocities of most interest for this study is between about 630 m/s to 850 m/s (1014 K to 1732 K). The discrepancies in this range of velocities are more concentrated around zero, mostly between -5 m/s to 5 m/s. This also shows that the reflected shocks behave satisfactorily well and are close to ideal in the LPST. There are many more interesting discoveries in our analysis of our massive data of recorded shock waves. Yet we only present a preliminary example of our latest work to understand our shock tube's behavior. There is much work to be done on this in the future in order to draw a more general conclusion.

In the future, we will perform the same analysis for the HPST, as well as shocks with concentrated fuel/Ar mixture reacting (which may induce significant effects on the reflected shock wave) in the LPST.

7 SUMMARY AND CONCLUSIONS

Shock tube experiments of the pyrolysis of two real fuels Jet A and JP10 have been done over a wide range of conditions regarding the fuel mole fraction (52 ppm to 6356 ppm), pressure (1 atm to 90 atm), and with different pressure attenuation rates in the HPST and the LPST. The temperature ranged from 800 K to 2200 K. Speciation data were obtained for the major products by GC-FID and GC-MS. The major species for the pyrolysis of both fuels are C1 to C4 hydrocarbons, cyclopentadiene, benzene, toluene, 1,3,5-hexatriyne, and, in the case of JP10, pentene. The carbon total profiles support the assumption that the pyrolysis of the real fuel can be approximated by fuel breaking down into a limited number of small stable species that have well known chemistry. This assumption is what the HyChem model is based upon. Jet A fuel produces significant amounts of C_2H_4, CH_4, and C_3H_6, while JP10 not only produces large amounts of C_2H_4 and CH_4, but also produced significant amounts of cyclopentadiene and benzene. For both fuels, the speciation data shows very little pressure dependence (with the same mole fraction of fuel) with a dilute test gas at between 25 atm to 90 atm from the HPST. The Jet A fuel experiments with high fuel content at lower pressure (1 atm – 12 atm) in the LPST showed significant difference in the formation of some species, such as C_2H_6 and aC_3H_4. Significant pressure and fuel concentration dependence is observed in these Jet A experiments. The LPST JP10 experiments with 75 ppm at 12 atm produced very close speciation profile with that from the HPST JP10 72 ppm 25 atm experiments for all species measured.

The speciation data is compared with the HyChem model for both Jet A and JP10. The Jet A model predicts the experimental data satisfactorily considering the different thermodynamic condition in the experiments upon which the model was fit. The model predicts a faster decomposition rate of

the fuel and faster rise of C_2H_4 in the low temperature region below 1400 K. Monte Carlo analysis on the rate parameters of the *A* factor and activation energy E_a are done separately, as a sensitivity analysis for the Jet A model. The model shows different sensitivities to *A* and E_a with respect to temperature. Additionally, the fuel pyrolysis submodel and the foundational chemistry submodel were studied separately in the Monte Carlo analysis. The low temperature region is dominated by the fuel pyrolysis submodel, while the high temperature region is dominated by the foundational chemistry one. A potential reason for the model-experiment discrepancies in Jet A study may be due to the model assuming that the multicomponent jet fuel follows a single lumped fuel pyrolysis reaction with coefficients not changing over the reaction time or with temperature. The comparison between the 2nd Generation surrogate model for Jet A and the HyChem model suggests that the surrogate model more closely simulates the experimental results, though with much higher computational costs. The JP10 HyChem model predicts our experiments very well for most important species, much better than the case for Jet A. This result demonstrate that the HyChem approach can be well applied to model single component fuels as well.

Besides the fuel studies, a thorough discussion about the temperature characterization and measurement is presented. The method of temperature calibration by chemical thermometers, which has received some skepticism, is revisited. Chemical responses from changing pressure processes were studied starting from single reaction models and later extended to complex reaction networks. We demonstrated that the constant pressure simulations can reproduce the changing pressure simulations well enough to be used routinely for analysis in both of our shock tubes for most species. The support for this conclusion come from mathematical reasoning, simulation comparisons, the HyChem model assumptions, as well as the experiments of JP10 that reproduce each other under different pressure attenuation rates. Some theoretical aspects for the constant

pressure approximation were also discussed along with the chemical thermometer methodology. The validity of the constant pressure simulation also justifies the conventional approach of chemical thermometers. Although a better knowledge of the rate constants of TFE is still needed, the chemical thermometer approach can generally be safely used in dilute shock tube experiments that use GC as the analytical instrument, as long as the rate parameters used in the experiments are reported.

The temperature uncertainty characterization was described in a detailed manner, at the same time introducing a new approach for calculating the end wall velocities directly by a nonlinear fit of shock arrival times, which has less uncertainties than the velocity-extrapolated ones. Species uncertainty and temperature uncertainty were displayed together in plots. As one of the other efforts for advancing our understanding of the shock wave temperatures in experiments, the reflected shock wave velocity analysis was introduced and showed good consistency with the expected behavior of the shock wave in the ideal situation.

Overall, the shock tube experiments of real jet fuels were successful. The HyChem model performed well. The large cooperative work has shown great values in inter-laboratory discussions. We gained deep understanding of and more confidence in our temperature characterization methods.

8 PAST WORK ON THE EFFECT OF GRAPHENE AEROSOL ON COMBUSTION

Before the work on the shock tube study, I was working on a project aimed at discovering the effect of aerosols of graphene-derived nano-particulates on combustion. The work was very exploratory. Two flow reactors were set up along with a self-assembled electrospray atomization apparatus and an ionizer that eliminates electrostatic charges in the particles. Flames were ignited by spark ignitors in the flow reactor. The nanoparticles were synthesized. They included graphene oxide, nitrogen-doped graphene quantum dots, and pristine graphene. The nanoparticles were dispersed into the liquid fuels (ethanol, heptane) or water by a variety of methods, taking up to 0.5% of the fuel mass. The colloidal mixture is aerosolized by electrospray atomizer and, in some experiments, ultrasonic nebulizer. The fuels (ethanol, heptane, and CH_4) were either injected along with the nanoparticles through the atomizer or separately and later mixed with air in the vapor phase at different equivalence ratios. The nanoparticles were confirmed to have been successfully transported to the reactors in the gas phase. The only evident effect of the nanoparticles we observed is that, they tend to suppress the ignition of the fuel/air mixture. This is probably due to the radical scavenging of the graphene nanoparticles. The project was initially aimed at knowing well if there are catalytic effects from graphene nanoparticles that will boost combustion. The outcome from experiments seems to be quite the contrary. Anyway, the project has ended with no further pursuit of its goals. I hope this will bring some inspirations for relevant researches, for example, studying the effect of the high concentration of soot or industrial dust on combustion.

9 FUTURE WORK

Some of the future work has already been suggested in the previous chapters. For future work,

1) Further investigate the chemistry of the jet fuels under oxidation conditions and validate the experiments against the HyChem model.

2) Perform the experiments using GC×GC TOFMS to obtain a detailed speciation data of the multicomponent jet fuels' pyrolysis or oxidation in the shock tube. This can also assess the component-wise fuel loss while injecting the test gas into the shock tube.

3) Develop a Jet A model that is able to better describe the fuel decomposition. We probably need to think out of the framework of the HyChem model, but still use some similar approaches.

4) Further our investigation into the behaviors of the shock waves, especially on the temperature responses in the two shock tubes.

5) Improve our measure precision. Understand the cause of the scattering in speciation data and try to reduce scattering. Find potential bias in measurements and remove them.

6) Upgrade the Monte Carlo analysis with more details about the uncertainties of each rate parameter and their covariances. The *n* factor will also be studied.

REFERENCES

[1] T. Edwards, L.Q. Maurice, Surrogate Mixtures to Represent Complex Aviation and Rocket Fuels, *J. Propuls. Power*. 17 (2001) 461–466. doi:10.2514/2.5765.

[2] T. Malewicki, S. Gudiyella, K. Brezinsky, Experimental and modeling study on the oxidation of Jet A and the n-dodecane/iso-octane/n-propylbenzene/1,3,5-trimethylbenzene surrogate fuel, *Combust. Flame*. 160 (2013) 17–30. doi:10.1016/j.combustflame.2012.09.013.

[3] S. Dooley, S.H. Won, J. Heyne, T.I. Farouk, Y. Ju, F.L. Dryer, K. Kumar, X. Hui, C.J. Sung, H. Wang, M.A. Oehlschlaeger, V. Iyer, S. Iyer, T.A. Litzinger, R.J. Santoro, T. Malewicki, K. Brezinsky, The experimental evaluation of a methodology for surrogate fuel formulation to emulate gas phase combustion kinetic phenomena, *Combust. Flame*. 159 (2012) 1444–1466. doi:10.1016/j.combustflame.2011.11.002.

[4] T. Edwards, M. Colket, N. Cernansky, F. Dryer, F. Egolfopoulos, D. Friend, E. Law, D. Lenhert, P. Lindstedt, H. Pitsch, A. Sarofim, K. Seshadri, M. Smooke, W. Tsang, S. Williams, Development of an Experimental Database and Kinetic Models for Surrogate Jet Fuels, in: 45th AIAA Aerosp. Sci. Meet. Exhib., 2007. doi:10.2514/6.2007-770.

[5] P. Dagaut, A. El Bakali, A. Ristori, The combustion of kerosene: Experimental results and kinetic modelling using 1- to 3-component surrogate model fuels, *Fuel*. 85 (2006) 944–956. doi:10.1016/j.fuel.2005.10.008.

[6] S. Dooley, S.H. Won, S. Jahangirian, Y. Ju, F.L. Dryer, H. Wang, M.A. Oehlschlaeger, The combustion kinetics of a synthetic paraffinic jet aviation fuel and a fundamentally

formulated, experimentally validated surrogate fuel, *Combust. Flame*. 159 (2012) 3014–3020. doi:10.1016/j.combustflame.2012.04.010.

[7] A. Violi, S. Yan, E.G. Eddings, A.F. Sarofim, S. Granata, T. Faravelli, E. Ranzi, Experimental formulation and kinetic model for JP-8 surrogate mixtures, *Combust. Sci. Technol.* 174 (2002) 399–417. doi:10.1080/00102200215080.

[8] E.G. Eddings, S. Yan, W. Ciro, A.F. Sarofim, Formulation of a surrogate for the simulation of Jet fuel pool fires, *Combust. Sci. Technol.* 177 (2005) 715–739. doi:10.1080/00102200590917248.

[9] H.R. Zhang, E.G. Eddings, A.F. Sarofim, Criteria for selection of components for surrogates of natural gas and transportation fuels, *Proc. Combust. Inst.* 31 I (2007) 401–409. doi:10.1016/j.proci.2006.08.001.

[10] M. Colket, T. Edwards, S. Williams, N.P. Cernansky, D.L. Miller, F. Egolfopoulos, F.L. Dryer, J. Bellan, P. Lindstedt, K. Seshadri, H. Pitsch, A. Sarofim, M. Smooke, W. Tsang, Identification of target validation data for development of surrogate jet fuels, *46th AIAA Aerosp. Sci. Meet. Exhib.* (2008) 92407.

[11] P.N. Rao, D. Kunzru, Thermal cracking of JP-10 : Kinetics and product distribution, 76 (2006) 154–160. doi:10.1016/j.jaap.2005.10.003.

[12] S. Nakra, R.J. Green, S.L. Anderson, Thermal decomposition of JP-10 studied by micro-flowtube pyrolysis-mass spectrometry, 144 (2006) 662–674. doi:10.1016/j.combustflame.2005.08.035.

[13] C.W. Gao, A.G. Vandeputte, N.W. Yee, W.H. Green, R.E. Bonomi, G.R. Magoon, H.

Wong, O.O. Oluwole, D.K. Lewis, N.M. Vandewiele, K.M. Van Geem, JP-10 combustion studied with shock tube experiments and modeled with automatic reaction mechanism generation, *Combust. Flame*. 162 (2015) 3115–3129. doi:10.1016/j.combustflame.2015.02.010.

[14] N.M. Vandewiele, G.R. Magoon, K.M. Van Geem, W.H. Green, G.B. Marin, Experimental and Modeling Study on the Thermal Decomposition of Jet Propellant-10, (2014).

[15] N.M. Vandewiele, G.R. Magoon, K.M. Van Geem, W.H. Green, G.B. Marin, Kinetic Modeling of Jet Propellant-10 Pyrolysis, (2015). doi:10.1021/ef502274r.

[16] N.M. Vandewiele, G.R. Magoon, M. Eestermans, K.M. Van Geem, M. Reyniers, W.H. Green, B. Guy, Thermal decomposition of JP-10 : Experimental and modeling study fuel, (n.d.).

[17] G.R. Magoon, W.H. Green, O.O. Oluwole, H. Wong, S.E. Albo, D.K. Lewis, M.W. Kelly, N. London, Updating Our Understanding of JP-10 Decomposition Chemistry : Using RMG – an Automatic Reaction Mechanism Generator, (2010) 1–17.

[18] D.J. Luning Prak, M.H. Jones, P. Trulove, A.M. McDaniel, T. Dickerson, J.S. Cowart, Physical and chemical analysis of alcohol-to-jet (ATJ) fuel and development of surrogate fuel mixtures, *Energy and Fuels*. 29 (2015) 3760–3769. doi:10.1021/acs.energyfuels.5b00668.

[19] S. Gudiyella, T. Malewicki, A. Comandini, K. Brezinsky, High pressure study of m-xylene oxidation, *Combust. Flame*. 158 (2011) 687–704. doi:10.1016/j.combustflame.2010.12.012.

[20] S. Gudiyella, K. Brezinsky, High pressure study of 1,3,5-trimethylbenzene oxidation, *Combust. Flame*. 159 (2012) 3264–3285. doi:10.1016/j.combustflame.2012.06.014.

[21] T. Malewicki, K. Brezinsky, Experimental and modeling study on the pyrolysis and oxidation of n-decane and n-dodecane, *Proc. Combust. Inst.* 34 (2013) 361–368. doi:10.1016/j.proci.2012.06.156.

[22] S. Banerjee, R. Tangko, D.A. Sheen, H. Wang, C.T. Bowman, An experimental and kinetic modeling study of n-dodecane pyrolysis and oxidation, *Combust. Flame*. 163 (2016) 12–30. doi:10.1016/j.combustflame.2015.08.005.

[23] S. Gudiyella, K. Brezinsky, High pressure study of n-propylbenzene oxidation, *Combust. Flame*. 159 (2012) 940–958. doi:10.1016/j.combustflame.2011.09.013.

[24] D.R. Haylett, D.F. Davidson, R.D. Cook, Z. Hong, W. Ren, S.H. Pyun, R.K. Hanson, Multi-species time-history measurements during n-hexadecane oxidation behind reflected shock waves, *Proc. Combust. Inst.* 34 (2013) 369–376. doi:10.1016/j.proci.2012.06.014.

[25] H. Wang, R. Xu, K. Wang, C.T. Bowman, R.K. Hanson, D.F. Davidson, K. Brezinsky, F.N. Egolfopoulos, A physics-based approach to modeling real-fuel combustion chemistry - I. Evidence from experiments, and thermodynamic, chemical kinetic and statistical considerations, *Combust. Flame*. (2018). doi:10.1016/j.combustflame.2018.03.019.

[26] D.A. Sheen, H. Wang, Combustion kinetic modeling using multispecies time histories in shock-tube oxidation of heptane, *Combust. Flame*. 158 (2011) 645–656. doi:10.1016/j.combustflame.2010.12.016.

[27] R. Xu, K. Wang, S. Banerjee, J. Shao, T. Parise, Y. Zhu, S. Wang, A. Movaghar, D.J. Lee,

R. Zhao, X. Han, Y. Gao, T. Lu, K. Brezinsky, F.N. Egolfopoulos, D.F. Davidson, R.K. Hanson, C.T. Bowman, H. Wang, A physics-based approach to modeling real-fuel combustion chemistry – II. Reaction kinetic models of jet and rocket fuels, *Combust. Flame*. (2018). doi:10.1016/j.combustflame.2018.03.021.

[28] E. Ranzi, M. Dente, A. Goldaniga, G. Bozzano, T. Faravelli, Lumping procedures in detailed kinetic modeling of gasification, pyrolysis, partial oxidation and combustion of hydrocarbon mixtures, *Prog. Energy Combust. Sci.* 27 (2001) 99–139. doi:10.1016/S0360-1285(00)00013-7.

[29] Y. Gao, R. Shan, S. Lyra, C. Li, H. Wang, J.H. Chen, T. Lu, On lumped-reduced reaction model for combustion of liquid fuels, *Combust. Flame*. 163 (2016) 437–446. doi:10.1016/j.combustflame.2015.10.018.

[30] Y. Han, A.M. Elbaz, W.L. Roberts, H.G. Im, New Procedure to Develop Lumped Kinetic Models for Heavy Fuel Oil Combustion, *Energy and Fuels*. 30 (2016) 9814–9818. doi:10.1021/acs.energyfuels.6b01685.

[31] R.S. Tranter, K. Brezinsky, D. Fulle, Design of a high-pressure single pulse shock tube for chemical kinetic investigations, *Rev. Sci. Instrum.* 72 (2001) 3046–3054. doi:10.1063/1.1379963.

[32] Kenneth Brezinsky: High Pressure Shock Tube Laboratory, https://kenbrez.lab.uic.edu/, (n.d.). https://kenbrez.lab.uic.edu/.

[33] R.S. Tranter, R. Sivaramakrishnan, K. Brezinsky, M.D. Allendorf, High pressure, high temperature shock tube studies of ethane pyrolysis and oxidation, *Phys. Chem. Chem. Phys.* 4 (2002) 2001–2010. doi:10.1039/b110702j.

[34] D.F. Davidson, Y. Zhu, J. Shao, R.K. Hanson, Ignition delay time correlations for distillate fuels, *Fuel*. 187 (2017) 26–32. doi:10.1016/j.fuel.2016.09.047.

[35] C.C. Schmidt, C.T. Bowman, Flow reactor study of the effect of pressure on the thermal de-NOx process, *Combust. Flame*. 127 (2001) 1958–1970. doi:https://doi.org/10.1016/S0010-2180(01)00300-5.

[36] Y.L. Wang, C. Ji, A.T. Holley, F.N. Egolfopoulos, T.T. Tsotsis, H.J. Curran, Propagation and extinction of premixed dimethyl-ether/air flames, *West. States Sect. Inst. Spring Meet. 2008*. 32 (2008) 1035–1042. doi:10.1016/j.proci.2008.06.054.

[37] Y. Gao, T. Lu, Reduced HyChem Models for Jet Fuel Combustion, *10th U.S. Natl. Combust. Meet.* (2017) 1–10.

[38] M. Colket, J. Heyne, M. Rumizen, M. Gupta, T. Edwards, W.M. Roquemore, G. Andac, R. Boehm, J. Lovett, R. Williams, J. Condevaux, D. Turner, N. Rizk, J. Tishkoff, C. Li, J. Moder, D. Friend, V. Sankaran, Overview of the National Jet Fuels Combustion Program, *AIAA J*. 55 (2017) 1087–1104. doi:10.2514/1.J055361.

[39] J.S. Chickos, H. Zhao, Measurement of the Vaporization Enthalpy of Complex Mixtures by Correlation-Gas Chromatography. The Vaporization Enthalpy of RP-1, JP-7, and JP-8 Rocket and Jet Fuels at T = 298.15 K, *Energy & Fuels*. 19 (2005) 2064–2073. doi:10.1021/ef050116m.

[40] HyChem, Combustion Reaction Models of Liquid Fuels, (n.d.). https://web.stanford.edu/group/haiwanglab/HyChem/index.html.

[41] H. Wang, X. You, A. V. Joshi, A.L. S. G. Davis, F. Egolfopoulos, C.K. Law, USC Mech

Version II. High-temperature combustion reaction model of H2/CO/C1-C4 compounds, (2007). http://ignis.usc.edu/%0AUSC_Mech_II.htm.

[42] The San Diego Mechanism, Chemical-kinetic mechanisms for combustion applications, (n.d.). http://web.eng.ucsd.edu/mae/groups/combustion/mechanism.html.

[43] Mechanisms - Combustion - Lawrence Livermore National Laboratory, (n.d.). https://combustion.llnl.gov/mechanisms.

[44] E. Ranzi, A. Frassoldati, R. Grana, A. Cuoci, T. Faravelli, A.P. Kelley, C.K. Law, Hierarchical and comparative kinetic modeling of laminar flame speeds of hydrocarbon and oxygenated fuels, *Prog. Energy Combust. Sci.* 38 (2012) 468–501. doi:10.1016/j.pecs.2012.03.004.

[45] A.M. Ferris, D.F. Davidson, R.K. Hanson, A combined laser absorption and gas chromatography sampling diagnostic for speciation in a shock tube, *Combust. Flame*. (n.d.). doi:https://doi.org/10.1016/j.combustflame.2018.04.032.

[46] R.S. Tranter, R. Sivaramakrishnan, N. Srinivasan, K. Brezinsky, Calibration of reaction temperatures in a very high pressure shock tube using chemical thermometers, *Int. J. Chem. Kinet.* 33 (2001) 722–731. doi:10.1002/kin.1069.

[47] P.T. Lynch, G. Wang, Chemical thermometry in miniature HRRST using 1,1,1-trifluoroethane dissociation, *Proc. Combust. Inst.* 36 (2017) 307–314. doi:https://doi.org/10.1016/j.proci.2016.05.057.

[48] B. Culbertson, K. Brezinsky, High-pressure shock tube studies on graphite oxidation reactions with carbon dioxide and water, *Proc. Combust. Inst.* 33 (2011) 1837–1842.

doi:10.1016/j.proci.2010.05.035.

[49] D.F. Davidson, D.R. Haylett, R.K. Hanson, Development of an aerosol shock tube for kinetic studies of low-vapor-pressure fuels, *Combust. Flame*. 155 (2008) 108–117. doi:https://doi.org/10.1016/j.combustflame.2008.01.006.

[50] D. Jackson, D. Davidson, R. Hanson, Application of an Aerosol Shock Tube for the Kinetic Studies of n-Dodecane/Nano-Aluminum Slurries, in: 44th AIAA/ASME/SAE/ASEE Jt. Propuls. Conf. Exhib., American Institute of Aeronautics and Astronautics, 2008. doi:doi:10.2514/6.2008-4767.

[51] P. Roth, The shock tube technique applied to study aerosol rate processes BT - Shock Waves, in: K. Takayama (Ed.), Springer Berlin Heidelberg, Berlin, Heidelberg, 1992: pp. 73–82.

[52] K.P.J. Reddy, M.S. Hegde, V. Jayaram, Material processing and surface reaction studies in free piston driven shock tube, *Shock Waves, Vol 1, Proc.* (2009) 35–42\r799.

[53] W. Bleakney, D.K. Weimer, C.H. Fletcher, The Shock Tube: A Facility for Investigations in Fluid Dynamics, *Rev. Sci. Instrum.* 20 (1949) 807–815. doi:10.1063/1.1741395.

[54] E.L. Resler, S. Lin, A. Kantrowitz, The Production of High Temperature Gases in Shock Tubes, *J. Appl. Phys.* 23 (1952) 1390–1399. doi:10.1063/1.1702080.

[55] D.K. Weimer, C.H. Fletcher, W. Bleakney, Transonic Flow in a Shock Tube, *J. Appl. Phys.* 20 (1949) 418. doi:10.1063/1.1698393.

[56] T. Suzuki, Y. Sakamura, O. Igra, T. Adachi, S. Kobayashi, A. Kotani, Y. Funawatashi, Shock tube study of particles' motion behind a planar shock wave, *Meas. Sci. Technol.* 16

(2005) 2431–2436. doi:10.1088/0957-0233/16/12/005.

[57] K.T. Hwang, J.H. Kim, Y.S. Lee, S.G. Kwon, J.H. Park, K.H. Song, A study on fracture phenomena of glass filled ceramics using shock tube, in: Materwiss. Werksttech., 2010: pp. 306–313. doi:10.1002/mawe.201000602.

[58] W. Bonfield, P.K. Datta, Impact fracture of compact bone in a shock tube, *J. Mater. Sci.* 9 (1974) 1609–1614. doi:10.1007/BF00540759.

[59] I.R.H. A.G. Gaydon, The Shock Wave in an Ideal Gas, in: Shock Tube High-Temperature Chem. Phys., Reinhold Pub. Corp., 1963.

[60] J.D. Anderson, Modern Compressible Flow: With Historical Perspective, 3rd ed., McGraw-Hill, 2002.

[61] M.F. Campell, Studies of Biodiesel Surrogates Using Novel Shock Tube Techniques, Stanford University, 2014.

[62] F. Nobuyuki, K. Mitsuo, A. Hiromitsu, A. Tetsuro, Evaluation of boundary-layer effects in shock-tube studies of chemical kinetics, *Int. J. Chem. Kinet.* 11 (2018) 285–304. doi:10.1002/kin.550110306.

[63] L. Davies, J.L. Wilson, Influence of Reflected Shock and Boundary-Layer Interaction on Shock-Tube Flows, *Phys. Fluids*. 12 (1969) I-37-I-43. doi:10.1063/1.1692625.

[64] E.L. Petersen, R.K. Hanson, Improved Turbulent Boundary-Layer Model for Shock Tubes, *AIAA J.* 41 (2003) 1314–1322. doi:10.2514/2.2076.

[65] E.L. Petersen, R.K. Hanson, Nonideal effects behind reflected shock waves in a high-pressure shock tube, *Shock Waves*. 10 (2001) 405–420. doi:10.1007/PL00004051.

[66] H. Mirels, Attenuation in a shock tube due to unsteady-boundary-layer action, Cleveland, OH, USA, 1957. https://ntrs.nasa.gov/archive/nasa/casi.ntrs.nasa.gov/19930092322.pdf.

[67] J.V. Michael, J.W. Sutherland, The thermodynamic state of the hot gas behind reflected shock waves: Implication to chemical kinetics, *Int. J. Chem. Kinet.* 18 (2018) 409–436. doi:10.1002/kin.550180402.

[68] A. Fridlyand, K. Brezinsky, A. Mandelbaum, N-Heptane Pyrolysis and Oxidation in Ethylene–Methane and Iso-Octane Mixtures, *J. Propuls. Power*. 29 (2013) 732–743. doi:10.2514/1.B34875.

[69] J.H. Kiefer, The Laser-Schlieren Technique in Shock Tube Kinetics, in: A. Lifshitz (Ed.), Shock Waves Chem., Marcel Dekker, 1981: p. 59.

[70] A. Fridlyand, P.T. Lynch, R.S. Tranter, K. Brezinsky, Single pulse shock tube study of allyl radical recombination, *J. Phys. Chem. A.* 117 (2013) 4762–4776. doi:10.1021/jp402391n.

[71] T. Malewicki, DEVELOPMENT OF A JET A CHEMICAL SURROGATE MODEL USING HIGH, University of Illinois at Chicago, 2012.

[72] A.R. Amadio, M.W. Crofton, E.L. Petersen, Test-time extension behind reflected shock waves using CO2-He and C3H8-He driver mixtures, *Shock Waves*. 16 (2006) 157–165. doi:10.1007/s00193-006-0058-6.

[73] W. Tang, K. Brezinsky, Chemical kinetic simulations behind reflected shock waves, *Int. J. Chem. Kinet.* 38 (2006) 75–97. doi:10.1002/kin.20134.

[74] A. Matsugi, K. Yasunaga, H. Shiina, Thermal Decomposition of 1,1,1-Trifluoroethane

Revisited, *J. Phys. Chem. A*. 118 (2014) 11688–11695. doi:10.1021/jp510227k.

[75] A. Matsugi, Dissociation of 1,1,1-Trifluoroethane Is an Intrinsic RRKM Process: Classical Trajectories and Successful Master Equation Modeling, *J. Phys. Chem. A*. 119 (2015) 1846–1858. doi:10.1021/acs.jpca.5b00796.

[76] A. Lifshitz, I. Shweky, J.H. Kiefer, S.S. Sidhu, Thermal isomerization of cyclopropanecarbonitrile. The use of two chemical thermometers in single pulse shock tube experiments, in: K. Takayama (Ed.), Proc. 18th Int. Symp. Shock Waves, Springer-Verlag, Berlin, 1992: pp. 825–830.

[77] A. Lifshitz, C. Tamburu, F. Dubnikova, Reactions of 1-naphthyl radicals with ethylene. Single pulse shock tube experiments, quantum chemical, transition state theory, and multiwell calculations, *J. Phys. Chem. A*. 112 (2008) 925–933. doi:10.1021/jp077289s.

[78] Y. Tao, R. Xu, K. Wang, J. Shao, S.E. Johnson, A. Movaghar, X. Han, J.-W. Park, T. Lu, K. Brezinsky, F.N. Egolfopoulos, D.F. Davidson, R.K. Hanson, C.T. Bowman, H. Wang, A Physics-based approach to modeling real-fuel combustion chemistry - III. Reaction kinetic model of JP10, *Combust. Flame*. Submitted (2018).

[79] CHEMKIN-PRO 15172, Reaction Design, (2016).

[80] A. Fridlyand, M.S. Johnson, S.S. Goldsborough, R.H. West, M.J. McNenly, M. Mehl, W.J. Pitz, The role of correlations in uncertainty quantification of transportation relevant fuel models, *Combust. Flame*. 180 (2017) 239–249. doi:10.1016/j.combustflame.2016.10.014.

[81] X. Han, M. Liszka, R. Xu, K. Brezinsky, H. Wang, A high pressure shock tube study of

the pyrolysis of real jet fuel Jet A, *Proc. Combust. Inst.* 37 (2018).

[82] J. Urzay, N. Kseib, D.F. Davidson, G. Iaccarino, R.K. Hanson, Uncertainty-quantification analysis of the effects of residual impurities on hydrogen-oxygen ignition in shock tubes, *Combust. Flame*. 161 (2014) 1–15. doi:10.1016/j.combustflame.2013.08.012.

[83] N. Kseib, J. Urzay, G. Iaccarino, Statistical inference of uncertainties in elementary reaction rates of chemical mechanisms, in: Cent. Turbul. Res. Annu. Res. Briefs 2011, 2011: pp. 161–168. https://web.stanford.edu/group/ctr/ResBriefs/2011/14_kseib.pdf.

[84] K. Pearson, Note on Regression and Inheritance in the Case of Two Parents, *Proc. R. Soc. London*. 58 (1895) 240–242. doi:10.1098/rspl.1895.0041.

[85] C. Spearman, The proof and measurement of association between two things. By C. Spearman, 1904., *Am. J. Psychol.* 100 (1987) 441–471. doi:10.2307/1422689.

[86] J.L. Myers, A.D. Well, Research Design and Statistical Analysis, 2003. http://books.google.co.uk/books?id=e2UyC4qTObAC.

[87] R. V Hogg, A.T. Craig, Introduction to Mathematical Statistics, 1995. doi:10.2307/1267313.

[88] R.H. Myers, S.L. Myers, Probability & Statistics for Engineers Scientists Probability & Statistics for Engineers & Scientists, 2007. doi:10.2307/2288012.

[89] Median filter - Wikipedia, (n.d.). https://en.wikipedia.org/wiki/Median_filter.

[90] T. Hastie, R. Tibshirani, J. Friedman, The Elements of Statistical Learning, *Elements*. 1 (2009) 337–387. doi:10.1007/b94608.

[91] R.S. Tranter, R. Sivaramakrishnan, N. Srinivasan, K. Brezinsky, Calibration of reaction

temperatures in a very high pressure shock tube using chemical thermometers, *Int. J. Chem. Kinet.* 33 (2001) 722–731. doi:10.1002/kin.1069.

[92] A. Matsugi, H. Shiina, Shock Tube Study on the Thermal Decomposition of Fluoroethane Using Infrared Laser Absorption Detection of Hydrogen Fluoride, *J. Phys. Chem. A.* 118 (2014) 6832–6837. doi:10.1021/jp5066709.

[93] B.R. Giri, R.S. Tranter, Dissociation of 1,1,1-trifluoroethane behind reflected shock waves: shock tube/time-of-flight mass spectrometry experiments, *J. Phys. Chem. A.* 111 (2007) 1585–1592. doi:10.1021/jp066232n.

[94] W. Tsang, A. Lifshitz, 1 , 1 , 1-Trifluoroethane, (1998).

[95] W. Tsang, C.M. Rosado-Reyes, Unimolecular Rate Expression for Cyclohexene Decomposition and Its Use in Chemical Thermometry under Shock Tube Conditions, *J. Phys. Chem. A.* 119 (2015) 7155–7162. doi:10.1021/jp509738r.

[96] B. Culbertson, K. Brezinsky, High-Pressure Shock Tube Studies on Carbon Oxidation Reactions with Carbon Dioxide and Water, *Energy & Fuels*. 23 (2009) 5806–5812. doi:10.1021/ef900641r.

[97] R.G. Gilbert, K. Luther, J. Troe, Theory of Thermal Unimolecular Reactions in the Fall-off Range. II. Weak Collision Rate Constants, *Berichte Der Bunsengesellschaft Für Phys. Chemie*. 87 (2018) 169–177. doi:10.1002/bbpc.19830870218.

[98] J.H. Kiefer, C. Katopodis, S. Santhanam, N.K. Srinivasan, R.S. Tranter, A Shock-Tube, Laser-Schlieren Study of the Dissociation of 1,1,1-Trifluoroethane: An Intrinsic Non-RRKM Process, *J. Phys. Chem. A.* 108 (2004) 2443–2450. doi:10.1021/jp036282h.

APPENDICES

APPENDIX A

LPST sample species calibrations in GC-FID are shown in Figure A1. Injection pressure is the pressure reading of the sampling line on the GC right before injection to the GC. The response factor is the ratio between the ppm value of the species mole fraction and the GC area reading normalized by injection pressure in psi. The linear fit is used to assign response factor for sampling in shock experiments based on the injection pressure.

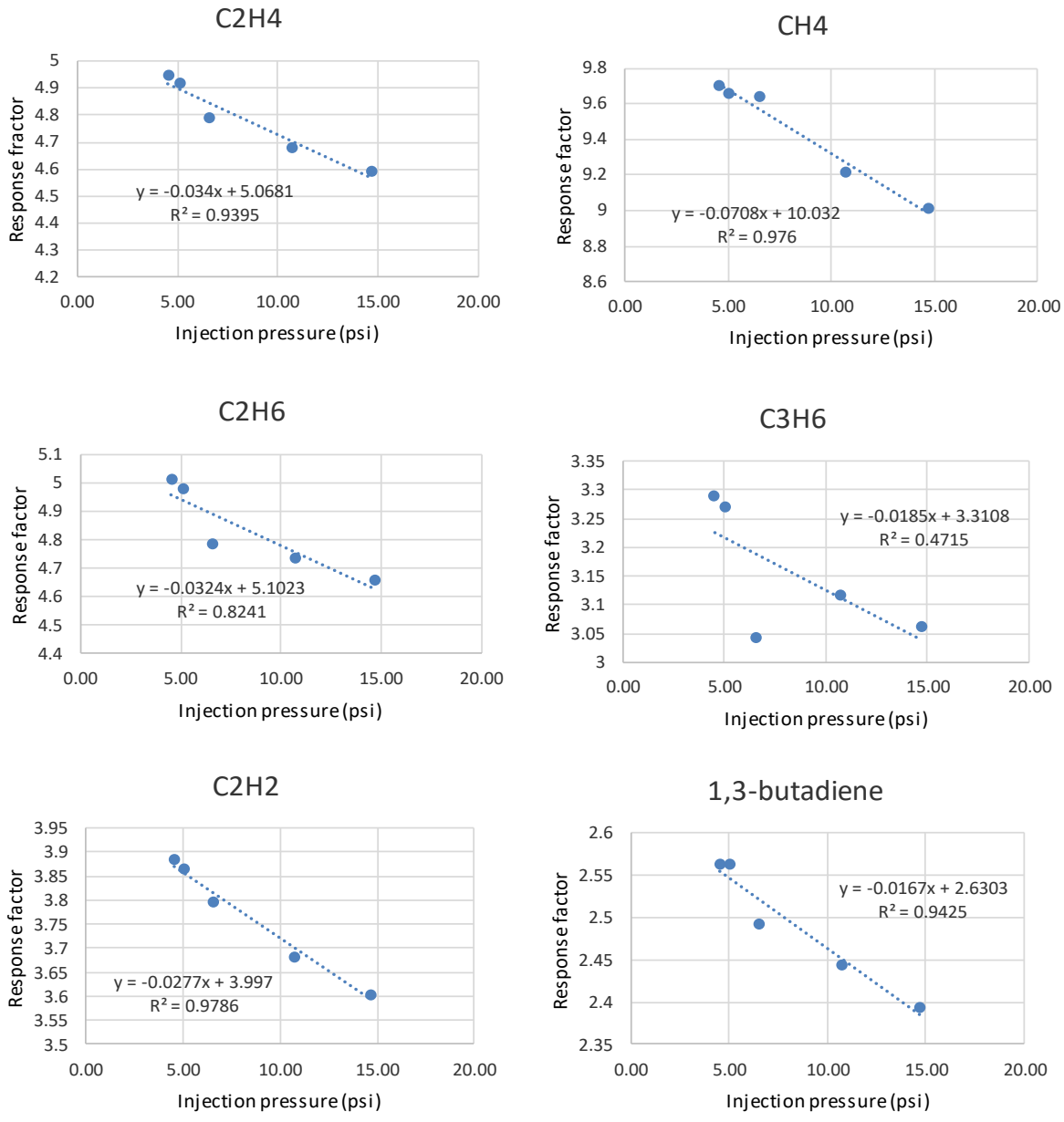

Figure A1: LPST species calibrations on GC FID.

HPST sample species calibrations in GC-FID are shown in Figure A2. Normalized GC area is the GC peak area reading/injection pressure in psi.

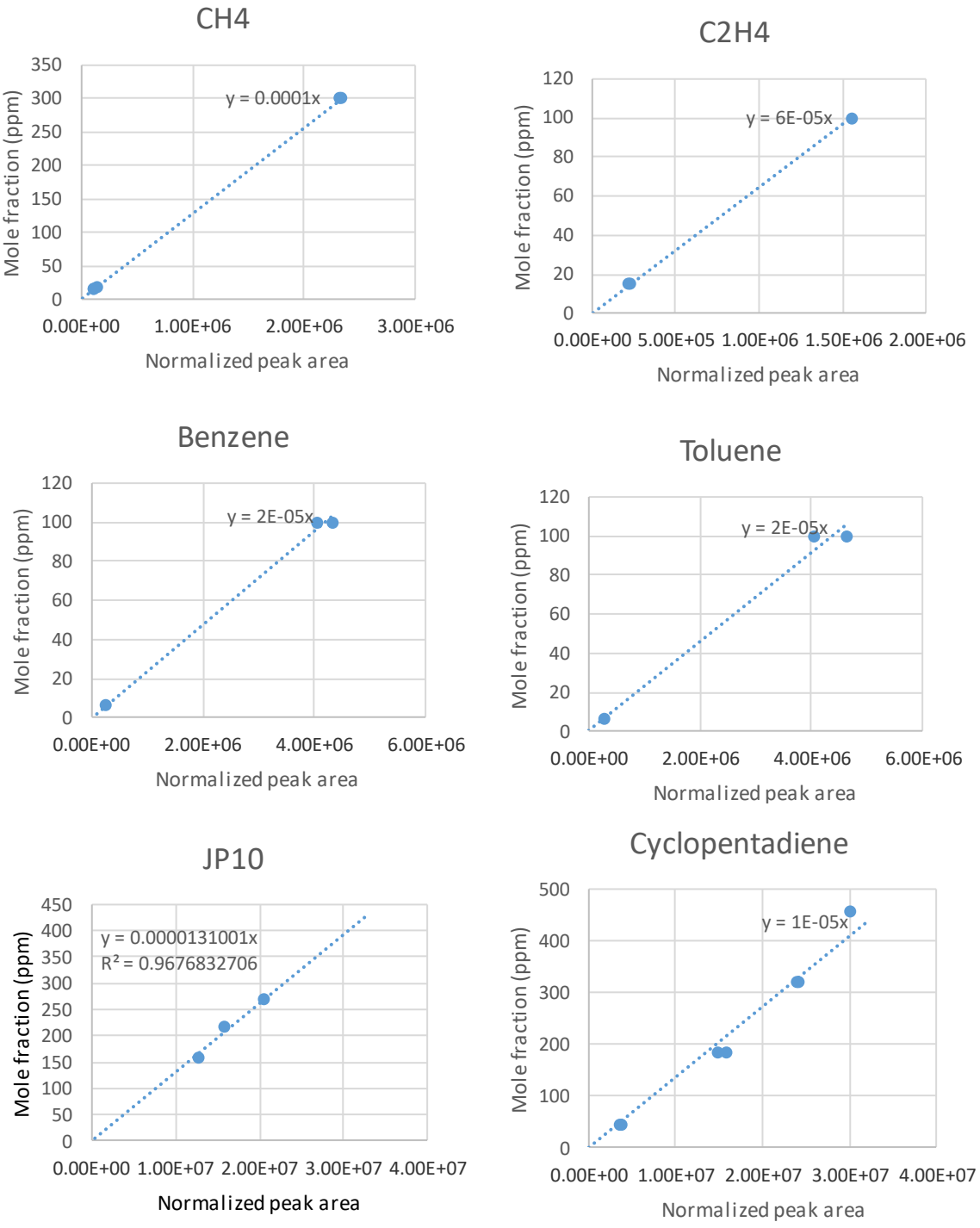

Figure A2: Species calibration in HPST GC-FID.

APPENDIX B

Jet A and JP10 pyrolysis data in HPST and LPST

Table A1: Symbol names in the tables of the experimental data sets of shock tube speciation.

Symbol	Name
T5	Calibrated shock temperature in the HPST
T5_t_extr	Shock temperature through arrival time extrapolation in the LPST
T5_t_extr -	Lower bound of the shock temperature through arrival time extrapolation in the LPST
T5_t_extr +	Upper bound of the shock temperature through arrival time extrapolation in the LPST
T5_v_extr	Shock temperature through velocity extrapolation in the LPST
P5	Shock pressure
τ	Reaction time by 80% rule
CH4	Methane
C2H6	Ethane
C2H4	Ethylene
C2H2	Acetylene
C3H8	Propane
C3H6	Propene
aC3H4	Allene
pC3H4	Propyne
1-C4H8	1-Butene
i-C4H8	Iso-butene
c-2-C4H8	Cis-2-butene
1,3-C4H6	1,3-Butadiene
1,2-C4H6	1,2-Butadiene
C4H4	Vinylacetylene
C4H2	Diacetylene
C5H8	Cyclopentene
C5H6	Cyclopentadiene
C6H6	Benzene
C6H2	1,3,5-hexatriyne
C7H8	Toluene
C10H16	Exo-tetrahydrodicyclopentadiene

Table A3: Experimental data set for HPST Jet A pyrolysis at ~25 atm, with 52.3 ppm fuel in Ar.

T5	P5	τ	CH4	C2H6	C2H4	C2H2	C3H8	C3H6	aC3H4	1-C4H8	pC3H4	1,3-C4H6
K	atm	sec	Mole fraction (ppm)									
843	19	0.00454	0.86	0.00	0.00	0.00	0.00	0.00	0.00	0.00	0.00	0.00
888	19	0.00409	0.76	0.00	0.00	0.00	0.00	0.00	0.00	0.00	0.00	0.00
979	20	0.00313	1.12	0.00	0.00	0.00	0.00	0.00	0.00	0.00	0.00	0.00
1044	23	0.00300	1.09	0.09	0.48	0.00	0.00	0.23	0.00	0.00	0.00	0.00
1068	25	0.00277	1.27	0.63	2.89	0.00	0.00	1.24	0.00	0.33	0.00	0.25
1103	26	0.00260	2.24	2.03	10.47	0.20	0.09	4.34	0.19	1.25	0.08	0.93
1115	25	0.00260	2.53	3.09	15.17	0.30	0.09	6.21	0.21	1.77	0.13	1.39
1129	24	0.00263	2.19	2.21	11.15	0.18	0.05	4.55	0.16	1.30	0.09	0.99
1133	27	0.00253	3.00	4.03	20.12	0.43	0.10	8.14	0.34	2.32	0.23	2.01
1147	27	0.00249	4.89	6.06	31.57	1.07	0.00	12.01	0.59	3.32	0.37	3.16
1183	27	0.00226	6.76	12.23	58.79	2.55	0.20	19.87	1.98	4.50	1.14	6.13
1209	23	0.00237	7.10	12.84	60.88	2.81	0.24	20.16	2.18	4.37	1.28	6.28
1213	26	0.00227	6.73	12.25	58.22	2.55	0.19	19.59	1.93	4.39	1.12	6.07
1227	27	0.00224	7.82	14.37	67.48	3.57	0.24	21.71	2.64	4.13	1.70	6.95
1247	31	0.00222	10.26	17.48	79.66	5.80	0.18	23.14	3.93	2.54	3.21	7.98
1261	27	0.00221	10.39	18.37	81.27	6.36	0.00	22.99	4.23	2.04	3.84	7.97
1293	25	0.00232	16.63	19.81	93.88	14.56	0.07	19.25	4.85	0.46	7.99	7.18
1300	28	0.00215	15.14	19.87	91.80	12.21	0.00	20.35	4.63	0.57	7.32	7.50
1304	27	0.00221	14.93	20.59	90.66	10.43	0.00	21.43	4.65	0.82	6.61	7.85
1342	27	0.00218	19.81	18.49	96.67	19.44	0.00	16.67	4.91	0.38	9.19	6.51
1349	26	0.00221	23.78	17.09	97.70	24.14	0.00	14.38	4.88	0.20	9.52	5.72
1356	29	0.00206	20.70	17.62	96.69	20.87	0.00	15.71	4.87	0.27	9.27	6.19
1367	35	0.00229	21.76	16.28	94.95	21.01	0.00	14.72	4.60	0.24	9.06	5.91
1422	25	0.00211	28.48	14.42	99.70	34.13	0.00	10.67	4.80	0.00	10.15	4.71
1423	25	0.00209	32.43	11.40	99.67	44.18	0.00	7.89	4.50	0.09	9.86	3.78
1436	25	0.00209	34.89	9.06	96.55	51.37	0.00	6.04	4.16	0.07	9.23	3.09
1451	27	0.00210	39.72	6.20	90.21	68.41	0.00	4.16	3.44	0.17	7.73	2.21
1455	25	0.00206	36.41	8.78	98.09	54.74	0.00	5.78	4.11	0.05	9.25	3.01
1498	28	0.00203	42.05	5.06	89.92	73.71	0.00	3.22	3.31	0.00	7.49	1.91
1507	28	0.00203	45.82	2.64	79.09	100.18	0.00	1.80	2.37	0.00	5.54	1.15
1607	34	0.00195	36.59	0.73	31.63	167.61	0.00	0.49	1.05	0.00	2.48	0.31
1615	31	0.00190	40.92	0.93	42.47	154.99	0.00	0.56	1.30	0.00	3.06	0.39
1632	30	0.00189	40.26	0.77	40.15	158.10	0.00	0.48	1.19	0.00	2.90	0.33
1639	30	0.00194	40.61	0.80	42.68	149.91	0.00	0.51	1.22	0.00	3.02	0.36
1640	31	0.00192	29.09	0.43	19.85	180.96	0.00	0.31	0.82	0.00	1.90	0.18
1645	37	0.00200	24.61	0.44	14.16	190.28	0.00	0.27	0.63	0.00	1.52	0.16
1654	30	0.00190	35.78	0.56	31.89	164.53	0.00	0.41	0.99	0.00	2.38	0.28
1694	31	0.00178	27.26	0.34	15.53	192.47	0.00	0.22	0.74	0.00	1.70	0.14
1717	36	0.00180	23.08	0.27	11.58	189.61	0.00	0.22	0.63	0.00	1.49	0.15
1726	34	0.00185	14.26	0.00	6.01	199.71	0.00	0.16	0.52	0.00	0.90	0.11
1729	38	0.00171	18.35	0.28	7.50	198.71	0.00	0.19	0.52	0.00	1.17	0.10
1821	36	0.00174	6.09	0.00	2.10	208.31	0.00	0.20	0.23	0.00	0.49	0.06
1833	25	0.00193	9.27	0.11	3.61	205.46	0.00	0.14	0.28	0.00	0.65	0.05
2018	29	0.00244	3.10	0.25	1.91	199.27	0.00	0.27	0.24	0.00	0.37	0.09
2092	29	0.00318	2.88	0.56	3.42	195.60	0.00	0.50	0.23	0.00	0.43	0.19
2104	34	0.00149	2.84	0.26	2.87	202.92	0.00	0.24	0.17	0.00	0.35	0.10
2134	36	0.00159	2.25	0.00	0.99	212.14	0.00	0.10	0.10	0.00	0.18	0.00

i-C4H8	C4H2	c-2-C4H8	1,2-C4H6	C4H4	C5H8	C5H6	C6H2	C6H6	C7H8
Mole fraction (ppm)									
0.00	0.00	0.00	0.00	0.00	0.00	0.00	0.00	0.05	0.25
0.00	0.00	0.00	0.00	0.00	0.00	0.00	0.00	1.04	0.27
0.00	0.00	0.00	0.00	0.00	0.00	0.00	0.00	0.00	0.29
0.00	0.00	0.00	0.00	0.00	0.00	0.00	0.00	0.05	0.31
0.16	0.06	0.00	0.00	0.00	0.04	0.00	0.00	0.20	0.25
0.47	0.13	0.00	0.11	0.00	0.07	0.13	0.00	0.24	0.31
0.61	0.19	0.00	0.00	0.00	0.12	0.16	0.00	0.26	0.70
0.48	0.13	0.00	0.00	0.00	0.08	0.10	0.00	0.22	0.32
0.80	0.21	0.00	0.00	0.00	0.11	0.28	0.03	0.48	0.40
1.11	0.31	0.00	0.06	0.11	0.16	0.51	0.00	0.88	0.57
1.63	0.43	0.00	0.14	0.31	0.21	1.33	0.00	1.89	0.94
1.64	0.40	0.00	0.15	0.34	0.18	1.35	0.00	2.05	0.98
1.64	0.45	0.00	0.14	0.29	0.22	1.24	0.00	1.69	0.87
1.66	0.48	0.00	0.20	0.42	0.23	1.62	0.00	2.32	1.05
1.68	0.45	0.00	0.23	0.68	0.10	2.23	0.03	2.66	1.37
1.62	0.43	0.00	0.25	0.75	0.15	2.37	0.00	2.90	1.45
0.97	0.22	0.16	0.30	1.57	0.00	2.69	0.63	4.17	2.02
1.20	0.26	0.00	0.33	1.39	0.00	2.78	0.00	3.32	1.84
1.34	0.32	0.00	0.33	1.21	0.05	2.81	0.95	3.23	1.89
0.71	0.36	0.12	0.33	1.98	0.00	2.38	0.92	3.92	2.28
0.92	0.11	0.00	0.31	2.15	0.00	1.97	0.00	4.39	2.26
0.64	0.40	0.13	0.33	2.04	0.00	2.24	0.00	4.10	2.30
0.59	0.36	0.10	0.30	1.98	0.00	2.13	0.00	3.76	2.22
0.27	0.91	0.08	0.34	2.60	0.00	1.44	0.69	4.90	2.41
0.17	1.42	0.03	0.27	2.76	0.00	1.00	0.13	5.05	2.35
0.11	1.88	0.02	0.25	2.73	0.00	0.75	0.04	6.89	2.16
0.09	3.23	0.00	0.21	2.44	0.00	0.53	0.22	6.06	1.66
0.11	2.08	0.03	0.26	2.73	0.00	0.72	0.06	6.54	2.13
0.00	3.54	0.00	0.18	2.47	0.00	0.39	0.99	6.28	1.56
0.00	5.81	0.00	0.11	1.85	0.00	0.25	0.36	6.81	0.98
0.00	15.13	0.00	0.00	0.74	0.00	0.00	1.88	3.27	0.17
0.00	13.11	0.00	0.04	0.91	0.00	0.11	1.38	4.48	0.26
0.00	13.62	0.00	0.06	0.89	0.00	0.09	1.43	3.68	0.23
0.00	11.85	0.00	0.03	0.92	0.00	0.13	1.09	3.83	0.27
0.00	18.57	0.00	0.00	0.52	0.00	0.09	2.35	2.74	0.13
0.00	20.56	0.00	0.00	0.44	0.00	0.00	2.83	1.47	0.07
0.00	15.15	0.00	0.12	0.74	0.00	0.09	1.88	3.02	0.20
0.00	20.88	0.00	0.00	0.47	0.00	0.06	3.07	2.11	0.08
0.00	21.26	0.00	0.00	0.44	0.00	0.07	2.86	1.48	0.05
0.00	25.56	0.00	0.00	0.30	0.00	0.00	3.56	2.30	0.00
0.00	24.01	0.00	0.00	0.37	0.00	0.00	3.23	0.94	0.00
0.00	29.43	0.00	0.00	0.27	0.00	0.00	4.35	0.26	0.00
0.00	27.93	0.00	0.00	0.30	0.00	0.00	4.05	0.44	0.00
0.00	28.03	0.00	0.00	0.31	0.00	0.00	3.92	0.28	0.00
0.00	26.93	0.00	0.00	0.38	0.00	0.10	3.70	0.26	0.08
0.00	29.14	0.00	0.06	0.36	0.00	0.05	4.39	0.91	0.05
0.00	30.85	0.00	0.00	0.31	0.00	0.00	4.44	1.06	0.00

Table A4: Experimental data set for HPST Jet A pyrolysis at ~90 atm, with 52.3 ppm fuel in Ar.

T5	P5	τ	CH4	C2H6	C2H4	C2H2	C3H8	C3H6	aC3H4	1-C4H8	pC3H4	1,3-C4H6
K	atm	sec	Mole fraction (ppm)									
707	34	0.00287	1.05	0.00	0.32	0.00	0.00	0.12	0.00	0.00	0.00	0.00
1004	55	0.00334	1.06	0.00	0.24	0.00	0.00	0.00	0.00	0.00	0.00	0.00
1011	69	0.00262	0.00	0.00	0.00	0.00	0.00	0.00	0.00	0.00	0.00	0.00
1047	69	0.00264	0.99	0.50	3.07	0.00	0.00	1.31	0.00	0.37	0.00	0.24
1050	53	0.00331	1.65	0.33	1.85	0.00	0.00	0.84	0.00	0.28	0.00	0.14
1118	83	0.00246	2.71	2.04	12.01	0.19	0.08	4.98	0.13	1.51	0.12	1.09
1125	86	0.00243	3.44	2.28	13.79	0.26	0.00	5.67	0.16	1.65	0.12	1.27
1138	98	0.00240	5.94	5.87	35.30	1.00	0.15	13.06	0.59	3.93	0.35	3.59
1146	91	0.00226	5.08	5.12	30.65	0.76	0.13	11.55	0.46	3.53	0.31	3.05
1148	99	0.00241	5.84	5.18	31.43	0.86	0.15	11.91	0.47	3.62	0.34	3.17
1160	90	0.00238	4.10	3.84	23.05	0.52	0.10	9.07	0.30	2.72	0.20	2.27
1171	85	0.00234	6.90	8.07	46.53	1.60	0.18	16.62	0.90	4.93	0.62	4.85
1191	98	0.00224	8.88	10.34	60.26	2.79	0.21	19.77	1.58	5.21	1.08	6.47
1196	91	0.00225	10.37	12.73	70.35	3.87	0.21	22.14	2.37	4.92	1.62	7.43
1199	88	0.00224	9.67	12.44	69.03	3.67	0.26	21.89	2.20	5.06	1.44	7.26
1209	106	0.00220	11.75	13.59	75.61	4.93	0.25	22.85	2.87	4.31	2.14	7.94
1213	108	0.00231	10.77	12.40	69.86	4.00	0.22	21.98	2.40	4.81	1.60	7.46
1249	103	0.00224	13.14	14.86	79.75	6.09	0.22	22.65	3.53	3.04	2.86	8.04
1250	112	0.00216	13.88	15.26	81.66	6.72	0.20	22.95	3.77	2.58	3.32	8.30
1252	104	0.00219	12.53	14.52	80.33	5.56	0.23	23.83	3.15	4.29	2.41	8.42
1255	96	0.00233	13.00	15.06	82.12	5.68	0.24	24.08	3.33	3.99	2.49	8.42
1266	105	0.00217	14.32	15.81	84.59	7.26	0.19	23.15	4.00	2.50	3.49	8.27
1284	110	0.00214	17.62	16.70	89.93	10.66	0.13	21.49	4.36	1.09	6.00	8.10
1306	111	0.00213	18.33	16.65	92.55	11.71	0.17	21.20	4.34	1.05	6.10	8.10
1320	111	0.00206	25.90	13.84	95.78	21.83	0.05	15.08	4.43	0.45	8.63	6.13
1322	108	0.00213	20.21	16.13	92.31	13.81	0.10	19.34	4.31	0.76	7.13	7.38
1329	103	0.00212	21.05	16.74	96.13	14.88	0.09	19.52	4.41	0.71	7.55	7.42
1333	97	0.00219	20.81	16.68	94.96	14.43	0.12	19.43	4.33	0.66	7.31	7.31
1346	72	0.00223	17.56	17.69	91.17	11.40	0.10	20.57	4.33	0.62	6.53	7.59
1375	103	0.00211	26.65	13.71	96.92	22.15	0.00	15.02	4.44	0.38	8.69	6.16
1378	104	0.00210	29.89	12.28	97.88	26.69	0.00	12.99	4.33	0.39	8.79	5.40
1390	103	0.00209	32.58	10.88	99.99	31.70	0.00	11.33	4.44	0.21	8.99	4.89
1393	95	0.00210	31.45	11.33	98.08	29.80	0.00	11.61	4.37	0.26	8.87	4.89
1414	109	0.00208	36.45	8.17	95.99	37.89	0.00	8.44	4.10	0.24	8.57	3.79
1418	101	0.00206	32.81	9.76	94.75	32.01	0.00	9.75	4.17	0.25	8.68	4.25
1430	105	0.00205	46.39	4.69	94.92	60.78	0.00	4.80	3.56	0.16	7.74	2.35
1437	97	0.00206	45.68	6.63	86.61	65.78	0.00	4.05	2.97	0.16	6.85	2.05
1446	108	0.00204	42.74	6.16	96.50	51.61	0.00	6.21	3.80	0.20	8.17	2.84
1469	102	0.00205	47.45	5.69	83.72	72.09	0.00	2.98	2.68	0.00	6.36	1.62
1492	76	0.00172	47.31	2.47	78.05	81.03	0.00	2.45	2.38	0.08	5.46	1.28
1522	101	0.00199	51.09	2.19	78.90	88.72	0.00	2.31	2.32	0.08	5.22	1.16
1538	75	0.00310	49.43	1.38	59.36	111.10	0.00	0.96	1.64	0.00	3.83	0.60
1600	103	0.00194	44.53	0.83	34.01	146.93	0.00	0.73	1.09	0.06	2.54	0.37
1638	97	0.00194	29.51	0.36	14.04	178.91	0.00	0.38	0.71	0.00	1.67	0.18
1714	91	0.00184	32.15	0.34	12.45	180.90	0.00	0.24	0.69	0.08	1.61	0.15
1782	81	0.00297	9.40	0.00	2.87	196.45	0.00	0.08	0.23	0.00	0.52	0.04
1803	99	0.00188	13.50	0.27	2.88	190.97	0.00	0.17	0.22	0.07	1.28	0.08
1805	90	0.00178	9.83	0.00	3.28	197.46	0.00	0.10	0.27	0.00	0.62	0.07
1847	95	0.00190	4.57	0.00	1.57	202.74	0.00	0.07	0.14	0.00	0.31	0.00
1899	90	0.00202	0.00	0.00	1.38	194.35	0.00	0.17	0.25	0.11	1.65	0.07
2077	79	0.00300	2.38	0.00	1.31	192.58	0.00	0.13	0.20	0.10	1.23	0.06

i-C4H8	C4H2	c-2-C4H8	1,2-C4H6	C4H4	C5H8	C5H6	C6H2	C6H6	C7H8
Mole fraction (ppm)									
0.00	0.00	0.00	0.00	0.00	0.00	0.00	0.00	0.00	0.26
0.00	0.00	0.00	0.00	0.00	0.00	0.00	0.00	0.00	0.33
0.00	0.00	0.00	0.00	0.00	0.00	0.00	0.00	0.00	0.00
0.15	0.00	0.04	0.00	0.00	0.00	0.00	0.00	0.09	0.27
0.10	0.00	0.00	0.00	0.00	0.00	0.00	0.00	0.06	0.29
0.53	0.00	0.12	0.00	0.00	0.13	0.11	0.00	0.32	0.35
0.59	0.00	0.14	0.00	0.00	0.11	0.16	0.13	0.33	0.43
1.25	0.00	0.28	0.07	0.11	0.17	0.53	0.00	0.81	0.57
1.09	0.00	0.25	0.04	0.11	0.16	0.40	0.00	0.67	0.52
1.16	0.00	0.27	0.05	0.13	0.19	0.46	0.00	0.77	0.58
0.90	0.00	0.20	0.03	0.05	0.14	0.29	0.00	0.56	0.49
1.46	0.00	0.33	0.08	0.20	0.21	0.76	0.00	1.65	0.64
1.59	0.00	0.36	0.11	0.34	0.20	1.27	0.05	0.00	0.83
1.68	0.00	0.39	0.13	0.46	0.19	1.60	0.00	2.37	1.04
1.74	0.00	0.40	0.16	0.42	0.17	1.58	0.00	2.15	1.03
1.73	0.00	0.39	0.22	0.59	0.19	1.85	0.00	2.47	1.17
1.73	0.00	0.39	0.18	0.47	0.17	1.61	0.00	2.34	1.08
1.67	0.00	0.38	0.21	0.70	0.11	2.02	0.00	2.62	1.18
1.62	0.00	0.38	0.22	0.80	0.10	2.30	0.00	2.97	1.43
1.77	0.00	0.40	0.21	0.65	0.15	2.07	0.00	2.94	1.34
1.76	0.00	0.43	0.21	0.63	0.15	2.07	0.00	2.84	1.22
1.61	0.00	0.37	0.24	0.82	0.09	2.39	0.04	3.02	1.44
1.45	0.00	0.30	0.25	1.22	0.06	2.64	0.00	3.33	1.68
1.32	0.00	0.26	0.27	1.41	0.17	2.74	0.00	3.56	1.74
0.62	0.37	0.11	0.25	2.05	0.00	2.26	0.00	4.36	2.22
1.08	0.11	0.21	0.26	1.52	0.06	2.62	0.00	3.61	0.00
1.04	0.14	0.19	0.26	1.56	0.04	2.64	0.38	4.08	1.77
1.05	0.13	0.19	0.25	1.50	0.05	2.50	0.00	3.82	1.70
1.20	0.26	0.00	0.28	1.26	0.06	2.64	0.22	5.93	1.65
0.62	0.33	0.11	0.24	2.09	0.00	2.27	0.25	5.72	2.40
0.47	0.48	0.11	0.26	2.23	0.00	1.89	0.28	4.29	2.13
0.35	0.66	0.07	0.20	2.47	0.00	1.68	0.00	5.22	2.49
0.35	0.55	0.07	0.25	2.30	0.00	1.63	0.00	4.97	1.93
0.22	0.79	0.07	0.19	2.31	0.00	1.22	0.00	5.36	2.12
0.25	0.62	0.06	0.21	2.29	0.00	1.37	0.07	4.83	2.25
0.08	1.71	0.03	0.14	2.34	0.00	0.65	0.13	6.63	1.86
0.05	2.28	0.00	0.09	2.13	0.00	0.56	0.09	6.14	1.46
0.12	1.25	0.02	0.14	2.38	0.00	0.91	0.11	6.31	1.88
0.00	2.67	0.00	0.06	2.06	0.00	0.52	0.06	7.29	1.63
0.00	3.34	0.00	0.07	1.73	0.00	0.30	0.19	7.62	1.13
0.00	3.34	0.00	0.09	1.64	0.00	0.34	0.11	6.47	1.01
0.00	4.48	0.00	0.00	1.37	0.00	0.29	0.00	5.21	0.58
0.00	9.55	0.00	0.03	0.74	0.00	0.23	0.73	4.48	0.22
0.00	15.91	0.00	0.06	0.58	0.00	0.12	1.95	2.54	0.13
0.00	16.26	0.00	0.00	0.62	0.00	0.00	1.86	1.96	0.08
0.00	24.10	0.00	0.03	0.43	0.00	0.15	0.00	0.52	0.00
0.00	20.60	0.00	0.00	0.50	0.00	0.00	2.14	0.62	0.00
0.00	23.82	0.00	0.00	0.47	0.00	0.00	3.19	0.51	0.00
0.00	26.30	0.00	0.00	0.47	0.00	0.00	3.60	0.30	0.00
0.00	19.49	0.00	0.00	0.50	0.00	0.22	1.62	0.57	0.00
0.00	18.24	0.00	0.00	0.50	0.00	0.20	1.51	0.28	0.09

Table A5: Experimental data set for HPST JP10 pyrolysis at ~25 atm, with 72 ppm fuel in Ar.

T5	P5	τ	CH4	C2H6	C2H4	C2H2	C3H6	aC3H4	1-C4H8	pC3H4	1,3-C4H6	C4H2
K	atm	sec	Mole fraction (ppm)									
921	22	0.00349	0.00	0.00	0.00	0.00	0.00	0.00	0.00	0.00	0.00	0.00
1050	23	0.00282	0.00	0.00	0.00	0.00	0.00	0.00	0.00	0.00	0.00	0.00
1065	24	0.00287	0.00	0.00	0.00	0.00	0.00	0.00	0.00	0.00	0.00	0.00
1079	33	0.00272	0.00	0.00	0.00	0.00	0.00	0.00	0.00	0.00	0.00	0.00
1099	23	0.00267	0.00	0.00	0.25	0.00	0.00	0.00	0.00	0.00	0.00	0.00
1116	24	0.00244	1.40	0.07	4.93	0.23	1.04	0.65	0.52	0.14	0.35	0.00
1123	24	0.00245	0.00	0.00	0.76	0.00	0.00	0.00	0.00	0.00	0.00	0.00
1137	23	0.00241	0.92	0.00	6.68	0.34	1.56	0.90	0.65	0.26	0.47	0.00
1162	25	0.00230	0.64	0.11	8.40	0.43	1.93	1.02	0.82	0.30	0.62	0.00
1186	25	0.00234	1.39	0.48	17.46	1.30	4.09	2.32	1.52	0.95	1.42	0.00
1199	25	0.00227	1.22	0.41	14.75	0.99	3.46	1.97	1.38	0.75	1.15	0.00
1207	21	0.00233	3.98	2.24	39.40	5.25	7.96	4.85	1.53	3.67	3.40	0.04
1222	23	0.00222	3.21	1.66	34.22	3.90	7.23	4.36	1.73	2.82	2.93	0.04
1238	24	0.00223	3.86	2.07	38.37	4.78	7.80	4.75	1.63	3.46	3.29	0.00
1274	24	0.00233	5.73	3.17	49.76	7.90	9.35	5.79	1.26	5.43	4.26	0.09
1288	30	0.00214	6.89	3.69	55.53	10.78	9.39	6.11	0.77	7.05	4.77	0.14
1292	26	0.00219	7.12	3.97	55.98	11.27	9.28	6.05	0.75	7.24	4.71	0.14
1324	21	0.00220	8.87	4.72	60.89	16.72	8.80	5.96	0.38	9.30	4.92	0.32
1334	31	0.00211	10.82	4.59	63.69	21.87	8.34	5.99	0.23	10.47	4.87	0.51
1344	29	0.00218	10.09	4.44	62.40	20.35	8.42	5.90	0.30	10.16	4.86	0.45
1366	23	0.00214	11.14	4.83	65.45	25.89	7.91	6.14	0.18	11.20	4.87	0.71
1401	32	0.00208	15.25	4.13	66.05	39.33	6.20	5.81	0.10	12.01	4.27	1.45
1426	32	0.00211	19.77	3.01	65.83	59.71	3.93	5.66	0.05	12.43	3.30	3.10
1442	31	0.00208	19.44	3.14	65.67	59.19	3.96	5.61	0.04	12.41	3.34	3.05
1473	31	0.00205	23.52	2.40	64.42	76.53	2.65	5.02	0.03	11.45	2.56	4.76
1506	30	0.00203	26.54	1.72	63.88	94.28	1.79	4.43	0.00	10.30	1.98	6.68
1520	29	0.00203	26.79	1.48	59.67	97.88	1.42	3.94	0.00	9.24	1.63	7.62
1529	34	0.00200	29.33	0.77	47.07	133.42	0.77	2.34	0.00	5.40	0.76	13.99
1543	32	0.00196	29.45	0.93	53.68	122.01	0.88	2.94	0.00	6.86	1.02	11.39
1576	35	0.00188	30.25	0.58	40.61	154.10	0.46	1.88	0.00	4.40	0.52	17.67
1582	28	0.00189	27.83	0.58	43.07	146.07	0.50	2.12	0.00	4.98	0.63	16.88
1636	24	0.00189	20.95	0.26	20.37	205.22	0.14	0.97	0.00	2.29	0.19	30.38
1689	34	0.00181	16.27	0.15	9.67	229.29	0.09	0.65	0.00	1.47	0.11	35.18
1745	23	0.00239	6.35	0.00	3.94	236.12	0.00	0.00	0.00	0.63	0.05	40.41
1754	23	0.00188	15.63	0.05	10.23	225.13	0.06	0.60	0.00	1.42	0.12	34.54
1781	19	0.00507	3.66	0.18	4.64	226.71	0.12	0.34	0.00	0.69	0.14	39.20

1,2-C4H6	C4H4	C5H8	C5H6	C6H2	C6H6	C7H8	C10H16
Mole fraction (ppm)							
0.00	0.00	0.00	0.00	0.00	0.00	0.00	69.19
0.00	0.00	0.00	0.00	0.00	0.00	0.00	69.65
0.00	0.00	0.00	0.00	0.00	0.00	0.00	67.90
0.00	0.00	0.00	0.00	0.00	0.00	0.00	58.78
0.00	0.00	0.00	0.00	0.00	0.00	0.00	68.63
0.00	0.00	1.17	3.84	0.38	1.23	0.18	61.75
0.00	0.00	0.24	0.54	0.14	0.16	0.00	68.47
0.00	0.08	1.52	5.18	0.00	1.71	0.28	58.31
0.07	0.00	1.77	6.40	0.00	2.12	0.35	56.40
0.04	0.23	2.39	12.95	0.04	5.46	0.86	46.33
0.00	0.18	2.78	10.43	0.39	4.34	0.73	49.55
0.14	0.82	1.97	27.27	0.08	14.67	2.26	23.12
0.13	0.65	2.30	24.36	0.07	12.47	1.89	28.20
0.12	0.75	2.10	26.84	0.08	14.34	2.16	24.40
0.16	1.14	1.51	33.03	0.08	19.19	2.97	16.00
0.21	1.54	1.02	35.40	0.05	22.04	3.49	10.24
0.21	1.54	0.90	34.98	0.06	22.02	3.52	8.72
0.22	2.03	0.48	34.12	0.05	24.63	4.02	5.25
0.21	2.36	0.35	31.74	0.03	26.44	4.33	3.60
0.23	2.24	0.38	32.13	0.02	25.80	4.24	4.23
0.25	2.63	0.25	30.01	0.03	27.14	4.35	2.82
0.22	3.25	0.12	20.92	0.03	29.00	4.36	1.53
0.19	3.64	0.09	10.82	0.03	30.78	4.06	1.22
0.21	3.72	0.06	10.97	0.00	29.90	3.98	0.97
0.15	3.72	0.05	6.38	0.00	30.18	3.37	0.69
0.11	3.56	0.00	3.99	0.21	30.61	2.81	0.54
0.12	3.24	0.03	3.07	0.34	28.91	2.40	0.52
0.05	1.88	0.00	1.50	1.17	24.08	1.11	0.46
0.07	2.43	0.00	1.61	0.75	26.73	1.54	0.40
0.04	1.54	0.00	0.81	1.64	21.10	0.75	0.35
0.06	1.73	0.00	0.86	1.54	21.77	0.83	0.38
0.10	0.77	0.00	0.21	4.15	9.53	0.18	0.22
0.00	0.51	0.00	0.20	5.06	4.82	0.10	0.19
0.04	0.27	0.00	0.14	6.89	1.67	0.04	0.14
0.00	0.51	0.00	0.13	5.17	4.86	0.09	0.18
0.04	0.33	0.00	0.46	6.92	1.68	0.11	0.35

Table A6: Experimental data set for HPST JP10 pyrolysis at ~90 atm, with 72 ppm fuel in Ar.

T5	P5	τ	CH4	C2H6	C2H4	C2H2	C3H6	aC3H4	1-C4H8	pC3H4	1,3-C4H6	C4H2
K	atm	sec	Mole fraction (ppm)									
941	76	0.00289	0.00	0.00	0.00	0.00	0.00	0.00	0.00	0.00	0.00	0.00
1064	100	0.00243	0.00	0.00	0.00	0.00	0.00	0.00	0.00	0.00	0.00	0.00
1070	84	0.00247	0.00	0.00	0.00	0.00	0.00	0.00	0.00	0.00	0.00	0.00
1085	86	0.00240	0.00	0.00	0.11	0.00	0.00	0.00	0.00	0.00	0.00	0.00
1089	75	0.00240	0.90	0.00	0.28	0.00	0.05	0.00	0.00	0.00	0.00	0.00
1124	108	0.00237	0.77	0.00	1.59	0.08	0.27	0.16	0.14	0.00	0.12	0.00
1140	90	0.00226	0.85	0.00	6.50	0.34	1.50	0.77	0.75	0.22	0.52	0.00
1157	94	0.00230	0.58	0.00	2.95	0.00	0.58	0.33	0.31	0.09	0.21	0.00
1180	88	0.00225	1.51	0.21	14.89	1.03	3.48	1.77	1.51	0.70	1.25	0.00
1183	94	0.00228	1.03	0.11	9.43	0.58	2.25	1.16	1.01	0.37	0.75	0.00
1193	86	0.00236	2.22	0.57	21.63	2.02	4.96	2.58	1.80	1.30	1.93	0.00
1216	85	0.00231	1.91	0.36	18.73	1.45	4.42	2.25	1.75	0.97	1.61	0.00
1250	97	0.00220	7.48	2.47	48.74	8.63	8.95	5.18	1.07	5.37	4.37	0.10
1283	111	0.00214	10.07	2.91	55.17	12.90	8.89	5.12	0.53	7.28	4.81	0.20
1320	92	0.00215	11.91	3.35	58.93	17.35	8.38	5.05	0.30	8.66	4.68	0.33
1321	108	0.00212	10.43	3.01	56.63	13.22	8.99	5.16	0.54	7.39	4.81	0.21
1345	99	0.00217	13.12	3.18	59.46	21.23	7.71	4.69	0.32	8.38	4.67	0.40
1356	79	0.00210	12.43	3.52	60.48	19.42	8.26	5.14	0.27	9.12	4.76	0.38
1358	86	0.00212	13.31	3.47	61.91	20.99	8.16	5.06	0.29	9.26	4.65	0.40
1423	95	0.00198	23.79	1.81	62.11	59.50	3.28	4.43	0.08	9.65	2.49	2.56
1459	86	0.00203	25.41	1.54	60.59	67.09	2.68	4.12	0.06	9.26	2.10	3.27
1513	105	0.00201	30.93	0.61	47.88	101.12	0.97	2.14	0.04	4.83	0.78	6.28
1518	89	0.00201	29.63	0.44	35.62	126.97	0.68	1.45	0.00	3.26	0.50	11.31
1562	94	0.00195	31.09	0.41	35.08	135.60	0.60	1.43	0.00	3.27	0.48	11.59
1598	95	0.00192	28.70	0.27	25.01	154.04	0.33	1.11	0.00	2.53	0.30	15.24
1612	90	0.00191	28.78	0.22	24.46	156.24	0.32	1.06	0.00	2.49	0.34	15.10
1665	89	0.00188	22.36	0.18	12.41	190.79	0.16	0.70	0.00	1.63	0.19	22.38
1705	92	0.00187	9.25	0.00	4.06	209.65	0.09	0.36	0.00	0.87	0.12	27.43
1719	95	0.00181	13.30	0.09	4.94	205.86	0.09	0.40	0.00	0.98	0.08	26.28
1723	92	0.00185	11.33	0.07	4.76	209.66	0.11	0.41	0.00	0.99	0.08	27.46
1754	94	0.00178	11.17	0.07	3.32	205.43	0.06	0.37	0.00	0.91	0.08	26.67
1796	83	0.00170	5.56	0.00	2.80	225.12	0.11	0.23	0.04	0.55	0.06	33.57
1944	81	0.00293	1.63	0.00	0.95	233.14	0.00	0.11	0.00	0.21	0.00	38.90
1998	98	0.00164	1.29	0.00	0.84	237.24	0.00	0.08	0.00	0.15	0.00	40.27
2025	94	0.00165	1.16	0.00	0.86	235.69	0.00	0.00	0.00	0.14	0.00	40.51
2043	67	0.00352	1.09	0.00	0.73	231.54	0.00	0.08	0.00	0.16	0.00	38.28

1,2-C4H6	C4H4	C5H8	C5H6	C6H2	C6H6	C7H8	C10H16
Mole fraction (ppm)							
0.00	0.00	0.00	0.00	0.00	0.02	0.00	74.15
0.00	0.00	0.05	0.10	0.00	0.04	0.00	74.05
0.00	0.00	0.00	0.00	0.00	0.00	0.00	72.57
0.00	0.00	0.03	0.06	0.00	0.00	0.00	84.81
0.00	0.00	0.09	0.17	0.00	0.09	0.00	65.75
0.00	0.00	0.43	1.18	0.00	0.33	0.06	63.07
0.07	0.00	1.53	5.15	0.02	1.81	0.29	73.97
0.00	0.00	0.84	2.26	0.00	0.65	0.10	64.07
0.03	0.21	2.38	10.87	0.06	4.29	0.62	45.78
0.00	0.11	1.85	7.09	0.04	2.55	0.42	51.19
0.05	0.37	2.53	15.54	0.07	7.08	1.04	40.03
0.03	0.26	2.59	13.76	0.07	5.92	0.89	41.09
0.16	1.31	1.17	30.85	0.07	18.75	2.71	13.67
0.19	1.84	0.63	32.67	0.07	23.67	3.77	9.57
0.15	2.07	0.42	30.62	0.04	24.42	3.94	5.00
0.16	1.77	0.65	32.58	0.05	22.96	3.51	7.40
0.17	2.82	0.38	29.66	0.05	23.83	3.63	3.83
0.17	2.31	0.36	30.63	0.04	26.10	4.30	4.06
0.17	2.29	0.35	28.45	0.03	23.97	3.61	3.34
0.10	3.21	0.10	8.52	0.03	27.33	3.21	1.13
0.09	3.07	0.06	6.39	0.05	29.80	3.40	0.90
0.05	1.72	0.04	2.26	0.22	26.25	1.42	0.50
0.03	1.08	0.04	1.79	0.80	21.89	0.78	0.44
0.02	1.10	0.00	1.33	0.71	21.29	0.66	0.39
0.01	0.91	0.00	0.68	1.26	16.96	0.44	0.54
0.00	0.93	0.00	0.67	1.13	15.20	0.40	0.25
0.01	0.78	0.00	0.35	1.97	8.66	0.19	0.15
0.00	0.58	0.00	0.24	3.14	2.16	0.08	0.08
0.00	0.64	0.00	0.20	2.86	2.91	0.09	0.08
0.02	0.57	0.00	0.22	3.27	2.79	0.00	0.07
0.00	0.59	0.00	0.15	2.94	1.71	0.05	0.07
0.05	0.48	0.00	0.13	4.46	1.30	0.05	0.06
0.00	0.49	0.00	0.04	5.61	0.41	0.00	0.05
0.04	0.44	0.00	0.00	5.78	0.34	0.00	0.05
0.04	0.47	0.00	0.03	5.76	0.37	0.00	0.05
0.00	0.45	0.00	0.03	6.01	0.28	0.00	0.03

Table A7: Experimental data set for LPST Jet A pyrolysis at ~1 atm, with 2705 ppm fuel in Ar.

T5_t_extr	T5_t_extr -	T5_t_extr +	T5_v_extr	P5	τ	CH4	C2H6	C2H4	C2H2	C3H8	C3H6	aC3H4
K	K	K	K	atm	sec	Mole fraction (ppm)						
912.0	880.3	944.3	671.9	1.28	0.00180	0.0000	0.0000	0.0016	0.0000	0.0000	0.0000	0.0000
1003.0	995.9	1010.2	997.0	1.19	0.00209	0.0028	0.0008	0.0083	0.0000	0.0000	0.0039	0.0000
1041.7	1028.9	1054.7	1033.8	1.23	0.00189	0.0052	0.0017	0.0150	0.0000	0.0000	0.0073	0.0000
1042.7	1031.5	1053.9	1036.5	1.21	0.00187	0.0020	0.0005	0.0056	0.0000	0.0000	0.0028	0.0000
1047.7	1041.0	1054.3	1040.5	1.23	0.00211	0.0121	0.0064	0.0488	0.0000	0.0008	0.0235	0.0000
1079.2	1074.3	1084.2	1087.2	1.21	0.00194	0.0163	0.0105	0.0701	0.0000	0.0013	0.0339	0.0002
1087.9	1078.9	1097.0	1081.0	1.22	0.00207	0.0244	0.0174	0.1149	0.0000	0.0022	0.0542	0.0004
1090.7	1073.8	1107.7	1084.2	1.24	0.00176	0.0106	0.0096	0.0585	0.0000	0.0000	0.0281	0.0000
1107.8	1095.5	1120.2	1098.4	1.25	0.00181	0.0155	0.0096	0.0701	0.0000	0.0010	0.0335	0.0000
1120.9	1114.8	1126.9	1115.6	1.27	0.00191	0.0431	0.0385	0.2393	0.0006	0.0000	0.1097	0.0013
1126.0	1111.8	1140.3	1115.5	1.21	0.00212	0.0412	0.0353	0.2236	0.0004	0.0043	0.1031	0.0012
1157.8	1151.5	1164.2	1149.0	1.19	0.00227	0.0841	0.0882	0.5450	0.0025	0.0102	0.2309	0.0050
1209.8	1205.9	1213.7	1203.7	1.24	0.00195	0.1281	0.1658	0.9610	0.0169	0.0173	0.3605	0.0161
1219.0	1212.0	1226.0	1213.0	1.18	0.00223	0.1774	0.2174	1.2637	0.0221	0.0214	0.4442	0.0260
1244.1	1235.9	1252.4	1241.9	1.22	0.00205	0.1456	0.2011	1.0752	0.0236	0.0151	0.3529	0.0274
1248.5	1237.0	1260.1	1239.5	1.11	0.00239	0.1895	0.2217	1.2776	0.0256	0.0184	0.4156	0.0313
1319.2	1315.7	1322.7	1317.8	1.10	0.00240	0.3114	0.3255	1.7280	0.0933	0.0181	0.4624	0.0802
1348.8	1334.8	1362.8	1353.4	1.21	0.00202	0.3068	0.3268	1.7410	0.0872	0.0188	0.4638	0.0761
1401.0	1389.0	1413.0	1397.9	1.16	0.00200	0.3962	0.3101	1.8178	0.1531	0.0087	0.3504	0.0765
1463.5	1444.6	1482.5	1459.2	1.12	0.00221	0.5657	0.1972	1.8159	0.3968	0.0021	0.1563	0.0571
1662.6	1641.2	1684.1	1651.8	1.14	0.00230	0.7887	0.0332	1.4017	1.5165	0.0000	0.0311	0.0265
1780.1	1759.5	1800.7	1764.2	1.10	0.00234	0.2852	0.0075	0.1918	2.2102	0.0000	0.0053	0.0073
1845.8	1821.7	1870.1	1843.6	1.10	0.00211	0.1001	0.0030	0.0471	1.4794	0.0000	0.0020	0.0024
2083.6	2065.1	2102.2	2084.5	1.21	0.00175	0.0489	0.0000	0.0207	1.9438	0.0000	0.0020	0.0014

1-C4H8	pC3H4	1,3-C4H6	i-C4H8	1,2-C4H6	C4H4
Mole fraction (ppm)					
0.0000	0.0000	0.0000	0.0000	0.0000	0.0000
0.0011	0.0000	0.0000	0.0004	0.0000	0.0000
0.0019	0.0000	0.0006	0.0009	0.0000	0.0000
0.0006	0.0000	0.0002	0.0003	0.0001	0.0000
0.0063	0.0000	0.0024	0.0028	0.0000	0.0000
0.0093	0.0002	0.0037	0.0046	0.0000	0.0000
0.0148	0.0003	0.0066	0.0063	0.0000	0.0000
0.0075	0.0000	0.0033	0.0036	0.0000	0.0000
0.0091	0.0000	0.0038	0.0038	0.0020	0.0000
0.0311	0.0009	0.0166	0.0122	0.0000	0.0003
0.0003	0.0006	0.0154	0.0113	0.0000	0.0000
0.0708	0.0028	0.0488	0.0227	0.0006	0.0012
0.1104	0.0110	0.0984	0.0334	0.0018	0.0032
0.1252	0.0159	0.1406	0.0394	0.0024	0.0053
0.0832	0.0176	0.1186	0.0284	0.0024	0.0062
0.0998	0.0196	0.1420	0.0333	0.0027	0.0072
0.0348	0.0681	0.1705	0.0294	0.0049	0.0199
0.0407	0.0617	0.1709	0.0284	0.0049	0.0200
0.0129	0.0952	0.1344	0.0160	0.0040	0.0322
0.0059	0.0963	0.0668	0.0043	0.0026	0.0455
0.0010	0.0522	0.0149	0.0008	0.0009	0.0294
0.0000	0.0153	0.0025	0.0000	0.0000	0.0077
0.0000	0.0048	0.0000	0.0000	0.0000	0.0036
0.0000	0.0025	0.0007	0.0003	0.0000	0.0041

Table A8: Experimental data set for LPST Jet A pyrolysis at ~12 atm, with 6356 ppm fuel in Ar.

T5_t_extr	T5_t_extr -	T5_t_extr +	T5_v_extr	P5	τ	CH4	C2H6	C2H4	C2H2	C3H8	C3H6	aC3H4
K	K	K	K	atm	sec	Yield (species mole fraction/initial fuel mole fraction)						
1064	1051	1078	1068	12.27	0.00201	0.0464	0.0086	0.1149	0.0003	0.0020	0.0531	0.0004
1107	1094	1119	1098	13.74	0.00194	0.1185	0.0292	0.3523	0.0022	0.0067	0.1534	0.0020
1128	1117	1140	1128	12.33	0.00216	0.1853	0.0533	0.6067	0.0061	0.0116	0.2502	0.0046
1141	1125	1157	1138	12.81	0.00185	0.1155	0.0291	0.3463	0.0021	0.0066	0.1505	0.0018
1160	1153	1167	1158	12.14	0.00211	0.2301	0.0709	0.7893	0.0105	0.0150	0.3115	0.0074
1163	1154	1173	1165	12.92	0.00220	0.2442	0.0771	0.8496	0.0135	0.0154	0.3274	0.0086
1164	1152	1176	1171	13.29	0.00203	0.1871	0.0545	0.6199	0.0061	0.0117	0.2540	0.0046
1195	1174	1215	1198	12.06	0.00216	0.2817	0.0938	1.0092	0.0187	0.0183	0.3765	0.0116
1216	1207	1225	1217	12.58	0.00198	0.2897	0.0924	1.0142	0.0186	0.0181	0.3756	0.0121
1244	1233	1256	1243	12.43	0.00217	0.4026	0.1393	1.4308	0.0529	0.0221	0.4541	0.0264
1256	1242	1270	1246	13.00	0.00214	0.4158	0.1386	1.4405	0.0550	0.0218	0.4552	0.0275
1261	1253	1270	1267	12.45	0.00198	0.3488	0.1179	1.2385	0.0352	0.0207	0.4274	0.0197
1262	1254	1270	1259	12.68	0.00209	0.3505	0.1231	1.2852	0.0372	0.0215	0.4339	0.0196
1311	1299	1323	1305	12.76	0.00227	0.4926	0.1612	1.6044	0.0985	0.0198	0.4431	0.0407
1315	1301	1330	1306	12.43	0.00224	0.5220	0.1650	1.6313	0.1228	0.0174	0.4208	0.0454
1345	1337	1353	1337	12.15	0.00239	0.5384	0.1615	1.6216	0.1226	0.0166	0.4129	0.0467
1368	1352	1385	1355	12.26	0.00210	0.5935	0.1711	1.7308	0.1775	0.0132	0.3832	0.0519
1383	1368	1398	1375	12.20	0.00219	0.6008	0.1612	1.6774	0.1942	0.0103	0.3472	0.0513
1391	1372	1410	1379	12.12	0.00216	0.6601	0.1615	1.7900	0.2525	0.0077	0.3205	0.0524
1407	1385	1431	1397	12.28	0.00222	0.7138	0.1421	1.7908	0.3192	0.0047	0.2719	0.0511
1487	1461	1514	1478	11.47	0.00221	0.8758	0.0753	1.7030	0.5889	0.0013	0.1296	0.0418
1547	1524	1570	1551	11.85	0.00226	0.9816	0.0354	1.5595	0.9203	0.0008	0.0677	0.0287
1597	1581	1612	1606	11.59	0.00209	0.3534	0.0343	0.6521	0.3047	0.0023	0.0757	0.0144
1632	1625	1638	1627	11.69	0.00223	0.3961	0.0276	0.5939	0.4789	0.0015	0.0056	0.0131

1-C4H8	pC3H4	1,3-C4H6	i-C4H8	1,2-C4H6	C4H4
Yield (species mole fraction/initial fuel mole fraction)					
0.0154	0.0005	0.0092	0.0061	0.0001	0.0002
0.0461	0.0021	0.0331	0.0164	0.0003	0.0000
0.0781	0.0047	0.0632	0.0256	0.0000	0.0010
0.0453	0.0021	0.0271	0.0161	0.0000	0.0005
0.0997	0.0074	0.0880	0.0297	0.0013	0.0019
0.1018	0.0085	0.0956	0.0321	0.0013	0.0026
0.0785	0.0046	0.0645	0.0254	0.0008	0.0011
0.1169	0.0111	0.1172	0.0354	0.0018	0.0034
0.1186	0.0114	0.1194	0.0338	0.0020	0.0034
0.1113	0.0248	0.1712	0.0367	0.0032	0.0093
0.1090	0.0257	0.1736	0.0366	0.0033	0.0097
0.1240	0.0179	0.1537	0.0378	0.0028	0.0060
0.1223	0.0186	0.1528	0.0396	0.0027	0.0065
0.0621	0.0426	0.1793	0.0302	0.0035	0.0164
0.0423	0.0521	0.1733	0.0268	0.0035	0.0196
0.0368	0.0532	0.1754	0.0248	0.0036	0.0203
0.0211	0.0715	0.1637	0.0191	0.0034	0.0263
0.0150	0.0760	0.1487	0.0162	0.0032	0.0280
0.0116	0.0868	0.1386	0.0135	0.0028	0.0319
0.0079	0.0935	0.1156	0.0103	0.0024	0.0359
0.0029	0.0862	0.0598	0.0029	0.0013	0.0398
0.0020	0.0630	0.0341	0.0016	0.0008	0.0390
0.0097	0.0260	0.0299	0.0041	0.0007	0.0131
0.0061	0.0246	0.0235	0.0027	0.0006	0.0147

Table A9: Experimental data set for LPST Jet A pyrolysis at ~1 atm, with 6356 ppm fuel in Ar.

T5_t_extr	T5_t_extr -	T5_t_extr +	T5_v_extr	P5	τ	CH4	C2H6	C2H4	C2H2	C3H8	C3H6	aC3H4
K	K	K	K	atm	sec	Yield (species mole fraction/initial fuel mole fraction)						
1127	1117	1137	1132	1.19	0.00200	0.0912	0.0624	0.4460	0.0030	0.0033	0.1951	0.0036
1172	1169	1176	1165	1.17	0.00224	0.1239	0.0910	0.6490	0.0053	0.0166	0.2681	0.0065
1193	1175	1211	1180	1.19	0.00219	0.1723	0.1383	0.9496	0.0162	0.0235	0.3545	0.0133
1204	1197	1212	1198	1.20	0.00207	0.1751	0.1384	0.9586	0.0145	0.0239	0.3603	0.0131
1220	1205	1234	1211	1.25	0.00196	0.1953	0.1556	1.0753	0.0209	0.0256	0.3872	0.0171
1224	1222	1225	1222	1.19	0.00215	0.1737	0.1403	0.9708	0.0162	0.0240	0.3658	0.0142
1235	1213	1256	1224	1.17	0.00207	0.2074	0.1716	1.1612	0.0257	0.0268	0.4085	0.0216
1253	1240	1267	1241	1.15	0.00212	0.2183	0.1815	1.2244	0.0304	0.0278	0.4228	0.0245
1270	1258	1281	1262	1.14	0.00229	0.2710	0.2098	1.3976	0.0472	0.0285	0.4462	0.0368
1282	1277	1287	1275	1.19	0.00186	0.2719	0.2191	1.3983	0.0582	0.0267	0.4291	0.0443
1287	1278	1295	1281	1.20	0.00198	0.2565	0.2059	1.3564	0.0462	0.0275	0.4348	0.0364
1305	1300	1310	1302	1.03	0.00207	0.3062	0.2393	1.4913	0.0777	0.0263	0.4293	0.0558
1326	1312	1339	1319	1.17	0.00215	0.3296	0.2482	1.5511	0.0907	0.0256	0.4318	0.0609
1346	1336	1356	1340	1.17	0.00204	0.3270	0.2537	1.5736	0.0966	0.0266	0.4408	0.0622
1361	1343	1379	1352	1.13	0.00234	0.3689	0.2513	1.5816	0.1169	0.0207	0.3972	0.0668
1376	1366	1386	1373	1.20	0.00188	0.3563	0.2559	1.5985	0.1161	0.0227	0.4136	0.0683
1379	1369	1389	1377	1.21	0.00197	0.3668	0.2552	1.6062	0.1298	0.0213	0.4063	0.0704
1386	1377	1395	1381	1.12	0.00228	0.3951	0.2548	1.6320	0.1473	0.0181	0.3825	0.0706
1396	1380	1413	1384	1.19	0.00208	0.3835	0.2528	1.6098	0.1289	0.0194	0.3879	0.0686
1443	1424	1463	1434	1.11	0.00244	0.5216	0.2166	1.7205	0.3039	0.0071	0.2662	0.0679
1547	1534	1560	1540	1.11	0.00244	0.6790	0.1397	1.7329	0.6122	0.0029	0.1473	0.0561

1-C4H8	pC3H4	1,3-C4H6	i-C4H8	1,2-C4H6	C4H4
Yield (species mole fraction/initial fuel mole fraction)					
0.0608	0.0028	0.0384	0.0203	0.0005	0.0006
0.0854	0.0045	0.0687	0.0262	0.0008	0.0014
0.1142	0.0101	0.1081	0.0313	0.0017	0.0030
0.1163	0.0095	0.1082	0.0318	0.0016	0.0030
0.1221	0.0128	0.1268	0.0356	0.0037	0.0042
0.1158	0.0105	0.1089	0.0333	0.0018	0.0035
0.1214	0.0156	0.1324	0.0348	0.0026	0.0056
0.1218	0.0179	0.1396	0.0356	0.0027	0.0063
0.1093	0.0261	0.1629	0.0342	0.0034	0.0094
0.0854	0.0326	0.1568	0.0314	0.0037	0.0120
0.1034	0.0256	0.1540	0.0338	0.0033	0.0096
0.0650	0.0425	0.1652	0.0279	0.0040	0.0148
0.0558	0.0486	0.1683	0.0269	0.0042	0.0164
0.0575	0.0495	0.1720	0.0276	0.0044	0.0166
0.0323	0.0641	0.1581	0.0223	0.0043	0.0211
0.0383	0.0622	0.1635	0.0239	0.0045	0.0205
0.0318	0.0681	0.1620	0.0230	0.0045	0.0215
0.0257	0.0772	0.1532	0.0204	0.0042	0.0248
0.0277	0.0699	0.1551	0.0209	0.0042	0.0232
0.0119	0.1059	0.1113	0.0104	0.0034	0.0384
0.0052	0.1019	0.0658	0.0044	0.0022	0.0452

Table A10: Experimental data set for LPST JP10 pyrolysis at ~12 atm, with 75 ppm fuel in Ar.

T5_t_extr	T5_t_extr -	T5_t_extr +	T5_v_extr	P5	τ	CH4	C2H6	C2H4	C2H2	C3H6	aC3H4
K	K	K	K	atm	sec	Mole fraction (ppm)					
1039	1017	1061	1024	8.2	0.00135	0.00	0.00	0.00	0.00	0.00	0.00
1075	1070	1080	1070	11.8	0.00231	0.00	0.00	2.37	0.00	0.55	0.00
1103	1095	1111	1099	12.3	0.00208	0.00	0.00	4.60	0.00	0.98	0.51
1148	1145	1151	1147	12.2	0.00208	1.15	0.42	15.96	0.89	3.97	2.07
1163	1147	1178	1156	12.3	0.00208	0.55	0.00	9.61	0.42	2.34	1.23
1166	1160	1173	1161	12.2	0.00219	0.00	0.00	7.66	0.00	1.53	0.72
1196	1188	1204	1196	12.5	0.00209	2.22	1.20	29.52	2.31	7.02	3.72
1206	1199	1213	1202	12.7	0.00199	2.85	1.60	33.40	3.09	7.79	4.09
1212	1208	1217	1213	12.3	0.00193	3.56	2.28	39.38	4.03	9.08	4.67
1217	1214	1221	1216	12.1	0.00197	3.77	2.43	41.23	4.47	9.10	5.13
1229	1215	1243	1222	12.4	0.00219	6.74	4.82	56.63	9.69	10.69	6.20
1229	1217	1241	1220	12.5	0.00198	2.77	1.60	32.76	2.88	7.76	4.06
1250	1234	1266	1243	12.3	0.00213	6.65	4.88	56.94	9.55	10.87	6.34
1261	1251	1272	1253	12.1	0.00206	5.86	4.17	53.63	8.32	10.18	6.30
1274	1266	1281	1268	12.3	0.00214	7.74	5.26	59.23	12.97	9.78	5.92
1277	1258	1296	1269	11.9	0.00214	8.20	5.48	60.32	14.63	9.69	5.76
1325	1313	1337	1318	12.0	0.00217	10.54	5.66	63.02	23.70	8.43	5.31
1334	1325	1343	1331	12.0	0.00220	12.94	5.19	64.17	35.63	6.63	5.51
1384	1376	1392	1378	11.7	0.00254	16.06	4.62	67.46	48.52	5.14	5.79
1392	1379	1405	1385	11.7	0.00204	12.78	5.23	64.23	35.82	6.66	5.57
1429	1415	1443	1422	12.3	0.00219	23.21	3.47	61.57	87.21	1.86	4.43
1431	1422	1439	1426	12.2	0.00211	23.79	3.40	65.96	85.14	2.15	5.01
1435	1428	1443	1429	11.8	0.00227	23.31	3.62	67.72	77.84	2.56	5.27
1456	1442	1471	1442	12.5	0.00210	24.06	2.39	65.67	84.88	1.71	4.93
1461	1449	1473	1455	12.6	0.00209	25.81	1.78	62.97	92.59	1.23	4.20
1467	1452	1482	1459	12.3	0.00202	25.72	2.16	65.06	92.80	1.45	4.72
1471	1464	1479	1472	11.5	0.00228	31.11	1.43	55.15	139.58	0.68	2.56
1482	1467	1497	1478	12.6	0.00212	28.96	1.60	53.79	120.80	0.73	2.87
1486	1476	1495	1478	11.8	0.00217	27.42	1.87	59.46	105.11	0.97	3.54
1514	1504	1524	1508	11.8	0.00227	27.99	1.29	49.52	125.60	0.61	2.31
1525	1515	1534	1521	12.3	0.00208	30.86	1.06	58.02	129.09	0.75	2.73
1599	1584	1615	1589	11.6	0.00233	24.77	1.24	19.43	161.66	0.44	1.20
1682	1670	1694	1677	10.7	0.00257	9.74	0.45	4.93	203.46	0.00	0.59

1-C4H8	pC3H4	1,3-C4H6	C4H2	C4H4	C5H8	C5H6	C6H6	C7H8	C10H16
Mole fraction (ppm)									
0.00	0.00	0.00	0.00	0.00	0.00	0.00	0.00	0.00	71.46
0.41	0.00	0.00	0.00	0.00	0.56	1.49	0.23	0.00	65.23
0.57	0.00	0.33	0.00	0.00	1.21	3.50	1.21	0.18	60.96
1.78	0.66	1.30	0.00	0.17	2.70	12.10	4.86	0.84	45.75
1.17	0.29	0.74	0.00	0.00	2.07	7.36	2.59	0.50	53.56
0.56	0.25	0.54	0.00	0.00	0.71	3.74	1.55	0.00	38.10
2.37	1.75	2.54	0.00	0.37	2.84	21.85	9.33	1.50	33.05
2.36	2.15	3.09	0.00	0.60	2.82	24.24	11.04	1.77	26.98
2.40	2.66	3.74	0.00	0.77	2.66	27.20	13.12	2.08	22.56
1.99	3.24	3.76	0.00	0.71	2.23	29.32	14.53	2.29	19.39
0.87	6.08	5.39	0.00	1.62	0.92	35.55	19.93	3.36	9.31
2.39	2.08	2.96	0.00	0.49	2.81	23.52	10.77	1.70	27.79
0.91	5.97	5.45	0.00	1.64	0.99	35.84	20.03	3.43	8.21
0.88	5.78	4.85	0.00	1.22	0.98	36.19	19.74	3.27	8.48
0.25	8.59	5.28	0.19	1.76	0.33	36.43	22.67	4.00	3.74
0.20	8.86	5.42	0.23	2.03	0.28	35.65	22.77	3.94	3.57
0.00	10.64	5.33	0.53	2.76	0.12	29.70	25.86	4.68	2.63
0.00	11.71	4.81	1.13	3.24	0.00	21.20	25.72	4.22	2.48
0.00	12.76	4.19	2.01	3.50	0.00	13.25	27.12	4.22	2.60
0.00	11.96	4.88	1.14	3.36	0.00	21.24	26.20	4.18	2.44
0.00	10.00	2.39	4.54	4.63	0.00	3.86	23.97	2.79	1.42
0.00	11.36	2.71	4.79	4.84	0.00	3.98	25.32	2.97	1.48
0.00	11.85	2.98	4.38	4.74	0.00	4.27	28.89	3.58	1.99
0.00	11.39	2.24	5.66	3.94	0.00	2.38	28.04	2.99	1.40
0.00	9.60	1.64	6.78	3.56	0.00	1.74	26.44	2.34	1.22
0.00	10.79	2.00	6.34	4.15	0.00	1.98	26.86	2.69	1.37
0.00	5.99	0.88	10.42	2.69	0.00	1.15	24.65	1.34	0.83
0.00	6.55	1.00	8.39	3.15	0.00	1.45	21.14	1.42	0.78
0.00	8.10	1.35	7.46	3.74	0.00	1.67	24.86	1.91	0.98
0.00	5.39	0.79	9.38	2.40	0.00	1.03	22.40	1.22	0.75
0.00	6.21	0.85	11.33	2.61	0.00	1.14	23.38	1.13	0.85
0.00	2.70	0.36	11.30	1.18	0.00	0.73	7.77	0.51	0.23
0.00	1.36	0.00	26.30	0.54	0.00	0.30	3.95	0.39	0.25

APPENDIX C

Spearman's rank correlation coefficient between species mole fraction an A factors of important reactions in Jet A pyrolysis simulations.

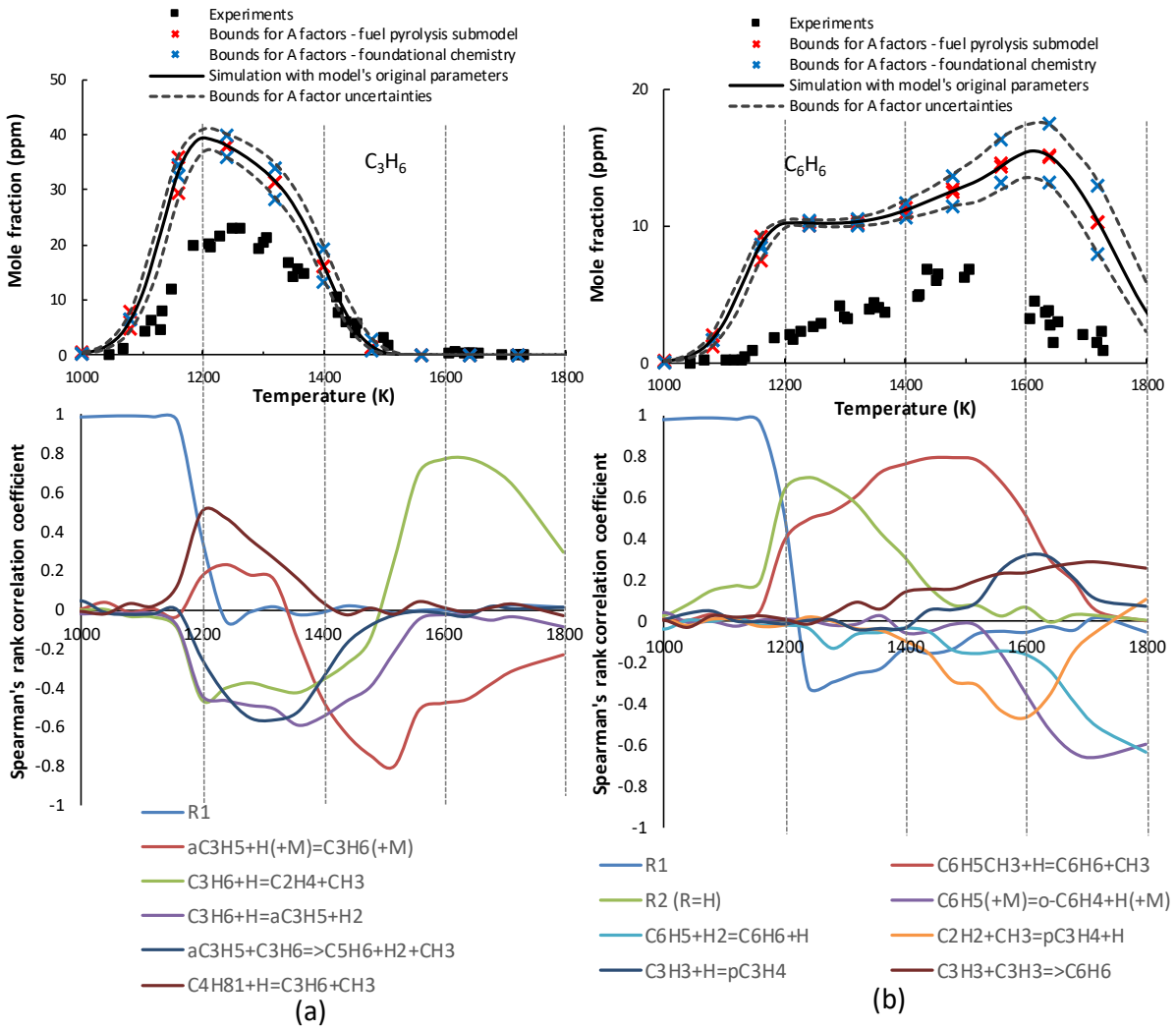

Figure A3: Spearman's rank correlation coefficients (bottom two subplots) between important reactions and certain species in the Jet A model acquired by the full model Monte Carlo simulation data with *A* factor perturbation at 25 atm 52.3 ppm fuel/Ar, 2.3 ms reaction time. The coefficients are plotted along temperature. It is compared to the experiments in the HPST and simulations (top two subplots) with the uncertainty band from the *A* factor Monte Carlo simulation. (a) C_3H_6 and (b) C_6H_6. Reactions are selected based on the peak of the absolute value of the Spearman's rank correlation coefficients within the temperature region where the species has significant existence.

APPENDIX D

Additional plots for JP10 pyrolysis: Monte Carlo analysis (Figure A4) and pressure dependence analysis (Figure A5)

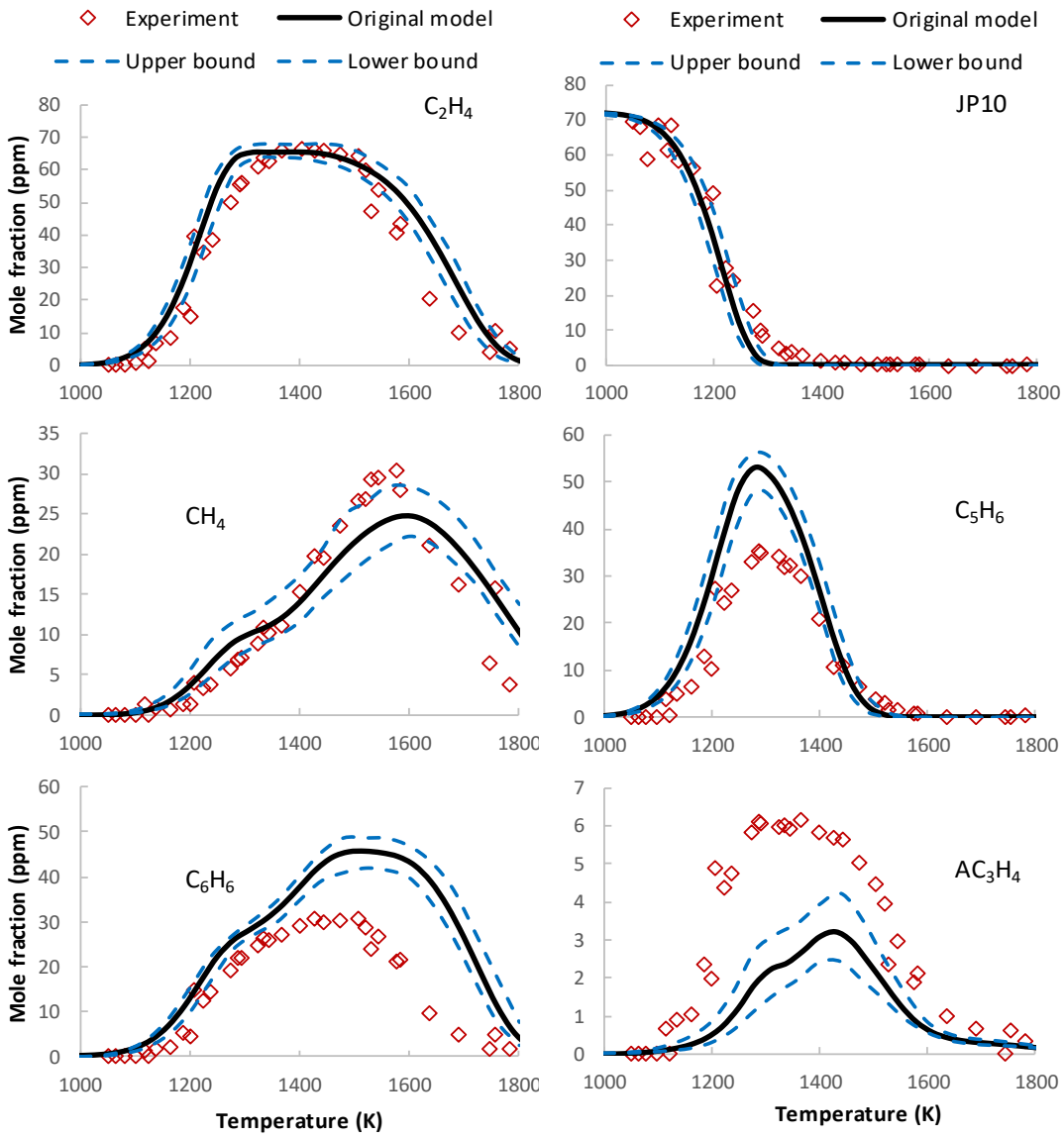

Figure A4: Selected species comparison between experiments (red diamond) and simulations (black solid line for original HyChem model, blue dashed lines for the upper and lower bounds of Monte Carlo simulations) for JP10 pyrolysis at the condition of 25 atm and 72 ppm of fuel in the HPST. In the Monte Carlo simulations, all A factors of the HyChem model are sampled randomly in the ±30% range of their original values.

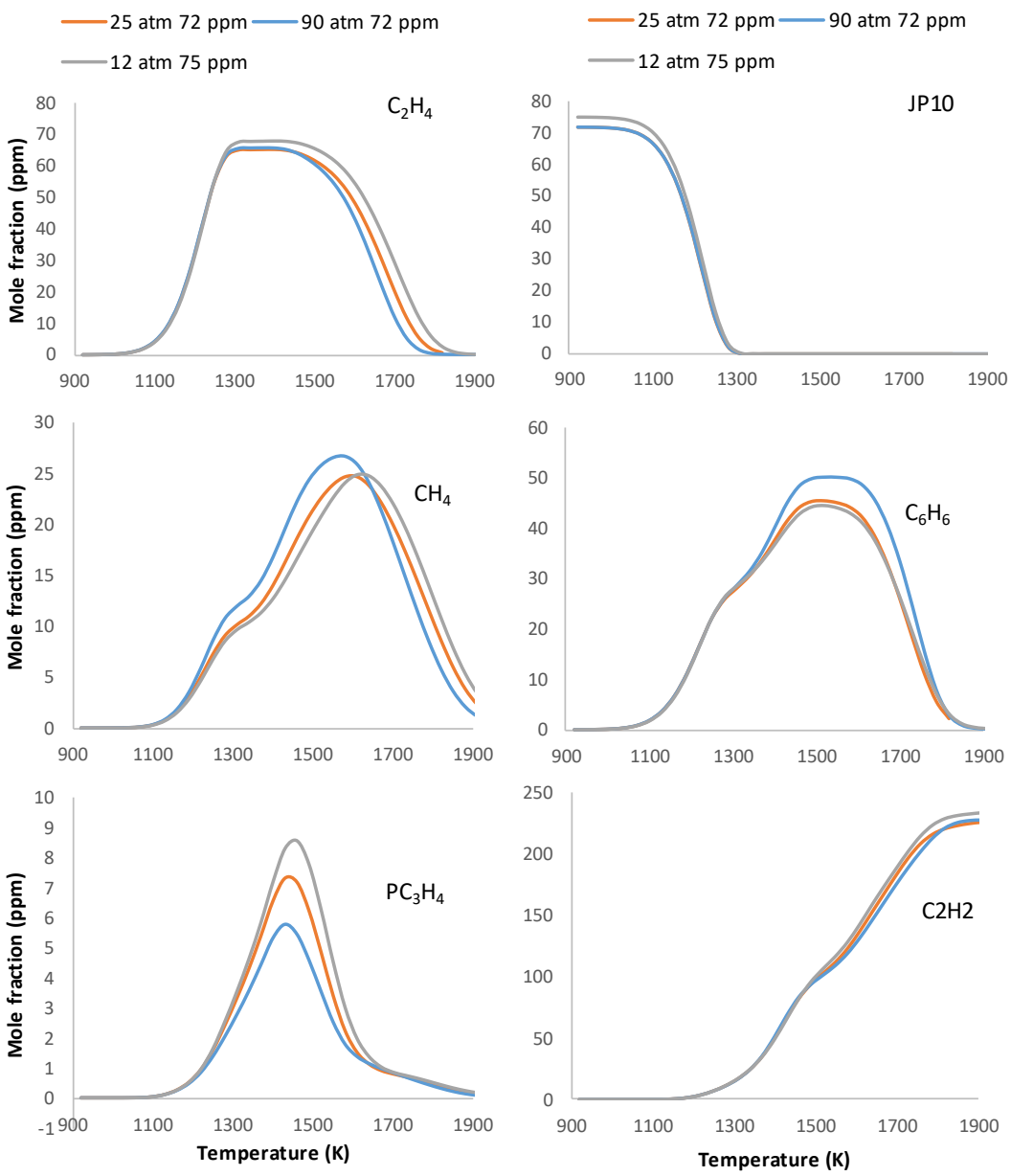

Figure A5: JP10 pressure dependent plot in HPST and LPST simulations. Reaction time for HPST is 2.3 ms. Reaction time for LPST is 2.1 ms.

APPENDIX E

Explanation of Jet A fuel's composition consistency in the shock tube

In the HPST, the reported Jet A mole fraction of 52.3 ppm is obtained from the CO_2 conversion experiment, which is 9.4% less than the predicted value from the preparation of the fuel/Ar mixture. In case the latter mole fraction value was underestimated, we compared Jet A fuel loss to that of JP10 in the same way of calculation and it shows that our JP10 CO_2 conversion result also gives a mole fraction of 9.4% less than the predicted value from mixture preparation possibly due to the tank volume uncertainty. From our experience, JP10 vaporizes easily although it has high boiling point (185 °C). Thus, in this respect, we believe the 9.4% loss of carbon for the Jet A fuel is not underestimated. In addition, our HP-5 chromatogram of Jet A directly injected from the shock tube to GC shows that more than half of the peak areas are after the retention time of JP10, which has 10 carbons per molecule. The Jet A in average has 11.37 carbons per molecule. This shows that the chance is small for the occurrence of a strong preferential absorption or condensation of Jet A component species in the injection process. Judging from the above observations, we believe that the Jet A injected into the HPST did not suffer a significant preferential loss of fuel components. However, to be exactly sure, a GCxGC-TOFMS study will be needed and is planned for the future.

APPENDIX F

Proof for approximations:

$$\Delta v_l \approx \frac{x_{endwall}}{t} - \frac{x_{endwall}}{t_u} \qquad (6.11)$$

$$\Delta v_u \approx \frac{x_{endwall}}{t_l} - \frac{x_{endwall}}{t} \qquad (6.12)$$

Proof:

Basic equations:

$$t = \int_0^{0.37} \frac{1}{ax+b}\, dx$$

$$t_l = \int_0^{0.37} \frac{1}{ax+b+\Delta v(x)}\, dx$$

The proposed equation:

$$\Delta v_u \approx \frac{0.37}{t_l} - \frac{0.37}{t} = \frac{0.37(t-t_l)}{tt_l} = \frac{0.37\Delta t}{tt_l}$$

To prove that this is a reasonable approximation, we do

$$\Delta t = t - t_l = \int_0^{0.37} \left[\frac{1}{ax+b} - \frac{1}{ax+b+\Delta v(x)}\right] dx$$

$$= \int_0^{0.37} \frac{\Delta v(x)}{(ax+b)[ax+b+\Delta v(x)]}\, dx$$

For our experimental cases, the attenuation of velocity is small compared to the absolute value of velocity. (This is why t-x curve is highly linear as result). Thus $\frac{1}{(ax+b)[ax+b+\Delta v(x)]}$ is weakly dependent

on x, and, as a weighting coefficient in the integral, can be approximated as constant $1/v_{avg}^2$. Here, we let

$$v_{avg} = \frac{\int_0^{0.37} v(x)dx}{0.37}$$

As we just reasoned, when v_{avg} is used as coefficient (instead of subtraction operations), it can be approximated as any value of v(x). Therefore, we can say it is close enough to another way of averaging:

$$v_{avg} \approx \frac{0.37}{t}$$

Now,

$$\Delta t = \frac{1}{v_{avg}^2}\int_0^{0.37} \Delta v(x)\, dx$$

$$= \frac{1}{v_{avg}^2}\Delta v_{avg} * 0.37$$

$$\approx \frac{t^2}{0.37^2}\Delta v_{avg} * 0.37$$

Hence,

$$\Delta v_{avg} = \frac{0.37\Delta t}{t^2} \approx \frac{0.37\Delta t}{t t_l}$$

We assume that physically, the deviation of velocity away from the mean is close to uniform along x, or at least $\Delta v(x) \approx \Delta v_{avg}$ is an "averaged" case for a given Δt, meaning among all possible curves of $\Delta v(x)$ for a given Δt will have be averaged to $\Delta v(x) \approx \Delta v_{avg}$.

As we mentioned before, there is no analytical calculation without any approximations or simulations. This is a reasonable approximation for Δv calculation.

APPENDIX G
The HyChem model information

For general information of the HyChem modeling approach and downloads, see:

https://web.stanford.edu/group/haiwanglab/HyChem/index.html.

The fuel lumped reactions in pyrolysis study from HyChem model:

(A units mole-cm-sec-K, E units cal/mole)

A n E

Jet A fuel lumped reactions R1 and R2 without oxygen involved:

POSF10325=>
1.7426762C2H4+0.8190578C3H6+0.0871338iC4H8+0.2614014C4H81+0.17C6H6+0.1633333
C6H5CH3+0.5H+1.5CH3 1.53E+27 -2.58 87697.0

POSF10325+H=>
H2+0.45CH4+1.5945764C2H4+0.7494509C3H6+0.0797288iC4H8+0.2391865C4H81+0.2465C
6H6+0.2368333C6H5CH3+0.3H+0.7CH3 7.66E-02 4.76 1294.9

POSF10325+CH3=>
1.45CH4+1.5945764C2H4+0.7494509C3H6+0.0797288iC4H8+0.2391865C4H81+0.2465C6H6
+0.2368333C6H5CH3+0.3H+0.7CH3 3.17E-07 5.95 5748.4

JP10 fuel lumped reactions R3 and R4 without oxygen involved

C10H16=>
1.79H+0.01CH3+0.20aC3H5+0.866256C2H4+0.069300C3H6+0.952881C5H6+0.407140H2+0.
351372C6H6+0.082420C6H5CH3 3.20E+15 0.000 72500

C10H16+H=>
H2+0.43H+0.26CH3+0.31aC3H5+0.781605C2H4+0.062528C3H6+0.859765C5H6+0.367354H
2+0.361212C6H6+0.084728C6H5CH3 1.83E+04 2.765 2551

C10H16+CH3=>
CH4+0.43H+0.26CH3+0.31aC3H5+0.781605C2H4+0.062528C3H6+0.859765C5H6+0.367354
H2+0.361212C6H6+0.084728C6H5CH3 1.84E-05 4.891 3621

APPENDIX H

The rigorous approach for converting CO_2 mole fractions to fuel mole fractions in CO_2 conversion experiments of Jet A fuel (POSF#10325) in concentrated mixtures (high fuel mole fraction).

Variables and parameters before shock firing:

Given: P_1 as the pressure of the injected fuel/Ar mixture initially injected in the driven section, P_2 as the pressure of the driven gas after further injecting O_2. Unknown variables are the total moles of fuel, Ar, O_2 in the non-reacted mass that was later sampled by the GC after the shock: n_f, n_{Ar}, and n_{O2}. They are related by

$$\frac{n_{O2}}{n_f + n_{Ar}} = \frac{P_2 - P_1}{P_1} \qquad (\mathrm{A}.1)$$

Variables and parameters after shock firing:

For the GC-sampled mass, the moles of CO_2, CO, Ar, H_2O, O_2 are n_{CO2}, n_{CO}, n_{Ar}, n_{H2O}, and $n_{2,O2}$. Given the molecular formula of C_mH_n, we know

$$n_f = (n_{CO} + n_{CO2})\frac{1}{m} \qquad (A.2)$$

$$n_{H2O} = n_f * \frac{n}{2} \qquad (A.3)$$

$$n_{2,O2} = n_{O2} - 0.5 * n_{CO} - n_{CO2} \qquad (A.4)$$

Let

$$k_1 = \frac{n_{CO2}}{n_{CO} + n_{CO2} + n_{Ar} + n_{H2O} + n_{2,O2}} \qquad (A.5)$$

$$k_2 = \frac{n_{CO}}{n_{CO} + n_{CO2} + n_{Ar} + n_{H2O} + n_{2,O2}} \qquad (A.6)$$

$$x = \frac{n_f}{n_{Ar}} \qquad (A.7)$$

Derivation of fuel mole fraction:

From Equations A.1-A.7, we can get

$$x = \frac{1+\frac{k_2}{k_1}}{m} * \frac{P_2}{P_1} * \frac{1}{-1+\frac{1-k_2}{k_1} - \frac{P_2-P_1}{P_1}\frac{\frac{k_2}{k_1}+1}{m} + \frac{k_2}{2k_1} - \frac{1+\frac{k_2}{k_1}}{m} * \frac{n}{2}} \qquad (A.8)$$

Finally, the fuel mole fraction in the original mixture without oxygen is

$$y = \frac{x}{1+x} \qquad (A.9)$$

In a simplified calculation, if $k_2 \ll k_1 \ll 1$ (when CO_2 is far greater than the CO in the sampled gas and has a very small mole fraction in Ar), then the fuel mole fraction can be simplified as

$$y \approx \frac{P_2}{P_1} * \frac{k_1}{m} \qquad (A.10)$$

which is the same formula as what one would typically use in a CO_2 conversion without needing the complex calculation described above.

APPENDIX I

Permission of using Figure 11.

Copyright Clearance Center RightsLink®

Home | Create Account | Help

Title: A physics-based approach to modeling real-fuel combustion chemistry – II. Reaction kinetic models of jet and rocket fuels

Author: Rui Xu,Kun Wang,Sayak Banerjee,Jiankun Shao,Tom Parise,Yangye Zhu,Shengkai Wang,Ashkan Movaghar,Dong Joon Lee,Runhua Zhao,Xu Han,Yang Gao,Tianfeng Lu,Kenneth Brezinsky,Fokion N. Egolfopoulos,David F. Davidson,Ronald K. Hanson,Craig T. Bowman et al.

Publication: Combustion and Flame

Publisher: Elsevier

Date: Available online 10 April 2018

LOGIN

If you're a copyright.com user, you can login to RightsLink using your copyright.com credentials.

Already a RightsLink user or want to learn more?

Please note that, as the author of this Elsevier article, you retain the right to include it in a thesis or dissertation, provided it is not published commercially. Permission is not required, but please ensure that you reference the journal as the original source. For more information on this and on your other retained rights, please visit: https://www.elsevier.com/about/our-business/policies/copyright#Author-rights

BACK | CLOSE WINDOW

VITA

EDUCATION

University of Illinois at Chicago, Chicago, Illinois, USA

Ph.D. Candidate Mechanical Engineering, August 2012 – June 2018
A shock tube study of real jet fuels Jet A and JP10
Advisor: Prof. Kenneth Brezinsky

M.S. Mechanical Engineering, September 2012

Advisor: Prof. Suresh Aggarwal

Southeast University, Nanjing, China

B.Eng. Automation, July 2008

WORK EXPERIENCE

University of Illinois at Chicago, Chicago, Illinois, USA

Research assistant/teaching assistant, August 2011 – June 2018

Dalian Datang Scientific Instruments Co. Ltd, Dalian, China

Product Design Engineer/Assistant Engineer, August 2008 – July 2010

PUBLICATIONS

X. Han, M. Liszka, R. Xu, K. Brezinsky, H. Wang, A high pressure shock tube study of the pyrolysis of real jet fuel Jet A, *Proceedings of Combustion Institute*, 37 (2018).

R. Xu, K. Wang, S. Banerjee, J. Shao, T. Parise, Y. Zhu, S. Wang, A. Movaghar, D. J. Lee, R. Zhao, X. Han, Y. Gao, T. Lu, K. Brezinsky, F. N. Egolfopoulos, D. F. Davidson, R. K. Hanson, C. T. Bowman, H. Wang, A physics-based approach to modeling real-fuel combustion chemistry - II. Reaction kinetic models of jet and rocket fuels, *Combustion of Flame*, 193 (2018), 520-537.

Y. Tao, R. Xu, K. Wang, J. Shao, S. E. Johnson, A. Movaghar, X. Han, J. Park, T. Lu, K. Brezinsky, F. N. Egolfopoulos, D. F. Davidson, R. K. Hanson, C. T. Bowman, H. Wang, A physics-based approach to

modeling real-fuel combustion chemistry - III. Reaction kinetic model of JP10, *Combustion of Flame*, submitted, 2018.

X. Fu, X. Han, K. Brezinsky, S.K. Aggarwal, Effect of fuel molecular structure and premixing on soot emissions from n-heptane and 1-heptene flames, *Energy & Fuels*, 27 (10) (2013), 6262-6272.

X. Han, S.K. Aggarwal, A numerical investigation on counterflow flames of biodiesel/diesel Surrogate Blends, *ASME Turbo Expo 2013: Turbine Technical Conference and Exposition* 2013.

X. Han, S.K. Aggarwal, K. Brezinsky, Effect of unsaturated bond on NOx and PAH formation in n-heptane and 1-heptene triple flames, *Energy & Fuels*, 27 (1) (2013), 537-548.

X. Han, S.K. Aggarwal, K. Brezinsky, A numerical investigation of NO_x emission from n-heptane and 1-heptene triple flames. *Combustion Institute Central State Conference* 2012.

PRESENTATIONS AND POSTERS

Poster: Shock Tube Study of the Pyrolysis of the Jet Fuels JP10 and JetA2. *10^{th} US National Combustion Meeting*. 2017.

Poster: Shock Tube Study of the Pyrolysis of the Jet Fuels JP10 and JetA2. *10^{th} International Conference in Chemical Kinetics*. 2017.

Presentation, A numerical investigation of NO_x emission from n-heptane and 1-heptene triple flames. *Combustion Institute Central State Conference* 2012.